

Aerosol Satellite Remote Sensing

Satelliet Detectie van Aërosolen

(met een samenvatting in het Nederlands)

Proefschrift

ter verkrijging van de graad van doctor
aan de Universiteit van Utrecht
op gezag van de Rector Magnificus, Prof. Dr. H.O. Voorma,
ingevolge het besluit van het College voor Promoties
in het openbaar te verdedigen
op maandag 11 oktober 1999 des middags te 12:45 uur.

door

Joris Pepijn Veefkind

geboren op 1 mei 1970 te Eindhoven

Promotores: Prof. Dr. Ir. P.J.H. Bultjes
(Verbonden aan de Faculteit der Natuur -en
Sterrenkunde van de Universiteit Utrecht)

Prof. Dr. G. de Leeuw
(Verbonden aan TNO Fysisch en Elektronisch
Laboratorium te 's-Gravenhage)

The work described in this thesis was performed at TNO Physics and Electronics Laboratory (TNO-FEL), The Hague, The Netherlands, and was made possible by a grant from the Netherlands Space Research Organization (SRON), and by the TNO Defense Research AIO Fund.

ISBN 90-393-2173-6

Now the world is very old
and the sky is very high
and we're just traffic in between
You and I [..]

Lloyd Cole

Contents

Voorwoord	v
1 Introduction and Overview	1
1.1 Introduction	1
1.2 Atmospheric Aerosols	2
1.3 Climate Forcing	3
1.3.1 Direct Aerosol Forcing	4
1.3.2 Indirect Aerosol Forcing	7
1.3.3 Modeling Needs	9
1.4 Aerosol Satellite Remote Sensing	9
1.5 Satellite Sensors	10
1.6 Aim of this Work	12
1.7 Outline of this thesis	12
Bibliography	13
2 Theory of Aerosol Satellite Remote Sensing	15
2.1 Introduction	15
2.2 Scattering and Absorption by Aerosols	15
2.2.1 Definitions	15
2.2.2 Aerosol Optical Properties	18
2.3 Principles of Aerosol Satellite Remote Sensing	22
Bibliography	27
3 A New Algorithm to Determine the Spectral Aerosol Optical Depth over the Ocean from Satellite Radiometer measurements	31
3.1 Introduction	32
3.2 Algorithm Description	33
3.2.1 Radiative Transfer Calculations	33
3.2.2 Aerosol Optical Depth Retrieval	38
3.3 Sensitivity Study	39
3.4 Results and Discussion	42
3.5 Conclusions	46
Bibliography	47

4	Aerosol Optical Depth retrieval using ATSR-2 and AVHRR during TARFOX	49
4.1	Introduction	50
4.2	Retrieval Algorithm	51
4.3	Experiments	53
4.4	Results and Discussion	53
4.4.1	Synoptic Situation	53
4.4.2	ATSR-2 Retrieval	54
4.4.3	AVHRR Retrieval	57
4.4.4	Aerosol Optical Depth Gradient	60
4.5	Conclusions	61
	Bibliography	62
5	Retrieval of Aerosol Optical Depth over Land using two-angle view Satellite Radiometry during TARFOX	65
5.1	Introduction	66
5.2	The ATSR-2 sensor	67
5.3	The Dual View Algorithm	67
5.4	Results and Discussion	68
5.5	Conclusions	72
	Bibliography	72
6	Regional Distribution of Aerosol over Land derived from ATSR-2 and GOME data	75
6.1	Introduction	76
6.2	Aerosol Remote Sensing Methods	77
6.2.1	Aerosol Model	77
6.2.2	Radiative Transfer Model	78
6.2.3	The ATSR-2 dual view algorithm	79
6.2.4	GOME UV method	81
6.2.5	Cloud detection in ATSR-2 images	82
6.3	Observational Data	83
6.4	Results	83
6.4.1	ATSR-2 retrieval	83
6.4.2	GOME retrieval	86
6.4.3	Back-Trajectories	91
6.5	Summary and Conclusions	92
6.6	Acknowledgments	92
	Bibliography	92
7	Comparison of Aerosol Satellite Remote Sensing and a 3D chemical transport Model	95
7.1	Introduction	96
7.2	Modeling the Sulfur Cycle using the TM3 model	97
7.3	Modeling the Aerosol Optical Depth	98

7.4	GOME UV Aerosol Retrieval	100
7.5	Observational Data	101
7.6	Results and Discussion	102
7.6.1	Timeseries	102
7.6.2	Spatial Correlation	104
7.7	Conclusions	113
7.8	Acknowledgments	115
	Bibliography	115
8	Concluding Remarks	117
8.1	Aerosol retrieval over the ocean	118
8.2	Aerosol retrieval over land	118
8.3	Application of aerosol retrieval	119
8.4	Future Outlook	120
A	List of Acronyms	121
	Summary	123
	Samenvatting	127
	Curriculum Vitae	131

Voorwoord

Dit proefschrift is het tastbare bewijs van vier jaar promotie-onderzoek. Hoewel dit boekje de bekroning vormt, is het proces wat hiertoe geleid heeft voor mij minstens even belangrijk. Dit traject wordt door iedere promovendus verschillend afgelegd. Er zijn er bij die aan het begin van hun onderzoek zo op een rijdende trein kunnen stappen. Bij mij was het omgekeerde het geval: er was geen rails, en er was geen trein. De grote uitdaging was het ontwerpen en bouwen van een eigen trein. Het bouwen begon met het vergaren van kennis. Hier en daar moest ook nog een wiel worden uitgevonden. Daarna werden alle onderdelen afzonderlijk getest. Dan het grote moment: voor het eerst zet de trein zich in beweging... en hij rijdt! Natuurlijk moet hij direct weer terug naar de werkplaats, want het kan altijd sneller, het kan altijd beter.

Nu de trein eenmaal rijdt, kan hij gebruikt worden om de wereld te ontdekken. Onderweg kom je nog anderen tegen. Soms mag je een stuk over iemand anders spoor, of mag je kijken in de machinekamer van een andere trein. Je leent eens wat onderdelen, dan weer neem jijzelf iemand mee. Het netwerk vertakt zich!

Als de trein dan eindelijk lekker op stoom is, dien je naar huis terug te keren. Men verlangt een verslag over hetgeen je gezien hebt tijdens je reizen. Maar eenieder weet dat het schrijven van reisverslagen minder leuk is dan het reizen zelf. Ook wil men een handleiding voor de besturing van jouw trein. Eenieder weet ook dat het schrijven van een handleiding nog saaier is dan het lezen ervan. Dan komt het eindstation in zicht. Je zet nog een keer flink wat druk op de ketel. Vol trots laat je zien hoe hard jouw trein wel niet kan. Je stapt voor het laatst uit. Iemand anders gaat nu met jouw trein verder. Nog één keer bewonder je de locomotief, voordat hij definitief vertrekt. Even ben je bedroefd als je terugdenkt aan die goede oude trein. Maar niet lang, want het volgende project wacht. Deze keer wordt het een vliegtuig!

Wanneer u door dit proefschrift bladert, komt u de namen tegen van velen die aan mijn trein een bijdrage hebben geleverd. Een aantal mensen wil ik met name bedanken. Allereerst mijn (co-)promotor Gerrit de Leeuw. Jij had altijd veel vertrouwen in mijn werk, en gaf mij alle vrijheid om mezelf te ontwikkelen. Ook wil ik Peter Bultjes bedanken. Hoewel jij niet belast was met de dagelijkse begeleiding, kon je wel goed aangeven waar de problemen lagen, wat mij geholpen heeft om overzicht te houden. Daarnaast wil ik Rob van Dorland en Hans Schrijver bedanken, die ook deel uitmaakten van het aerosol retrieval project.

Tijdens de regelmatige bijeenkomsten vormden jullie een prima klankbord.

It is a pleasure to thank Phil Durkee, Ken Davidson and all the other staff members of the meteorology department of the Naval Postgraduate School, for their hospitality during my visits to Monterey. Phil's expertise in satellite remote sensing was of great help when I first started in this field.

Daarnaast wil ik alle collega's van TNO-FEL bedanken, die in de afgelopen jaren een prettige omgeving hebben gevormd om in te werken. Voor mij was het van groot belang dat ik mensen om mij heen had die naar me wilde luisteren wanneer ik met een probleem zat, of wanneer ik dacht een goed idee te hebben. Tevens denk ik met veel genoegen terug aan de zeildagen, het karten en niet te vergeten het laser-questen. Graag wil ik ook mijn ouders bedanken, die mij altijd alle steun en mogelijkheden gegeven hebben. Zij gaven mij alle vrijheid en hebben mij geleerd daarmee om te gaan, iets wat mij tijdens mijn onderzoek zeer goed van pas kwam. Natuurlijk wil ik mijn vrienden hier niet vergeten. Helaas (of gelukkig?) heb ik hen nog niet kunnen overtuigen dat aerosolen het allerbelangrijkste zijn in het leven.

Als laatste wil ik Madelon bedanken. Talloze keren heb je mijn mooie plaatjes moeten bewonderen. Door de rust die je mij gaf, is jouw bijdrage aan dit proefschrift veel groter dan je denkt!

Pepijn Veefkind, juli 1999.

Chapter 1

Introduction and Overview

1.1 Introduction

Perhaps the most important message from an atmospheric scientist to the public and to the policy makers should be that man is changing the atmosphere rapidly. Changing the atmospheric chemical composition will have large effects on the human environment. The best known examples of such effects are the predicted global warming due to the anthropogenic emission of greenhouse gases and the depletion of the ozone layer due to the emission of man-made CFC's. While these subjects have been given much attention, it is less well known that the concentration and chemical composition of airborne particles, so-called aerosols¹, have changed as well. This is even more remarkable when it is realized that the perception of air pollution that we are most familiar with is smog: the reduction of visibility due to the increased aerosol concentration. Besides visibility reduction, effects of aerosols include direct health effects, acid deposition, climate effects, and effects on atmospheric chemistry.

In the 1970s and 1980s most of the interest in atmospheric aerosols was because of their direct health effects and their effects on visibility. In the large urban regions in the United States, Europe, and Japan the aerosol concentration was increasing rapidly due to human activities. It was realized that these increased aerosol levels can cause direct health problems such as respiration problems, chronic bronchitis, and a depletion of the lung function. Also, the relation between the increased aerosol concentrations and the decreased visibility was studied. Related to the visibility reduction is the effect of aerosols on the performance of electro-optical sensor systems. Knowledge of the aerosol optical properties can be used to predict the detection range of such systems.

Over the last decade, there has been increased interest in the role of aerosols in climate and atmospheric chemistry. Aerosols affect climate by scattering and absorbing the incoming solar radiation, and by their effect on the albedo and lifetimes of clouds. Due to the complex relation between the aerosol properties

¹a definition of aerosols will be given in section 1.2

and the Earth's radiation balance, and the lack of data on aerosols on a global scale, aerosols are considered one of the largest uncertainties in today's climate modeling. The role of aerosols in atmospheric chemistry was dramatically shown by the depletion of the stratospheric ozone layer following the eruption of the Mt. Pinatubo in 1992. It was realized that chemical reactions in the atmosphere are not limited to the gas phase, but also occur on the surface of clouds droplets and aerosols particles.

Aerosol properties can be measured on regional to global scales by satellite remote sensing, which is the focal point of this thesis. Satellite remote sensing will contribute to a better understanding of the aerosol distribution and transport in general; in this thesis it will be discussed in the context of climate change.

1.2 Atmospheric Aerosols

An aerosol is defined as a system of particles, solid or liquid, in gaseous suspension. By definition the atmosphere itself is thus an aerosol. However, in atmospheric physics, the term "aerosol" is often used interchangeable with "aerosol particle". In this terminology, atmospheric aerosols are all the particles in the atmosphere larger than a few molecules and smaller than cloud droplets. In practice, the atmospheric aerosol particles have diameters ranging from 1×10^{-3} to $100 \mu\text{m}$. Aerosol particles can be emitted as particles (primary sources), for example soil dust and sea salt particles, or formed in the atmosphere from precursor gases such as SO_2 and NO_x (secondary sources). Some of the aerosol sources are clearly of natural origin, e.g., volcanic emissions and sea spray from the oceans; other sources, such as sulfate and nitrate particles resulting from fossil fuel burning, are clearly anthropogenic. There are also sources, e.g., biomass burning and soil dust emissions, where both natural and anthropogenic sources contribute. Often it is very hard to distinguish between anthropogenic and natural contributions to these sources.

Whereas most of the natural sources of aerosols can be expected to have changed only moderately over the last centuries, anthropogenic sources have grown dramatically during the 20th century. Industrial sulfate emissions have doubled since 1950, following a slow increase over the preceding 100 years. Emissions from biomass burning have undergone a steady increase over the last 150 years. Note that in this respect, natural emissions caused by eruptive volcanoes represent a special case, because of their highly variable and short temporal source strength.

The removal of aerosol particles from the atmosphere is achieved by precipitation ("wet deposition") or by direct uptake by the Earth's surface ("dry deposition"). The efficiency of these processes is strongly dependent upon particle size, especially for particles with diameters between 0.1 and $10 \mu\text{m}$. For particles in the diameter range 0.1 - $1 \mu\text{m}$, the most important sizes as far as climate impact is concerned, wet deposition is the dominant sink process.

The time spent in the atmosphere by an aerosol particle is a complex function

of its physical and chemical characteristics (size, hygroscopic properties, etc.), and the time and location of its release. The lifetime of sub-micron aerosol particles in the lower troposphere is estimated to be of the order of days to a week. Due to these short lifetimes, together with the many different sources with different spatial extents and emissions, the aerosol is highly variable in both space and time. This applies to the concentration, the size distribution, and to the chemical composition, and therefore also to the impact of aerosols on climate. The influence of the main source regions (Europe, North America, and China for industrial aerosols; South America and African Savanna for biomass burning aerosols; and Sahara and Central Asia for mineral dust) is thus primarily manifested within their immediate vicinity.

1.3 Climate Forcing

The driving force of the Earth's climate is absorption of solar radiation at the surface, and, to a lesser extent, by the atmosphere. The absorption of solar (shortwave) radiation is balanced by the outgoing thermal infrared (longwave) radiation. Climate forcing is the change in either shortwave or longwave radiation imposed on the Earth's radiation balance, driving the climate system to a new thermal equilibrium. Over the industrial period, the concentration of infrared absorbing gases such as carbon dioxide and methane have changed substantially. As indicated in Figure 1.1, the climate forcing of the anthropogenic greenhouse gases, the so-called enhanced greenhouse effect, is estimated to be approximately $+2.5 \text{ Wm}^{-2}$.

Over the last decade, anthropogenic aerosols have been recognized as another major anthropogenic perturbation of climate. Atmospheric aerosols exert both a direct and an indirect forcing on climate: directly by scattering and absorption of incoming solar radiation, and indirectly by their effect on the albedo and lifetimes of clouds. As is indicated in Figure 1.1, the climate forcing by both the direct and indirect effect is significant on a global scale. Owing to their short lifetimes, the climate effect of anthropogenic aerosols will be concentrated downwind of their source regions. In these areas, the climate forcing by anthropogenic aerosols can balance, or even exceed the climate forcing by the man-made greenhouse gases. In spite of the importance of aerosols for the Earth's radiation balance, the uncertainties in the estimates of the aerosol forcing is large. Aerosols are considered one of the largest uncertainties in today's climate modeling. These large uncertainties are caused by the complexity of the aerosol climate effects as compared to the forcing by the well-mixed greenhouse gases, and the lack of data on a global scale. The climate effects of aerosols are more complex because the aerosol forcing depends not only on the concentration but also on the size and the chemical composition. Furthermore, due to the short lifetimes, their spatial distribution is highly inhomogeneous and strongly correlated with their sources.

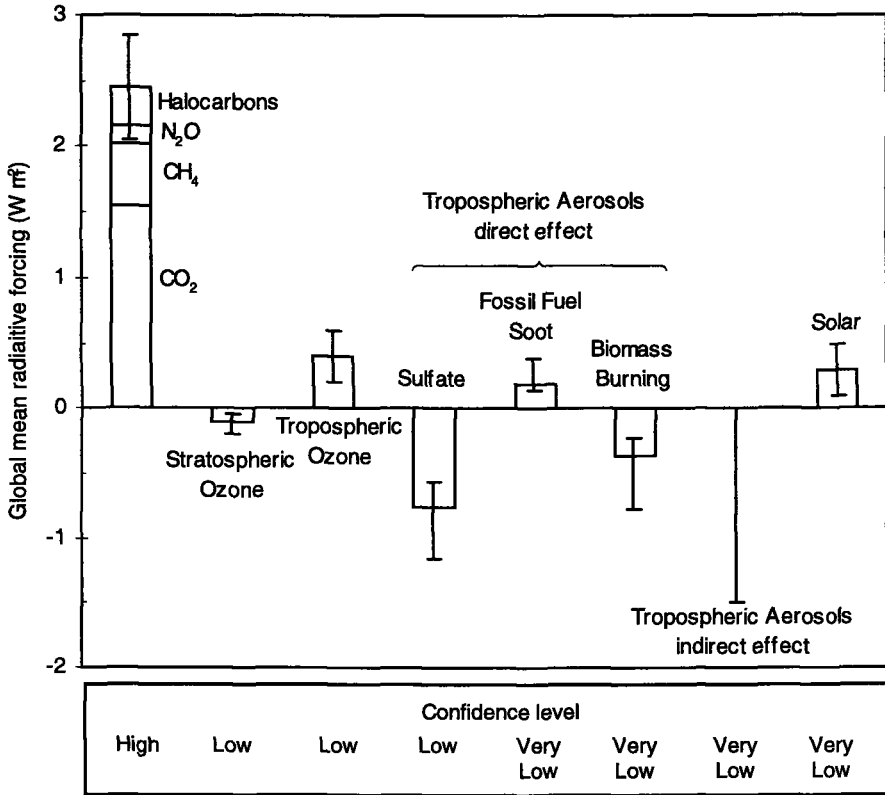


Figure 1.1: Estimated magnitudes and uncertainties of anthropogenic contributions to radiative forcing of climate (source: IPCC [1995]).

1.3.1 Direct Aerosol Forcing

In a pioneering study Charlson et al. [1992] estimated the magnitude of the direct forcing due to anthropogenic sulfate aerosols. They used a combination of a simple radiative transfer model and a chemical box-model describing mass balance. This model yields for the area-average shortwave forcing $\overline{\Delta F_R}$ resulting from an increase in sulfate aerosol concentration:

$$\overline{\Delta F_R} = -\frac{1}{2}F_T(1 - A_c)T_a^2(1 - R_s)^2\bar{\beta}\alpha_{SO_4^2-}f(RH)\overline{B_{SO_4^2-}} \quad (1.1)$$

where:

F_T is the solar constant, the mean solar irradiance at the top of the atmosphere;

A_c is the fractional cloud cover;

T_a is the fraction of the incoming light transmitted by the atmosphere above

Quantity	Value	Units	Uncertainty factor
F_T	1370	Wm^{-2}	-
$1 - A_c$	0.4		1.1
T_a	0.76		1.15
$1 - R_s$	0.85		1.1
$\bar{\beta}$	0.29		1.3
$f(RH)$	1.7		1.2
$\alpha_{SO_4^{2-}}$	5	m^2g^{-1}	1.8
$\overline{B}_{SO_4^{2-}}$	3.8	10^{-3} gm^{-2}	1.8
ΔF_R	-1.1	Wm^{-2}	2.4

Table 1.1: Evaluation of global mean direct forcing by anthropogenic sulfate aerosol, modified after Schwartz [1996]

the aerosol layer;

R_s is the mean surface albedo of the underlying surface;

β is the fraction of the radiation scattered upward by the aerosol;

$f(RH)$ is the relative increase in the scattering coefficient due to relative humidity (RH) above a reference value;

$\alpha_{SO_4^{2-}}$ is the light-scattering mass efficiency of sulfate aerosol, i.e. scattering coefficient per sulfate mass at low relative humidity ($RH = 30\%$);

$\overline{B}_{SO_4^{2-}}$ is the mean column burden of sulfate resulting from anthropogenic emissions.

Equation (1.1) can also be expressed in terms of the aerosol optical depth (AOD), using $AOD = \alpha_{SO_4^{2-}} f(RH) \overline{B}_{SO_4^{2-}}$.

The negative sign in equation (1.1) denotes that the forcing represents a cooling tendency. The factor $\frac{1}{2}$ is introduced because only half of the Earth is illuminated at a given time. Although more sophisticated descriptions of the direct aerosol forcing have been published since, equation (1.1) gives much insight in the variables controlling the direct forcing. Equation (1.1) indicates that the mean radiative forcing is directly proportional to the column burden of sulfate aerosol. Except for the column burden of aerosol mass, other microphysical parameters controlling the forcing are: the light-scattering efficiency, the increase of light scattering with increasing RH , and the upward scattered fraction. These variables are determined by the aerosol size distribution and the chemical composition. In Table 1.1 global mean values for the variables controlling the direct sulfate forcing are evaluated. From the values given in Table 1.1, the magnitude of the global mean direct radiative forcing is estimated as -1.1 Wm^{-2} . Also given in Table 1.1 is the uncertainty factor. The overall uncertainty factor is estimated as 2.4, i.e. the mean direct forcing is estimated between -0.5 and -2.6 Wm^{-2} . The key sources of uncertainty are the microphysical factors (scattering efficiency, upward scattered fraction, and dependence of the scattering on the

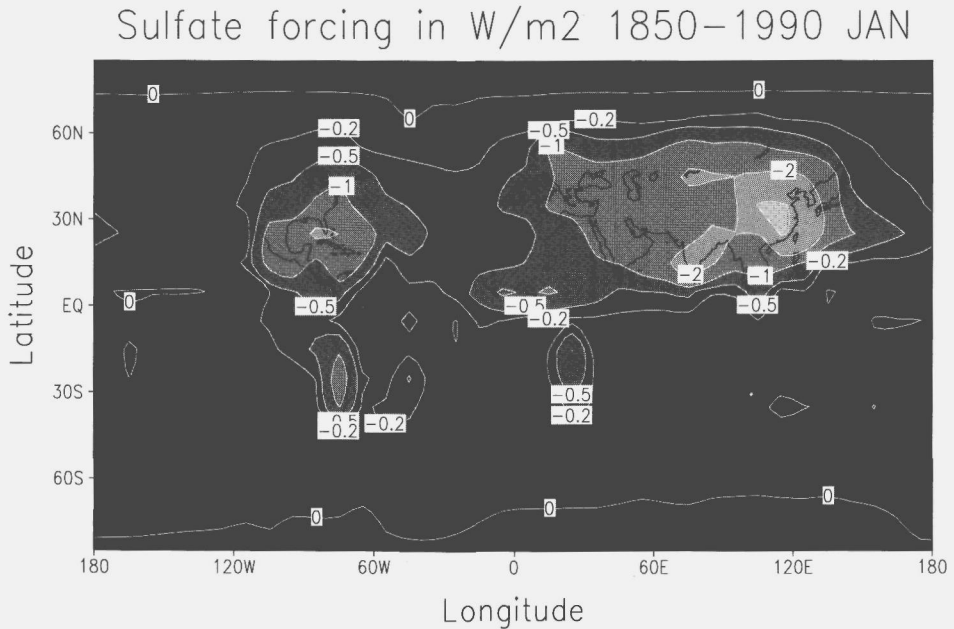


Figure 1.2: January average of direct radiative forcing (in Wm^{-2}) due to tropospheric anthropogenic sulfate aerosol changes since pre-industrial times (1850-1990). Adapted from Van Dorland et al. [1997].

RH), and the atmospheric chemistry factors determining the column burden of sulfate aerosol.

In contrast to most of the greenhouse gases, the lifetimes of atmospheric aerosols in the troposphere is short. Together with the highly non-uniform distribution of aerosol sources, this results in very different geographical patterns of radiative forcing by aerosols and greenhouse gases. The direct forcing by anthropogenic aerosols will be at its maximum downwind of the large industrialized regions. Figure 1.2 illustrates the highly non-uniform direct forcing by anthropogenic sulfate aerosols. Because the vast majority of the anthropogenic sources is situated on the northern hemisphere, the direct aerosol effect will cause a large hemispheric difference in radiative forcing of climate.

Above the direct radiative forcing by anthropogenic sulfate aerosols was evaluated. It is noted that sulfate is not the only anthropogenic aerosol contributing significantly to direct radiative forcing. Chemical analysis of anthropogenic aerosol shows that the organic aerosols and ammonium nitrate aerosols can contribute equally or even exceed the contribution of sulfate aerosols to scattering [Hegg et al., 1997, ten Brink et al., 1996]. Sulfate was discussed here as an example, because it is much better understood than other types of aerosol.

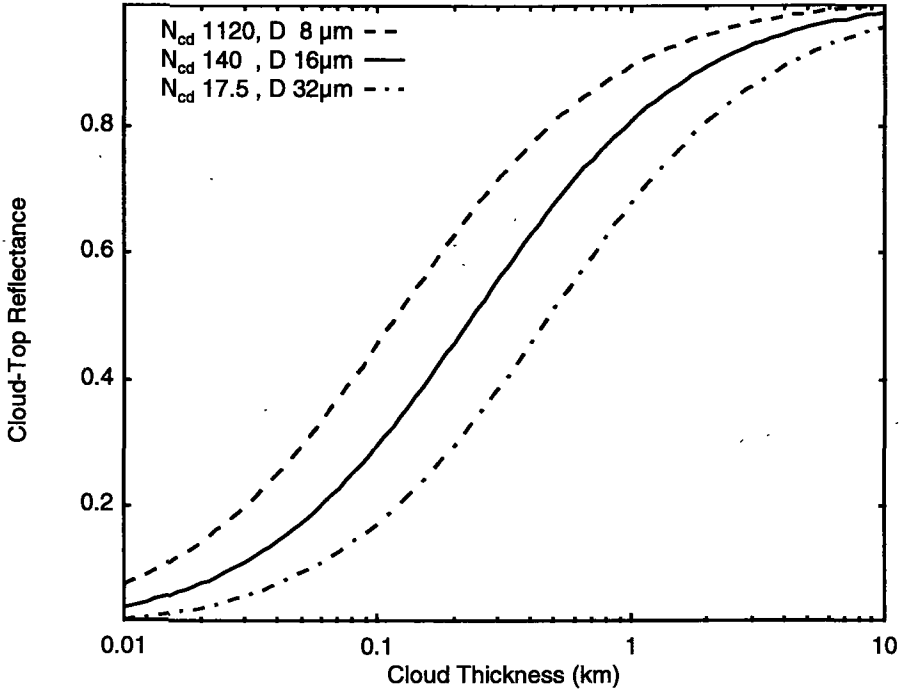


Figure 1.3: Dependence of cloud-top reflectance on cloud thickness for liquid water volume fraction of 0.3 cm^3 and indicated values for the cloud droplet number concentration N_{cd} . Note that the sensitivity for an eightfold increase/decrease in cloud droplet number concentration is largest for clouds of intermediate reflectance (source: Schwartz and Slingo, [1996]).

1.3.2 Indirect Aerosol Forcing

In addition to the direct effect, aerosols also affect the Earth's radiation balance by modifying the properties of clouds. Cloud formation occurs when water vapor condensates on cloud condensation nuclei (CCN). Anthropogenic aerosols usually contain relatively large amounts of water soluble material, and thus can act as CCN. Increasing the CCN concentration will result in clouds with more, but smaller, cloud droplets. Also, there is evidence that the lifetime of clouds increases with the cloud droplet concentration [Albrecht, 1989]. Although the mechanisms of indirect aerosol forcing is understood relatively well, it is very hard to quantify the indirect aerosol effect.

Figure 1.3 illustrates the dependence of the cloud top reflectance on the cloud droplet concentration. The sensitivity of the cloud top reflectance to an increase/decrease in the cloud droplet concentration is largest for clouds with cloud top reflectance around 0.5. The relative increase to a change in cloud droplet concentration is largest for clouds with an intermediate cloud top reflectance,

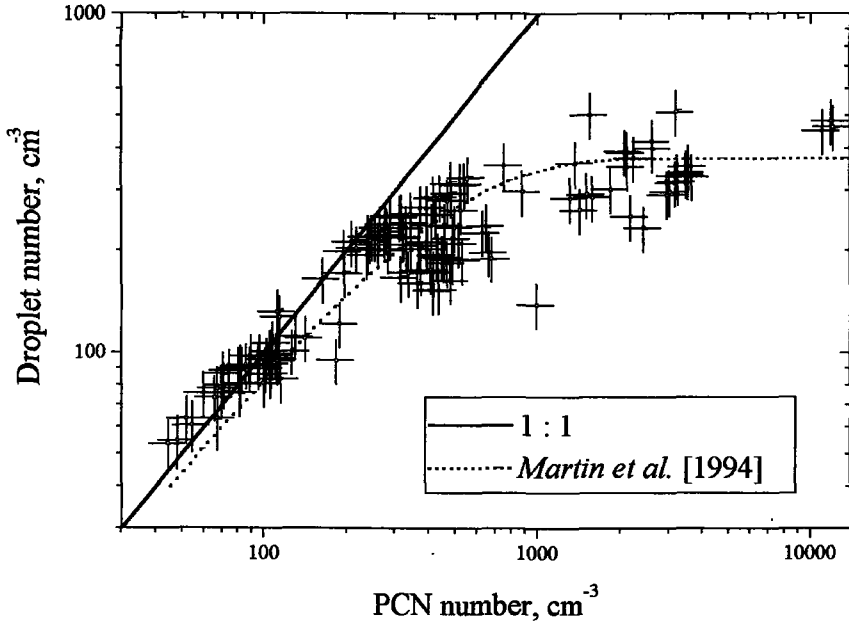


Figure 1.4: Droplet number concentration as a function of the potential condensation nuclei (PCN) concentration. Adapted from Khlystov [1998].

which is typical for marine stratus and stratocumulus clouds. Assuming a 30 % increase in cloud droplet concentration, Charlson et al. [1991] estimated the indirect aerosol forcing for the Northern hemisphere as -1.1 Wm^{-2} . This estimate clearly illustrates the potential of indirect aerosol forcing.

Relating the cloud droplet concentration to aerosol properties is complex, since it depends on the meteorological conditions, such as the updraft velocity and the mixing in the clouds, as well as on the ability of aerosol particles to act as CCN. The ability to act as CCN depends not only on the size distribution and the chemical composition of the particles, but also on the supersaturation in the cloud. The peak supersaturation in clouds seldom exceeds 0.05%. At this supersaturation only particles with dry diameters larger than approximately $0.1 \mu\text{m}$ get activated. Therefore, the concentration of aerosol particles larger than this diameter is important for assessing the aerosol indirect forcing. Figure 1.4 shows the droplet number concentration as a function of the number of particles that are larger than the activation threshold (the potential condensation nuclei). Based on this relation between the aerosol number concentration and the number of cloud droplets Khlystov [1998] estimated the indirect forcing by anthropogenic aerosols in the Netherlands as $-6.5 \pm 2.5 \text{ Wm}^{-2}$.

1.3.3 Modeling Needs

To fully describe the aerosol's radiative impact on climate the following information should be available [Lacis and Mishchenko, 1995]:

- the optical constants (complex refractive index) for the chemical compounds contained in aerosols, at all relevant wavelengths;
- the chemical composition, particle shape, and size distribution of aerosols species;
- a physical model to describe the effect of hygroscopical particle growth with changing relative humidity on the aerosol optical properties;
- a cloud microphysical model to determine changes in cloud droplet size, cloud optical depth, and lifetimes in response to changes in the CCN concentration.

It is clear that such information is not available on a global scale. In fact, most of the data available on aerosol properties is measured during short-term campaigns, which might not be relevant for other regions or other seasons, or even other conditions than encountered during the measurement campaign. Frequent global monitoring of aerosol properties is only achievable by satellite remote sensing. However, satellite remote sensing is limited to the aerosol optical properties. Therefore a combined effort of satellite remote sensing, short-term intensive field observations, and three-dimensional chemistry transport modeling is needed to adequately describe the aerosol's impact on climate.

1.4 Aerosol Satellite Remote Sensing

To understand the effects of aerosols on climate, the spatial distribution of aerosols should be known accurately. Because of the short lifetimes of aerosols in the troposphere, the aerosol is highly variable in both space and time. Only satellite remote sensing has the potential to measure the highly variable aerosol field on global scales during longer periods [IPCC, 1995].

Aerosol particles scatter and absorb solar radiation, thus modifying the radiation field. It was early recognized that the solar radiation backscattered to space was influenced by the aerosol and could be analyzed to determine aerosol properties. The first applications of satellite remote sensing date back to the mid-1970s and concerned the detection of desert dust over the ocean [Griggs, 1975, Fraser, 1976]. The correction of aerosol influence on the remote sensing of ocean color was considered by Gordon [1978]. Because the albedo of the ocean is low and relatively well-known, most aerosol satellite remote sensing studies have focused on the retrieval of aerosol properties over the ocean [Durkee et al., 1991, Husar et al., 1997]. The first studies on the detection of aerosols over land concerned the atmospheric corrections of land surface images [Tanré et al., 1979].

Sensor/ Satellite	VIS/NIR channels (μm)	Spatial Resolution (km^2)	Swath Width (km)	Comments
AVHRR NOAA	0.64, 0.84	1-4	2000	No inflight calibration Water vapor absorption
ATSR-2 ERS-2	0.555, 0.659, 0.865, and 1.6	1-4	512	Inflight calibration Dual view capability
GOME ERS-2	Continuous in 0.240 - 0.790	320 \times 40 or 80 \times 40	960 or 240	Spectrometer

Table 1.2: Characteristics of the satellite sensors used in this work. Only the channels in the visible (VIS) and near-infrared (NIR) are listed.

Until recently, satellite sensors that were used in aerosol retrieval were not designed for this task. Satellite remote sensing requires well-calibrated multi-spectral sensors. These sensors should have narrow spectral bands to avoid the water vapor absorption regions [Kaufman, 1995]. Since recently, data from sensors more suitable for aerosol retrieval is becoming available. Not only do these sensors have more spectral information and a better calibration, also new concepts are being tested. These new concepts include spaceborne spectrometers with high spectral resolution, radiometers viewing the Earth from different angles, and the capability of measuring the degree of polarization. Using these new opportunities more aerosol parameters can be determined. To fully utilize the possibilities of these new sensors, new aerosol retrieval algorithms have to be developed. These algorithms should be validated during intensive field campaigns and applied to the global data sets. The global aerosol data sets should be used in climate models to reduce the large uncertainties in the effect of anthropogenic aerosols (Figure 1.1). In addition, satellite remote sensing can also be used in field-campaigns, to determine if conditions encountered in ground based (point) measurements are valid for a larger region. As satellite remote sensing provides information on aerosol properties on regional scales, they can be very important in the validation and improvement of three-dimensional chemical transport models.

1.5 Satellite Sensors

In this work, data is presented from three satellite sensors: the Advanced Very High Resolution Radiometer (AVHRR), the second Along Track Scanning Radiometer (ATSR-2), and the Global ozone Monitoring Experiment (GOME). Table 2.1 shows an overview of the characteristics of these sensors. In Figure 1.5 the wavelength range of these sensors is presented graphically.

The AVHRR is a radiometer aboard the NOAA satellites [Kidwell, 1997]. The first AVHRR was launched in 1979, since then at least one AVHRR sensor

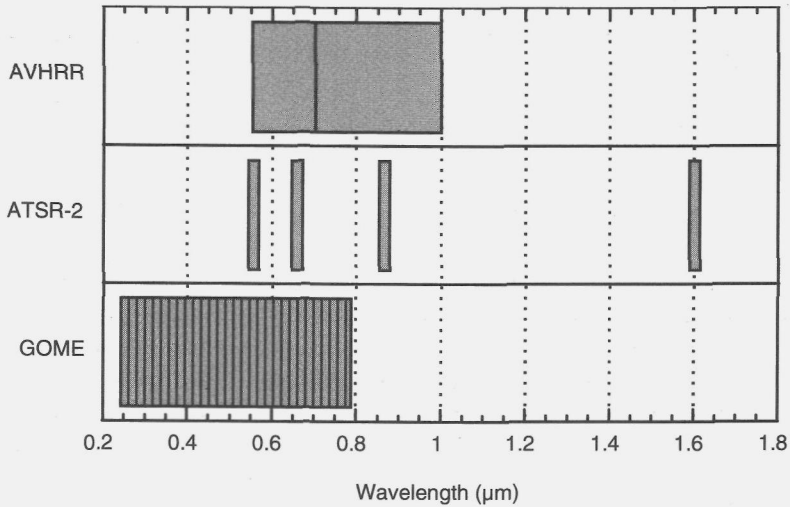


Figure 1.5: Spectral channels in the visible and near-infrared for the AVHRR, the ATSR-2, and GOME.

has been in orbit. The spatial resolution of the AVHRR sensors is 1.1 km^2 at nadir, and the swath width is approximately 2000 km. With this large swath width, the AVHRR provides daily global coverage. The AVHRR has four spectral bands, of which there are two in the visible and near-infrared. The effective wavelength of these two bands are $0.64 \text{ }\mu\text{m}$ for Channel 1, and $0.84 \text{ }\mu\text{m}$ for Channel 2. With a spectral width of 0.15 and $0.20 \text{ }\mu\text{m}$, respectively, these bands are very broad. The AVHRR has no inflight calibration facility for Channel 1 and 2.

The ATSR-2 is a radiometer aboard the European ERS-2 satellite, which was launched in April 1995 [RAL, 1996]. The ATSR-2 has seven spectral bands, four of these bands are in the visible and near-infrared (effective wavelengths 0.555 , 0.659 , 0.865 , and $1.6 \text{ }\mu\text{m}$). In-flight calibration of these channels is performed by measuring the solar irradiance during parts of the orbit. The spatial resolution is 1.1 km^2 at nadir, and the swath width is 512 km. The ATSR-2 has a conical scanning mechanism, providing two images for each location, measured at nadir and at an viewing zenith angle of approximately 55° along track. The timespan between these two images is about two minutes.

Besides the ATSR-2, the ERS-2 satellite also carries the spectrometer GOME. GOME is a four-channel grating spectrometer, which measures from $0.240 \text{ }\mu\text{m}$ to $0.790 \text{ }\mu\text{m}$, with a spectral resolution of 0.2 to 0.4 nm [ESA, 1995]. The default spatial resolution is $320 \times 40 \text{ km}^2$. However, the spatial resolution can be improved to $80 \times 40 \text{ km}^2$. Since June 1997, these smaller pixels are used for three

days per month. Each scan line consist of three pixels, thus the swath with of GOME is 960 km for the default pixels, and 240 km for the smaller pixels. To be able to correct for the polarization sensitivity of GOME, polarization is measured by so-called polarization measuring devices (PMDs). For calibration purposes the Sun is observed via a diffuser plate once per day. Spectral calibration is performed using an onboard spectral line lamp.

1.6 Aim of this Work

On board the European ERS-2 satellite, which was launched in April 1995, two instruments are available that can be used for aerosol retrieval. The Along Track Scanning Radiometer (ATSR-2) is a two-angle view radiometer with 7 wavelength bands. The Global Ozone Monitoring Experiment (GOME) is a spectrometer with a very high spectral resolution. Both instruments have a unique new concept. To use these instruments for determining aerosol properties such as aerosol optical depth and size distribution, new aerosol retrieval algorithms must be developed and validated. The new and innovating concepts of both ATSR-2 and GOME make it possible to extract more aerosol information from the data than thus far possible. Also, it is a challenge to combine information from GOME and ATSR-2 in so-called sensor synergy studies to improve the retrieval of aerosol properties.

Satellite remote sensing of aerosol properties is an example of an ill-conditioned problem, with too little experimental parameters. The other required parameters are provided through the use of models. However, these are not perfect and it is therefore of crucial importance to extensively validate the aerosol retrieval algorithms. This is best possible in so-called column closure experiments, during which the key physical parameters are determined using several independent methods. Validation in these column closure experiments permits the assessment of measurement uncertainty. Good results help establish credibility for satellite remote sensing of aerosol properties. Several of these column-closure studies will be described in this thesis.

Besides the development and validation, also the application of satellite aerosol retrieval during a number of case studies will be described. Satellite aerosol retrieval can be used to derive aerosol fields on a regional scale. In combination with meteorological data and transport models, it can be used to derive the emission, transport, and deposition of aerosols. This information can be used in climate models and three-dimensional chemical models, to improve our understanding of the atmosphere and the effects of human activities.

1.7 Outline of this thesis

In Chapter 2 of this thesis the theory of remote sensing of aerosol properties will be discussed. It will be shown how the aerosol optical properties are determined by the size distribution and the chemical composition of the particles. Also, the

effects of aerosols on the satellite measured radiance will be discussed.

Chapter 3 and 4 will be dedicated to the retrieval of aerosol properties over the ocean. In Chapter 3 a description of the algorithm will be given, as well as sensitivity assessment and a first validation. Most of this chapter was published in the *Journal of Aerosol Science* (Vol. 29 No. 10, pp. 1237-1248, 1998). In Chapter 4 the algorithm will be compared to airborne measurements during a column closure experiment. This chapter appeared in the *Journal of Geophysical Research* (Vol. 104 No. D2, pp. 2253-2260, 1999).

Chapters 5 and 6 will be dealing with aerosol satellite retrieval over land. In Chapter 5 the two-angle view retrieval algorithm will be described, together with the validation in a column closure experiment. This chapter was published in the *Geophysical Research Letters* (Vol. 25 No. 16, pp. 3135-3138, 1998). In Chapter 6, aerosol retrieval in the UV will be introduced, and different methods for aerosol retrieval over land will be discussed. For a case study over northwestern Europe, the regional distribution derived from satellite data and the results will be discussed in terms of regional sources and transport. This chapter was submitted to *Remote Sensing of the Environment* in January 1999.

In Chapter 7 satellite retrieval results are compared to results of a three-dimensional chemical transport, over Europe for August 1997. Satellite retrieval can be used for validation of such models. The models can be applied for interpretation of the observed spatial aerosol distribution.

In Chapter 8 final remarks and conclusions will be given, together with recommendations concerning future work.

Bibliography

- Albrecht, B. A. (1989). Aerosols, cloud microphysics, and fractional cloudiness. *Science*, 262:226-229.
- Charlson, R. J., Lagner, J., Rodhe, R., Leovy, C. B., and Warren, S. G. (1991). Perturbation of the northern hemisphere radiative balance by backscattering from sulfate aerosols. *Tellus*, 43AB:152-163.
- Charlson, R. J., Schwartz, S. E., Hales, J. M., Cess, R. D., Coackley, J. A. J., Hansen, J. E., and Hofmann, D. J. (1992). Climate forcing by anthropogenic aerosols. *Science*, 255:423-430.
- Dorland, R., Dentener, F. J., and Lelieveld, J. (1997). Radiative forcing due to tropospheric ozone and sulfate aerosols. *J. Geophys. Res.*, 102:28079-28100.
- Durkee, P. A., Pfeil, F., Frost, E., and Shema, R. (1991). Global analysis of aerosol particle characteristics. *Atmos. Environ.*, 24A:2457-2471.
- ESA (1995). Global ozone monitoring experiment users manual. Technical Report ESA SP-1182, ESA/ESTEC, Noordwijk, The Netherlands.
- Fraser, R. S. (1976). Satellite measurements of mass of saharan dust in the atmosphere. *Appl. Opt.*, 15:2471-2479.

- Griggs, M. (1975). Measurements of atmospheric aerosol optical thickness over water using erts-1 data. *Journal of the Air Pollution Control Association*, 25:622–626.
- Hegg, D. A., Livingston, J., Hobbs, P. V., Novakov, T., and Russell, P. B. (1997). Chemical apportionment of aerosol column optical depth off the mid-atlantic coast of the united states. *J. Geophys. Res.*, 102:25293–25303.
- Husar, R. B., Prospero, J. M., and Stowe, L. L. (1997). Characterization of tropospheric aerosols over the oceans with the noaa advanced very high resolution radiometer optical thickness operational product. *J. Geophys. Res.*, 102:16,889–16909.
- IPCC (1995). Radiative forcing of climate. In Houghton, J., Filho, L. G. M., Bruce, J., Lee, H., Haites, E., Harris, N., and Maskell, K., editors, *Climate change 1994*, pages 1–231. Cambridge UP, Cambridge.
- Kaufman, Y. J. (1995). Remote sensing of direct and indirect aerosol forcing, in: Aerosol forcing of climate. In Charlson, R. J. and Heintzenberg, J., editors, *Aerosol forcing of climate*, pages 297–332. John Wiley, New York.
- Khlystov, A. (1998). *Cloud forming properties of ambient aerosol in the Netherlands and resultant shortwave radiative forcing of climate*. PhD thesis, Wageningen Agricultural University.
- Kidwell, K. B. (1997). Noaa polar orbiter data users guide, aug. 1997 revision. Technical report, Natl. Oceanic and Atmos. Admin., Silver Spring, Md. (Available at <http://www2.ncdc.noaa.gov/docs/podug>).
- Lacis, A. A. and Mishchenko, M. I. (1995). Climate forcing, sensitivity and response. In Charlson, R. J. and Heintzenberg, J., editors, *Aerosol forcing of climate*, pages 11–42. John Wiley, New York.
- Martin, G. M., Johnson, D. W., and Spice, A. (1994). The measurement and parametrization of effective radius of droplets in warm stratiform clouds. *J. Atmos. Sci.*, 51:1823–1842.
- RAL (1996). ATSR-2 flight operations manual. Technical Report ER-MA-RAL-AT-2001, Rutherford Appleton Laboratory, Chilton, Didcot, UK.
- Schwartz, S. E. (1996). The whitehouse effect- shortwave radiative forcing of climate by anthropogenic aerosols, an overview. *J. Aerosol Sci.*, 27:359–382.
- Schwartz, S. E. and Slingo, A. (1996). Enhanced shortwave cloud radiative forcing due to anthropogenic aerosols. *NATO ASI series*, pages 191–236.
- Tanré, D., Herman, M., Deschamps, P. Y., and De, L. A. (1979). Atmospheric modeling for space measurements of ground reflectances including bi-directional properties. *Appl. Opt.*, 18:3587–3594.
- ten Brink, H. M., Veefkind, J. P., Waaijers-Ijpelaar, A., and van der Hage, J. C. H. (1996). Aerosol light-scattering in the netherlands. *Atmos. Environ.*, 30:4251–4261.

Chapter 2

Theory of Aerosol Satellite Remote Sensing

2.1 Introduction

Satellite sensors measure the top of the atmosphere (TOA) radiance. For a cloud-free atmosphere, the TOA radiance is caused by scattering by molecules and aerosols, and by reflection on the surface, as illustrated in Figure 2.1. Passive satellite remote sensing of aerosols analyzes the top of the atmosphere radiance to extract the aerosol optical properties. This is far from straightforward, because like most remote sensing problems, the problem of the retrieval of the aerosol properties from the TOA radiance is ill-posed, meaning that there are more unknowns than equations. To obtain a solution, assumptions have to be made on part of the unknowns. In aerosol satellite remote sensing these include assumptions on the reflectivity of the surface, the shape of the aerosol size distribution, and the chemical composition of the aerosol particles.

This chapter will focus on the background of aerosol satellite remote sensing. In section 2.2 the aerosol optical properties and their dependence on the aerosol particle characteristics are discussed. In section 2.3 the effects of aerosols on the TOA radiance are described.

2.2 Scattering and Absorption by Aerosols

2.2.1 Definitions

A parallel light beam passing through a layer in the atmosphere is attenuated by scattering and absorption by aerosol particles and gas molecules, see Figure 2.2. The attenuation from the initial intensity is described by the well-known Lambert-Beer law. The extinction coefficient σ_e is defined as the fraction of intensity lost from a collimated beam per unit of layer thickness, and is usually given in units of m^{-1} or km^{-1} . Since the attenuation of radiation is caused by

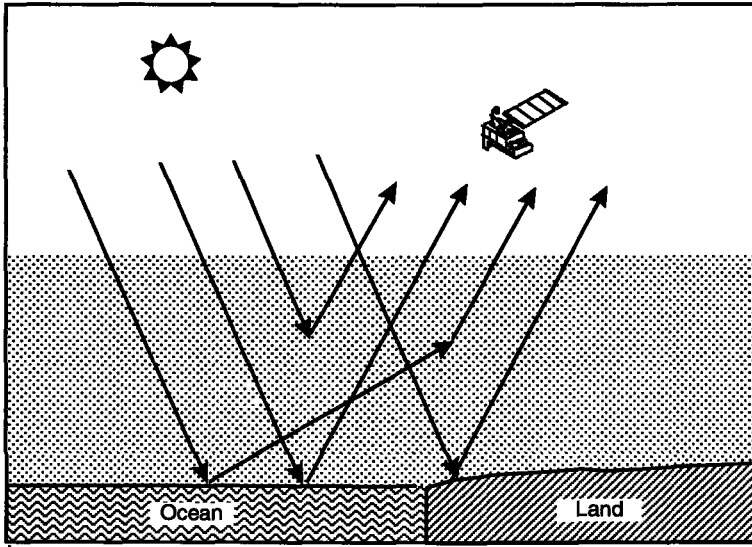


Figure 2.1: Schematic representation of the contributions to the top of the atmosphere radiance as measured by satellites. Photons can reach the satellite sensor by (multiple) scattering in the atmosphere, reflection on the surface, and combinations of atmospheric scattering and reflection on the surface. Because most aerosol retrieval algorithms consider only cloud free regions, no clouds are included in this figure.

both scattering and absorption, the extinction coefficient can be considered as the sum of the scattering coefficient σ_s , and the absorption coefficient σ_a :

$$\sigma_e(\lambda) = \sigma_s(\lambda) + \sigma_a(\lambda). \quad (2.1)$$

Note that the extinction, scattering and absorption coefficients are all dependent on the wavelength λ .

Both gases and aerosol are responsible for the scattering and absorption, and both processes are additive:

$$\sigma_s(\lambda) = \sigma_{sp}(\lambda) + \sigma_{sg}(\lambda), \quad (2.2)$$

and

$$\sigma_a(\lambda) = \sigma_{ap}(\lambda) + \sigma_{ag}(\lambda), \quad (2.3)$$

with scattering and absorption by particles denoted with subscripts 'p', and scattering and absorption by gas molecules denoted with subscripts 'g'.

The relative contribution of absorption to the extinction by aerosol particles is commonly expressed in terms of the aerosol single scattering albedo ω_0 , which

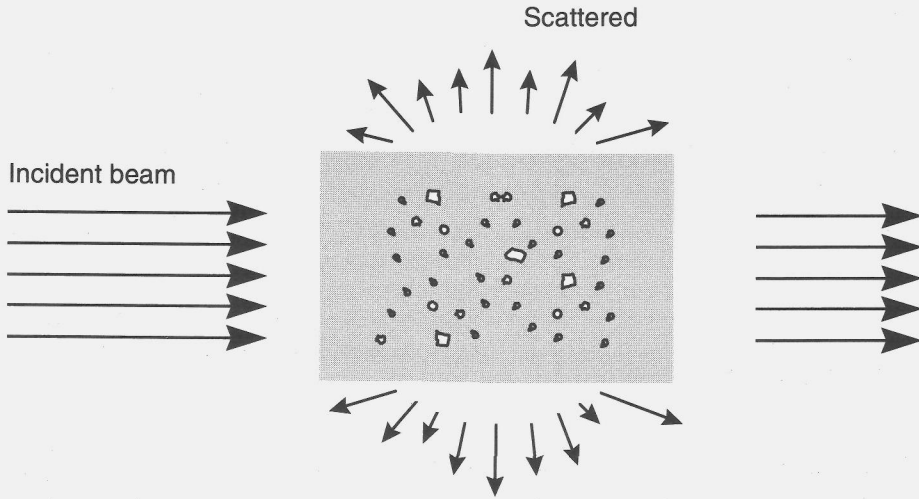


Figure 2.2: A parallel light beam passing through a layer consisting of air molecules and aerosol particles. The incident beam will be attenuated by scattering and absorption by both the molecules and the aerosol particles. The scattered light will be re-distributed over all directions.

is defined as the ratio between the particle scattering and particle extinction coefficient:

$$\omega_0(\lambda) = \frac{\sigma_{sp}(\lambda)}{\sigma_{ep}(\lambda)} \quad (2.4)$$

where σ_{ep} is the particle extinction coefficient. When $\omega_0 = 1$ all the extinction is caused by scattering, and when $\omega_0 = 0$ all the extinction is caused by absorption.

The total column aerosol optical depth (AOD), is defined as the aerosol extinction coefficient integrated over a vertical path from the ground to the top of the atmosphere:

$$AOD(\lambda) = \int_0^{TOA} \sigma_{ep}(\lambda, h) dh. \quad (2.5)$$

The angular distribution of the scattered photons is characterized by the phase function $p(\theta)$, where θ is the scattering angle, the angle between incidence and the scattering direction. As $p(\theta)$ is normalized over all scattering directions, it does not depend on the total aerosol concentration. Several parameters can be derived from the phase function to express the distribution of the scattered radiation. The asymmetry parameter g is often used in simplified radiative transfer calculations, that are implemented in climate models. The asymmetry parameter is the average cosine of the scattering angle:

$$g(\lambda) = \frac{1}{2} \int_0^\pi \cos(\theta) p(\lambda, \theta) \sin(\theta) d\theta. \quad (2.6)$$

Parameter	Polluted Continental	Clean Continental	Clean Marine
Aerosol Optical Depth	0.2 - 0.8	0.02 - 0.1	0.05 - 0.1
Single Scattering Albedo	0.8 - 0.95	0.9 - 0.95	close to 1
Scattering Coefficient ($1 \times 10^{-4} \text{ m}^{-1}$)	0.5 - 3	0.05 - 0.3	0.05 - 0.2
Back/Total Scattering	0.1 - 0.2	not available	0.15

Table 2.1: Typical range of aerosol optical properties of lower tropospheric aerosols. Values are for 0.500-0.550 μm wavelength at low relative humidity. Modified from IPCC [1995].

The asymmetry parameter g equals zero when the scattering is isotropic or symmetric about a scattering angle of 90° . If the scattering is completely directed into the forward direction ($\theta=0^\circ$) $g=1$, and $g=-1$ when the scattering is directed completely into the backward direction ($\theta=180^\circ$).

2.2.2 Aerosol Optical Properties

The aerosol particles are characterized by their shape, size, chemical composition, and total concentration, which in turn determine the aerosol optical properties. The typical range for the aerosol optical depth, the single scattering albedo, and the scattering coefficient, as observed in the lower troposphere, is given in Table 2.1. Also shown in Table 2.1 is the ratio between backscattered to total scattered light, which is used as a measure for the direction of the scattered light. For spherical particles, the extinction coefficient follows from the Mie theory:

$$\sigma_e = \int_0^\infty Q_e(x, m) \pi r^2 n(r) dr, \quad (2.7)$$

where Q_e is the extinction efficiency which is a function of the size parameter $x = 2\pi r/\lambda$, and the complex index of refraction m . The complex refractive index is determined by the chemical composition. $n(r) = dN/dr$ is the number size distribution of the N particles.

It is important to note that in equation (2.7) the extinction coefficient is determined by the scattering efficiency weighted by its geometrical cross section πr^2 . Therefore, the number size distribution $n(r)$ that is commonly used to describe the size distribution in aerosol models, does not contain much information on the size range contributing most to the scattering coefficient. Hansen and Hovenier [1974] have shown that the parameter that best describes the radiative properties of a given size distribution is the effective radius r_e , defined as:

$$r_e = \frac{\int_0^\infty r^3 n(r) dr}{\int_0^\infty r^2 n(r) dr}. \quad (2.8)$$

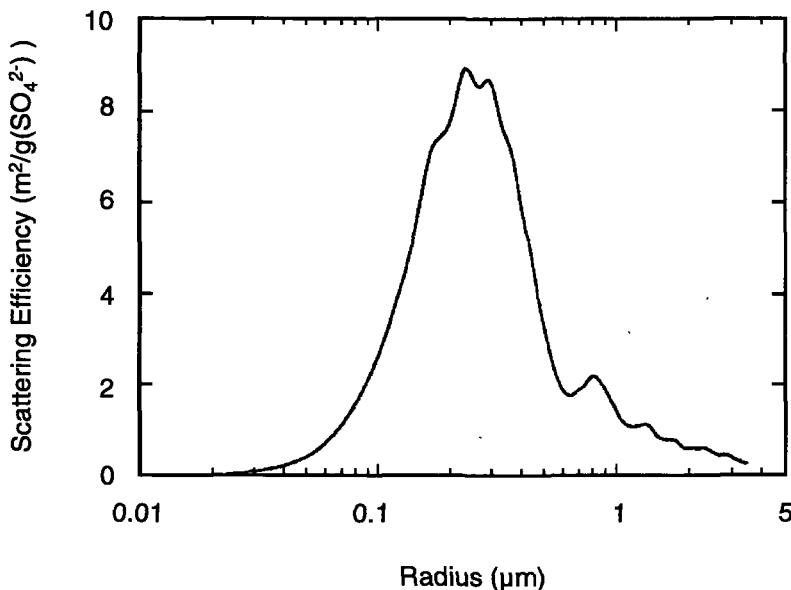


Figure 2.3: Dependence of the scattering efficiency of ammonium sulfate on particle size. The wavelength is $0.53 \mu\text{m}$; index of refraction 1.53. The scattering efficiency is expressed as the scattering coefficient per unit of mass SO_4^{2-} . (Source: Schwartz [1996]).

The effect of particle size on the scattering efficiency is shown in Figure 2.3. Here, the scattering per unit of sulfate mass of ammonium sulfate particles is plotted as a function of the particle radius. The mass scattering efficiency is largest when $x = \frac{2\pi r}{\lambda} \approx 1$, i.e. when the diameter of the particles is similar to the wavelength of the light. Anthropogenic aerosol particles produced by fossil fuel combustion, such as sulfates and nitrates, have diameters in the size range between diameters of 0.1 and $1 \mu\text{m}$. For shortwave solar radiation, these aerosols are thus in the size range with the highest scattering efficiency, see Figure 2.3. Sea salt and soil dust particles usually have diameters $>1 \mu\text{m}$ and therefore scatter the shortwave radiation less effectively.

Particle size is not only important for the scattering efficiency, it also affects the phase function, as illustrated in Figure 2.4. When the diameter of the particle is small as compared to the wavelength of the light, the phase function is symmetric in the forward and backward directions, but with increasing particle size the light is more scattered into the forward direction. For large particles, scattering is more concentrated in scattering angles between 0 and 30° , and in scattering angles between 150 and 180° .

Because most of the aerosol particles consist of hygroscopic material, their size, and therefore their optical properties will depend on the relative humidity (RH) of its surroundings. A large portion of the hygroscopic aerosols consists

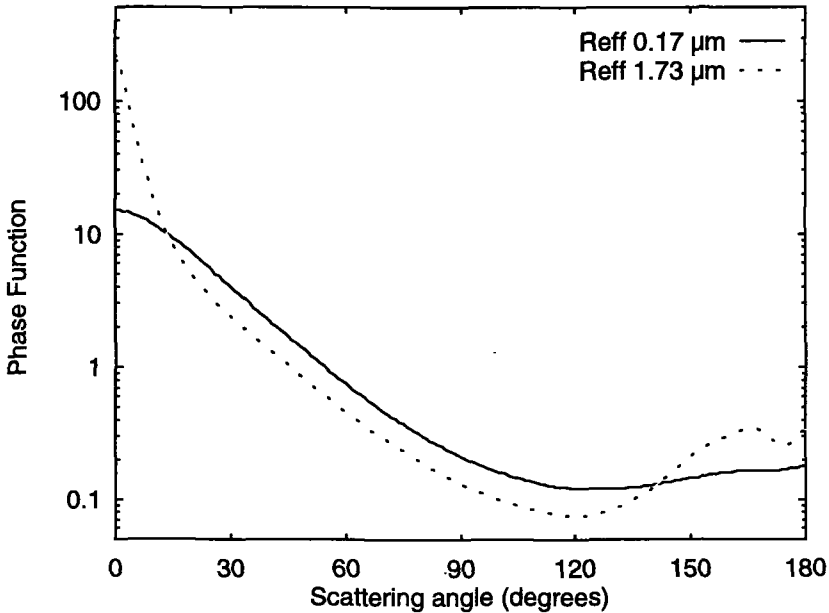


Figure 2.4: Phase functions calculated for lognormal aerosol size distributions with an effective radius of $0.17 \mu\text{m}$, and $1.73 \mu\text{m}$, respectively. The wavelength is $0.55 \mu\text{m}$, and the complex refractive index is $1.4 - 0.005i$. The small size distribution (effective radius $0.17 \mu\text{m}$) is typical for anthropogenic aerosols; the large size distribution (effective radius $1.73 \mu\text{m}$) is typical for stationary marine aerosols. [Gathman, 1983]

of salts such as ammonium sulfate, ammonium nitrate, and sea salt. The size change with changing RH of these salt particles follows a hysteresis curve. When the RH is increased starting at a low value, the particles do not grow until the RH reaches the so-called deliquescence point. Above the deliquescence point the particle grows gradually with increasing RH. Once the particle has been exposed to a RH above the deliquescent point it remains in the supersaturated state when the RH drops below the deliquescent state. This supersaturated state was found to prevail in the atmosphere over the dry state [Rood et al., 1989]. The particle returns to its dry state when the RH drops below the crystallization point. The increase of the scattering coefficient due to particle growth is expressed as the factor $f(RH)$, which is the ratio of the scattering coefficient at a given RH to the scattering at $RH < 40$. Figure 2.5 shows the hysteresis curve of ambient air as measured by Veeffkind et al. [1996] in The Netherlands, using humidity controlled nephelometry. It is noted that hygroscopic behavior will not only affect the scattering coefficient, but will also affect the other optical properties,

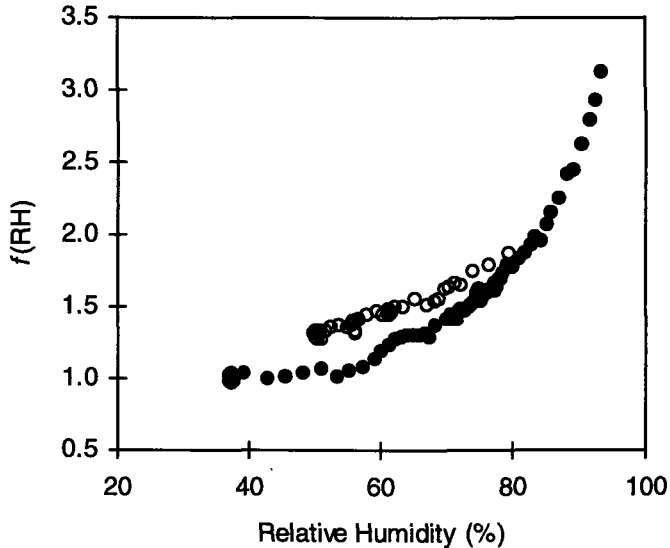


Figure 2.5: Aerosol scattering coefficient as a function of the relative humidity. Filled dots are for increasing relative humidity, open dots are for decreasing humidity (supersaturated state).

such as the phase function.

Above, only the simple case of spherical particles was considered. For spherical particles the optical properties can be calculated using Mie theory, for non-spherical particles only recently, an efficient method has been developed to calculate the optical properties. The effect of non-spherical particles on the aerosol optical properties was studied by Mishchenko [1993]. Comparisons between spheres and randomly oriented spheroids showed that especially the phase function is very sensitive to the particle shape. The ratio of the phase function for non-spherical particles to spherical particles can be as large as 3 for the scattering angles between 30 and 80° , and as small as 0.4 at scattering angles between 80 and 140° . For non-spherical particles it is important to take this effect into account when interpreting satellite measurements. However, for most of the aerosol particles the assumptions of spherical particles will be realistic, firstly because of the process by which they were formed, and secondly because of the hygroscopic nature of most aerosol particles. Secondary aerosols, such as sulfates and nitrates, are formed by gas-to-particle conversion. Gas-to-particle conversion, either on existing particles or forming new particles, will lead to spherical particles. Also the hygroscopicity, leaving the particles most of the time supersaturated, will also lead to particles which are quite spherical. On the other hand, mineral aerosols, such as desert dust are known to be strongly a-spherical. For these aerosols it is important to take particle shape into account. In the present work no cases involving desert dust are considered, and it is therefore

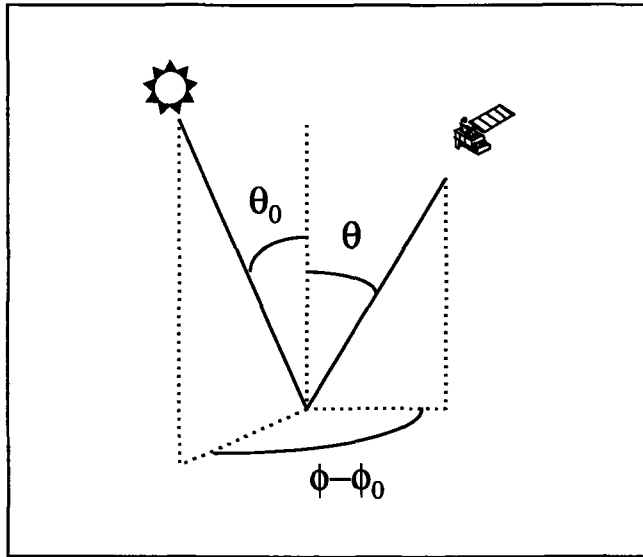


Figure 2.6: Schematic of the Sun/satellite geometry

assumed that all particles are spherical.

2.3 Principles of Aerosol Satellite Remote Sensing

Aerosol particles scatter and absorb radiation, and thus modify the radiation field in the atmosphere. Satellite sensors measure the TOA radiance, which is affected by the aerosol optical properties. Passive satellite remote sensing analyzes the TOA radiance to extract the aerosol optical properties. Clouds will have a very large impact on the TOA radiance. Aerosol retrieval is not possible when clouds are present. Therefore, only the cloud-free case will be considered. In the following, the reflectance ρ will be used instead of radiance, which is defined as $\pi L \cos(\theta_0)/F_0$ where L is the radiance, F_0 is the extraterrestrial solar irradiance and θ_0 is the solar zenith angle.

The simplest case for retrieval of aerosol optical properties is above a black surface. In this case, the TOA reflectance will be caused only by scattering in the atmosphere by aerosols and molecules (Rayleigh scattering), commonly referred to as the path reflectance. Both aerosol and Rayleigh scattering will depend on the Sun/satellite geometry, which is described by the solar zenith angle (θ_0), the satellite zenith angle (θ), and the relative azimuth angle between the Sun and the satellite ($\phi - \phi_0$), see Figure 2.6. The contribution of

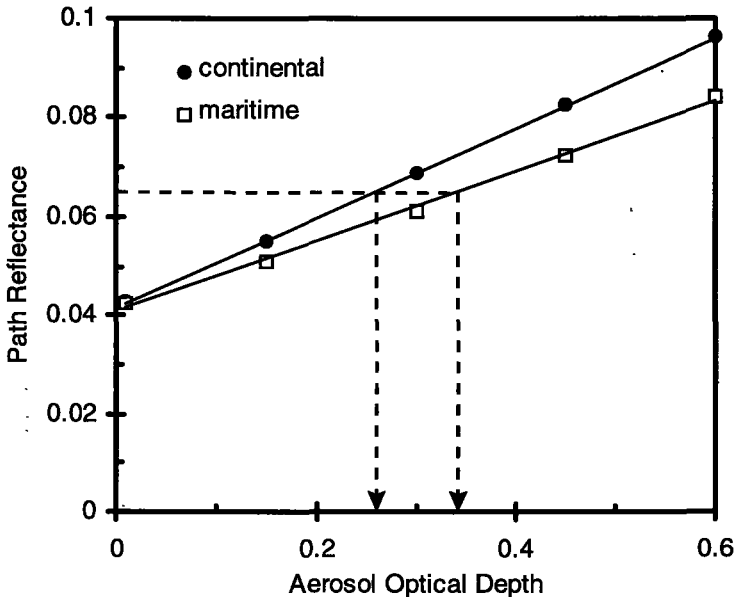


Figure 2.7: Path reflectance (ρ_{atm}) at $0.55 \mu\text{m}$ as a function of aerosol optical depth (AOD) for continental and maritime aerosol types as defined by WMO [1983] and a Sun satellite geometry defined by: $\theta_0=45^\circ$, $\theta=30^\circ$, and $\phi - \phi_0=90^\circ$. The lines are linear fits through the points, the correlation coefficients are larger than 0.99 for both fits. The dashed lines show the AOD for the continental and maritime type for the same value of the path reflectance.

aerosols to the TOA reflectance depends on the aerosol optical properties, and the vertical distribution of the aerosols. In Figure 2.7 the path reflectance is plotted as a function of the AOD, for two aerosol size distributions. This figure demonstrates the quasi-linear relationship between the path reflectance and the AOD [Durkee et al., 1986]. The slope between the reflectance and the aerosol optical depth depends strongly on the aerosol phase function, which in turn varies strongly with the aerosol size distribution. The intercept is determined by the Rayleigh scattering, and is independent of the aerosol optical properties.

The effect of the size distribution on the spectral behavior of the path reflectance due to the aerosols is illustrated in Figure 2.8. In this figure the path reflectance corrected for the Rayleigh contribution and normalized for $0.55 \mu\text{m}$, is plotted as a function of the wavelength for two aerosol types. The decrease with the wavelength is much larger for the continental aerosol type than for the maritime aerosol type. This difference is caused by the difference in size distribution between the two types: the continental aerosol type consist of smaller

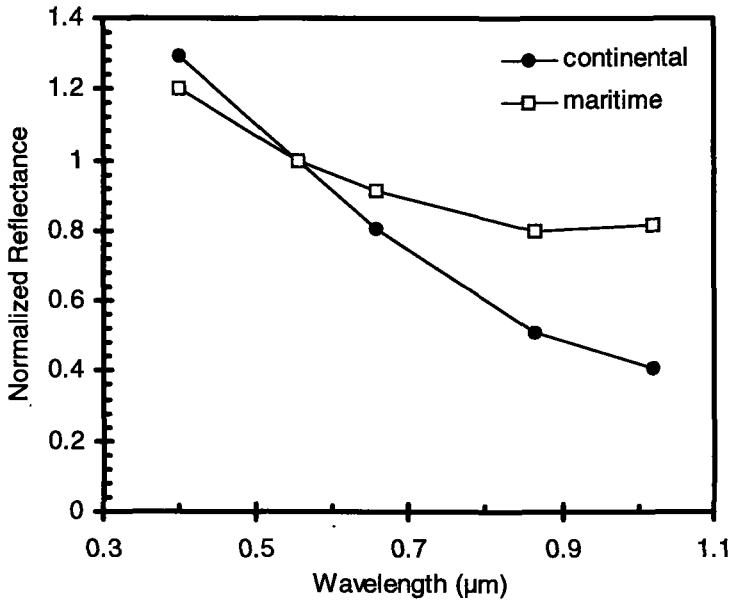


Figure 2.8: Path reflectance corrected for the Rayleigh contribution and normalized for $0.55 \mu\text{m}$, plotted as a function of wavelength. For Sun/satellite geometry and aerosol types see Figure 2.7.

particles than the maritime type. The spectral behavior of the AOD can often be represented by a power law function [Ångström, 1961]:

$$AOD(\lambda) \sim \lambda^{-\alpha}, \quad (2.9)$$

where λ is the wavelength and α is the Ångström wavelength exponent. The Ångström is related to the slope of the aerosol size distribution. When particle scattering is dominated by particles small as compared to the wavelength, α will be of the order 1.3 - 2. In the case that particle scattering is dominated by particles larger than the wavelength α tends toward zero. As can be seen in Figure 2.7, the reflectance is directly proportional to the AOD. Therefore, the spectral behavior of the AOD will also have large effects on the spectral behavior of the TOA reflectance. For relatively more smaller particles the reflectance will decrease stronger with the wavelength than when relatively more large particles are present. This can be used in retrieval algorithms to extract information on the size distribution of the aerosol particles dominating the scattering.

The first global maps of AOD were produced using the NOAA/AVHRR operational product [Husar et al., 1997]. This algorithm computes the AOD over the oceans from the $0.63 \mu\text{m}$ channel of the AVHRR. In this wavelength range

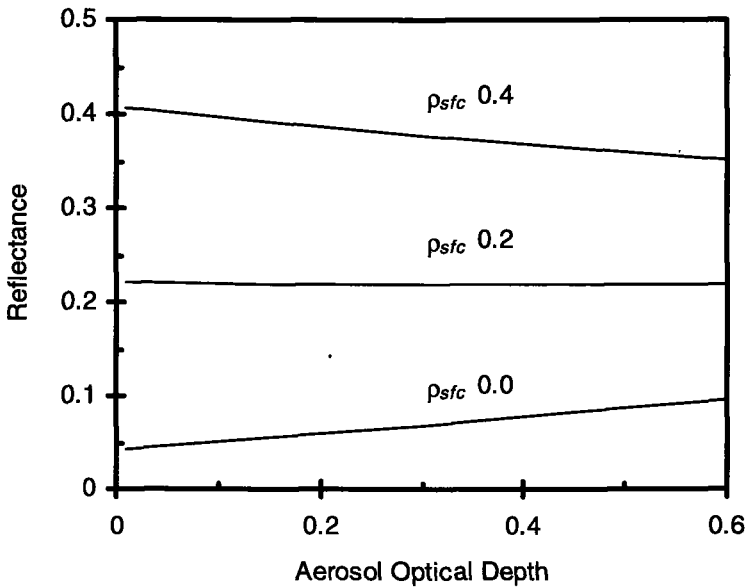


Figure 2.9: Reflectance as a function of aerosol optical depth for a surface albedo of 0.0, 0.2 and 0.4. Aerosol is of the continental aerosol type. The wavelength and Sun/satellite geometry are the same as in Figure 2.7.

the albedo of the ocean is very low. Assumptions are made on the phase function and the single scattering albedo, by prescribing the aerosol size distribution and chemical composition. In Figure 2.7 the arrows indicate the AODs for two aerosol size distributions for a given value of the path reflectance, showing that using a single size distribution will lead to considerable uncertainty in the retrieved AOD. To remove this uncertainty, Durkee et al. [1991] used both the $0.63 \mu\text{m}$ and the $0.83 \mu\text{m}$ channel of the AVHRR to extract information on the size distribution. Application of this technique is difficult because the two bands are very broad and not enough separated [Kaufman, 1995]. However, with the new generation of satellite sensors, with more and smaller spectral bands, AOD retrieval of the AOD is expected with errors $<0.03\text{-}0.05$ [Kaufman et al., 1997b]. In chapter 3 such an retrieval algorithm for use over the ocean is described in more detail.

When the surface is not black, photons reflected by the surface as well as photons scattered in the atmosphere contribute to the TOA reflectance. The reflectance of a cloud-free and horizontally homogeneous plane parallel atmosphere, overlying an isotropically reflecting (Lambertian) surface can be ex-

pressed as:

$$\rho(\lambda) = \rho_{atm}(\lambda) + \frac{\rho_{sfc}(\lambda)}{1 - \rho_{sfc}(\lambda) \cdot r(\lambda)} T(\lambda) \quad (2.10)$$

where:

ρ_{atm} is the path reflectance due to scattering in the atmosphere;

ρ_{sfc} is the surface albedo;

r is the spherical albedo of the atmosphere; and

T is the sum of the direct and diffuse transmittance by the atmosphere.

All the variables in equation (2.10) depend on the Sun/satellite geometry.

The effect of aerosols on the top of the atmosphere reflectance is twofold: first they increase the path reflectance (ρ_{atm}), and second they reduce the transmittance (T), thus decreasing the contribution of the reflection on the surface. When the surface albedo is small, the first effect will dominate, but at larger surface albedos the transmittance reduction becomes increasingly important, as shown in Figure 2.9. For a given combination of aerosol properties and surface albedo the scattering and extinction effects will cancel. For this case the reflectance will not vary with the aerosol optical depth.

Aerosol retrieval over land surfaces is much less advanced than retrieval over the ocean. In the visible and near-infrared, the land surface albedo is much higher than for sea. The impact of the higher surface albedo over land is illustrated in Figure 2.10. In this figure a scene over land and a scene over the ocean, which were taken almost simultaneously and within a few hundred kilometers, are compared. The high surface albedo over land dominates the TOA reflectance in the visible and near-infrared. One of the key problems for aerosol retrieval over land is how to distinguish between surface and atmospheric contributions to the TOA reflectance. Even when the surface albedo is known, which is usually not the case, this is difficult because of the twofold effect of aerosols on the TOA reflectance, as described above. Several methods are proposed to separate the atmospheric and the surface contributions.

Kaufman et al. [1997b] showed for different soil covers that there is a linear relation between the albedo in the mid-visible and in the mid-infrared. They propose to estimate the mid-visible albedo from the mid-infrared reflectance, for which the atmospheric contribution usually is negligible. Once the albedo is known, information on the AOD and size distributions can be derived.

The use of the degree of polarization of the radiance is thought to have great potential for aerosol retrieval over land [Herman et al., 1997b]. Because polarization of the light is caused mainly by scattering in the atmosphere, it is much easier to extract the aerosol information from the polarized radiance than from the unpolarized radiance.

The extra information from two-or multi-angle sensors can also be applied for aerosol retrieval over land. In chapter 5 an algorithm is presented based on the two angle view of the ATSR-2. This algorithm uses both the spectral and the directional information in the ATSR-2 data. An algorithm based on multi-angle radiometry is presented by Martonchik et al. [1998].

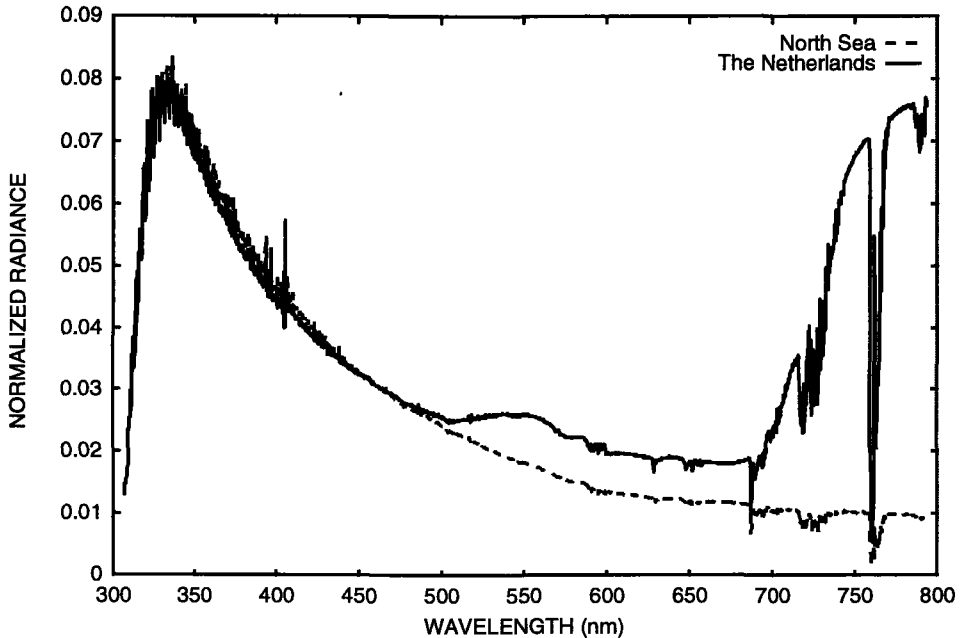


Figure 2.10: TOA radiance divided by the extraterrestrial solar irradiance, as a function of the wavelength, as measured by GOME for a scene over the Netherlands and a scene over the North Sea.

The above described methods are all based on retrieval in the visible and near-infrared. As can be seen in Figure 2.10, the TOA radiance in the UV (between 0.340 and 0.400 μm) differs little for the land and the sea pixel. In this wavelength range the albedo of most land surfaces is low (0.02 - 0.04) [Herman and Celarier, 1997]. In chapter 5 an algorithm will be presented that uses this wavelength range. The UV can also be used to sense the presence of absorbing aerosols such as desert dust and biomass burning aerosols [Herman et al., 1997a]. This retrieval technique is based on the extinction of Rayleigh scattering by aerosols. The resulting aerosol index is most sensitive to strongly absorbing aerosols at higher altitudes.

Bibliography

- Ångström, A. (1961). Techniques of determining the turbidity of the atmosphere. *Tellus*, 13:214-223.
- Durkee, P. A., Jensen, D. R., Hindman, E. E., and VonderHaar, T. H. (1986). The relationship between marine aerosols and satellite detected radiance. *J.*

- Geophys. Res.*, 91:4063–4072.
- Durkee, P. A., Pfeil, F., Frost, E., and Shema, R. (1991). Global analysis of aerosol particle characteristics. *Atmos. Environ.*, 24A:2457–2471.
- Gathman, S. G. (1983). Optical properties of the marine aerosol as predicted by the navy aerosol model. *Optical Eng.*, 22:57–62.
- Hansen, J. E. and Hovenier, J. W. (1974). Interpretation of the polarization of venus. *J. Atmos. Sci.*, 31:1137–1160.
- Herman, J. R., Bhartia, P. K., Torres, O., Hsu, C., Seftor, C., and Celarier, E. (1997a). Global distributions of uv-absorbing aerosols from nimbus 7/toms data. *J. Geophys. Res.*, 102:16,911–16,922.
- Herman, J. R. and Celarier, E. A. (1997). Earth surface reflectivity climatology at 340–380 nm from toms data. *J. Geophys. Res.*, 102:28,003–28,011.
- Herman, M., Deuzé, J. L., Devaux, C., Goluob, P., Bréon, F. M., and Tanré, D. (1997b). Remote sensing of aerosols over land surfaces including polarization measurements and application to polder measurements. *J. Geophys. Res.*, 102:17,039–17,050.
- Husar, R. B., Prospero, J. M., and Stowe, L. L. (1997). Characterization of tropospheric aerosols over the oceans with the noaa advanced very high resolution radiometer optical thickness operational product. *J. Geophys. Res.*, 102:16,889–16,909.
- IPCC (1995). Radiative forcing of climate. In Houghton, J., Filho, L. G. M., Bruce, J., Lee, H., Haites, E., Harris, N., and Maskell, K., editors, *Climate change 1994*, pages 1–231. Cambridge UP, Cambridge.
- Kaufman, Y. J. (1995). Remote sensing of direct and indirect aerosol forcing, in: Aerosol forcing of climate. In Charlson, R. J. and Heintzenberg, J., editors, *Aerosol forcing of climate*, pages 297–332. John Wiley, New York.
- Kaufman, Y. J., Tanre, D., Nakajima, T., Lenoble, J., Frouin, R., Grassl, H., Herman, B. M., King, M. D., and Teillet, P. M. (1997a). Passive remote sensing of tropospheric aerosol and atmospheric correction for the aerosol effect. *J. Geophys. Res.*, 102:16,815–16,830.
- Kaufman, Y. J., Wald, A. E., Remer, L. A., Gao, B. C., Li, R. R., and Flynn, L. (1997b). The modis 2.1 μm channel correlation with visible reflectances for use in remote sensing of aerosol. *IEEE Trans. on Geosci. and Remote Sens.*, 35:1286–1298.
- Martonchik, J. V., Diner, D. J., Kahn, R. A., Ackerman, T. P., Verstraete, M. M., Pinty, B., and Gordon, H. R. (1998). Techniques for the retrieval of aerosol properties over land and ocean using multiangle imaging. *IEEE Trans on Geosci. and Remote Sens.*, 36:1212–1227.
- Mishchenko, M. I. (1993). Light scattering by size-shape distributions of randomly oriented axially symmetric particles of size comparable to a wavelength. *Appl. Opt.*, 32:4652–4666.

- Rood, M. J., Shaw, T. V., Larson, T. V., and Covert, D. S. (1989). Ubiquitous nature of ambient metastable aerosol. *Nature*, 337:537–539.
- Schwartz, S. E. (1996). The whitehouse effect- shortwave radiative forcing of climate by anthropogenic aerosols, an overview. *J. Aerosol Sci*, 27:359–382.
- Veefkind, J. P., van der Hage, J. C. H., and ten Brink, H. M. (1996). Nephelometer derived and directly measured aerosol optical depth of the atmospheric boundary layer. *Atmos. Res.*, 41:217–228.

Chapter 3

A New Algorithm to Determine the Spectral Aerosol Optical Depth over the Ocean from Satellite Radiometer measurements

Most of this chapter has been published in the Journal of Aerosol Science: J.P. Veeffkind and G. de Leeuw, A New Algorithm to Determine the Spectral Aerosol Optical Depth from Satellite Radiometer Measurements, J. Aerosol Sci 29, 1237-1248, 1998.

A more comprehensive description of Fresnel reflection has been added to this paper.

Abstract

A new aerosol retrieval algorithm is presented which computes the spectral optical depth over the ocean from spaceborne radiometers. It includes both multiple scattering and the bi-directional reflectance of the ocean surface. The algorithm is applied to data from the Along Track Scanning Radiometer 2 (ATSR-2). This radiometer aboard the ERS-2 satellite has 4 bands in the visible and near-infrared. The ATSR-2 has a dual view capability: the reflectance is measured both at nadir and at a forward angle of approximately 55° along track. This feature is used to test the algorithm by comparing independent retrievals from the forward and the nadir view, applied to Southern Hemisphere data from 23 July, 1995. The retrieved aerosol optical depths compare favorably. The retrieved aerosol optical depths and spectral behavior are in agreement with expected

values in clean marine environments.

3.1 Introduction

Atmospheric aerosols play an important role in the Earth's radiation budget. They are considered the largest uncertainty in climate modeling, being able to -at least partly- balance global warming by anthropogenic greenhouse gases. Atmospheric aerosols influence the radiative budget in two ways, first by backscattering incoming solar radiation, and secondly by changing the albedo and lifetime of clouds. Present estimates of the radiative forcing of the combined effects are in the range between -0.4 and -3.0 Wm^{-2} on a global scale [Schwartz, 1996].

Because of the important role of aerosols for climate there is a distinct need for aerosol monitoring on a global scale. Due to the many different aerosol sources and their short lifetimes, tropospheric aerosols are highly variable in both space and time. Only satellite monitoring can achieve the global coverage and the necessary spatial resolution to measure the inhomogeneous aerosol fields [IPCC, 1995].

Satellite remote sensing of aerosol optical properties is best possible over surfaces with a low and preferably constant albedo. Most land surfaces have high surface reflectivity's, which makes satellite remote sensing extremely difficult. On the other hand, the albedo of the ocean is low and relatively well known. Therefore most studies have focused on oceanic regions.

Satellite remote sensing of aerosol optical properties requires well-calibrated, multispectral satellite sensors [Kaufman, 1995]. These sensors should have narrow spectral bands to avoid water vapor absorption regions. Most of the aerosol retrieval studies in the past have used data of the Advanced Very High Resolution Radiometer (AVHRR), which has two channels in the visible and near-infrared. The calibration of these channels is a source of uncertainty [Kaufman, 1995], and the spectral information is limited because the AVHRR bands are broad and not well enough separated. Also, the near-infrared channel suffers from severe water vapor absorption. Since recently, data from sensors more suitable for aerosol remote sensing is becoming available. These sensors have more spectral bands in the visible and near-infrared, that are narrow and thus avoid the water vapor absorption regions. Also, most of the new sensors have an in-flight calibration facility. With these new sensors it should be possible to determine the spectral aerosol optical depth over the ocean within ± 0.03 . To fully utilize their possibilities, these sensors require more advanced algorithms to compute the aerosol optical properties.

In this contribution an algorithm is presented to retrieve the spectral aerosol optical depth from satellite radiometer data over the ocean. The spectral aerosol optical depth contains information on both the aerosol size distribution as well as the concentration. The algorithm is designed to be applicable to different satellite sensors. One of the major improvements is that the bi-directional reflection of the ocean is taken into account. Past studies assumed the ocean to be black, or to be a Lambertian reflector. Simulations have shown that these assumptions may

cause serious errors in the retrieved aerosol optical depth [Tanré et al., 1997b].

The algorithm was applied to data from the Along Track Scanning Radiometer 2 (ATSR-2). ATSR-2 is a radiometer carried aboard the ERS-2 satellite, which was launched in April 1995. ATSR-2 has seven spectral bands, four of these bands are in the visible and near-infrared (effective wavelengths 0.555, 0.659, 0.865 and 1.6 μm) and are potentially useful for aerosol retrieval. The spatial resolution of the ATSR-2 is approximately $1 \times 1 \text{ km}^2$, and the swath width 500 km. A unique feature of the ATSR-2 is the dual view capability providing two views of each region: first a forward view (zenith angle approximately 55°) and about two minutes later a nadir view. The dual view is used to test the retrieval algorithm. To this end, the aerosol optical depth is retrieved independently from both the forward and the nadir view.

3.2 Algorithm Description

For cloud-free regions, the top of the atmosphere (TOA) reflectance, as measured by satellite radiometers, is due to scattering in the atmosphere by aerosols and molecules (Rayleigh scattering), and reflection by the surface. In most cases, the contribution by aerosols is not dominating the TOA reflectance. In aerosol optical depth (AOD) retrieval algorithms, the measured TOA reflectance is corrected for Rayleigh scattering and surface reflection. Also, AOD retrieval algorithms have to make assumptions on the aerosol size distribution. To correct for Rayleigh scattering, surface reflection, and to determine the best fit aerosol size distribution, radiative transfer calculations are performed. In this section we will first describe these radiative transfer calculations, and the assumptions that are used to determine the surface reflection and the aerosol size distributions. In the second part, we will describe how the AOD is computed from the measured and calculated TOA reflectances.

3.2.1 Radiative Transfer Calculations

The AOD retrieval algorithm applies only to cloud-free scenes over the ocean. For such cases, the TOA reflectance contains contributions from scattering in the atmosphere, reflection by the ocean, and combinations of atmospheric scattering and ocean reflection. To compute the TOA reflectance properly, the bi-directional reflectance of the ocean surface should be taken into account. To this end, the satellite measured reflectance is written as the sum of five components:

$$\rho = \rho_a + T_{\downarrow} \rho_{s,dir} T_{\uparrow} + t_{\downarrow} \rho_{s,dif\downarrow} T_{\uparrow} + T_{\downarrow} \rho_{s,dif\uparrow} t_{\uparrow} + t_{\downarrow} \rho_{s,iso} t_{\uparrow}, \quad (3.1)$$

where:

ρ_a is the path reflectance by aerosols and molecules;

T is the direct transmittance along an upward (\uparrow) or downward (\downarrow) path;

t is the diffuse transmittance due to forward scattering by aerosols and molecules;

and

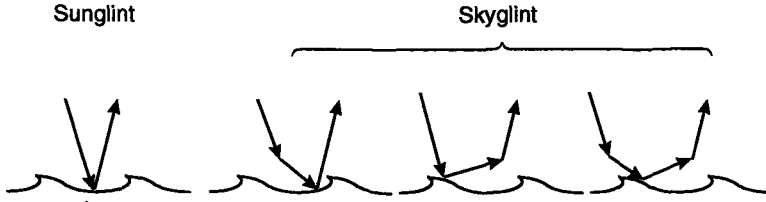


Figure 3.1: Difference between sunglint and skyglint. Sunglint is the direct contribution of light that is Fresnel reflected on the surface and transmitted on the down-and upward path through the atmosphere. Skyglint is the contribution of light that is Fresnel reflected on the surface and forward scattered on the downward, upward, or both on the down- and upward path through the atmosphere.

$\rho_{s,dir}$, $\rho_{s,dif\downarrow}$, $\rho_{s,dif\uparrow}$ and $\rho_{s,iso}$ describe the bidirectional surface reflection, see below.

All contributions in equation (3.1) depend on the wavelength and on the Sun/satellite geometry. The first component in equation (3.1), the path reflectance, is due to scattering in the atmosphere by aerosols and molecules. The path reflectance would be the only contribution if the surface were fully absorbing. The second component is the contribution of photons that are transmitted on their downward path, reflected by the ocean, and transmitted on their way up. This contribution involves only reflection by the ocean. The last three components involve both scattering in the atmosphere and reflection by the ocean. The third component accounts for photons that are scattered towards the surface on their downward path, reflected by the ocean, and transmitted to the satellite sensor. The fourth component accounts for photons that are transmitted on their downward path, reflected by the ocean, and forward scattered toward the sensor on their upward path. The last component accounts for photons that are forward scattered on their downward path, reflected by the surface, and forward scattered towards the satellite sensor on their upward path. All components of equation (3.1) are computed exactly, except for the last one. For the computation of this last term it is assumed that the scattering is isotropic. The use of an approximate value is justified because its contribution on the total TOA reflectance is small.

The algorithm uses a look-up table to compute the TOA reflectance from equation (3.1). In these look-up tables the transmittances and reflectances of equation (3.1) are stored as a function of the geometry and the wavelength. The look-up tables are computed using the discrete ordinate method DISORT [Stamnes et al., 1988]. Thus multiple scattering is taken into account. The effect of polarization is neglected.

In equation (3.1) the reflection by the ocean is described by four terms ($\rho_{s,dir}$, $\rho_{s,dif\downarrow}$, $\rho_{s,dif\uparrow}$ and $\rho_{s,iso}$). Each of these terms contains contributions by specular (Fresnel) reflection, reflectance by oceanic whitecaps, and by subsurface scattering. Fresnel reflection depends strongly on the geometry, while the re-

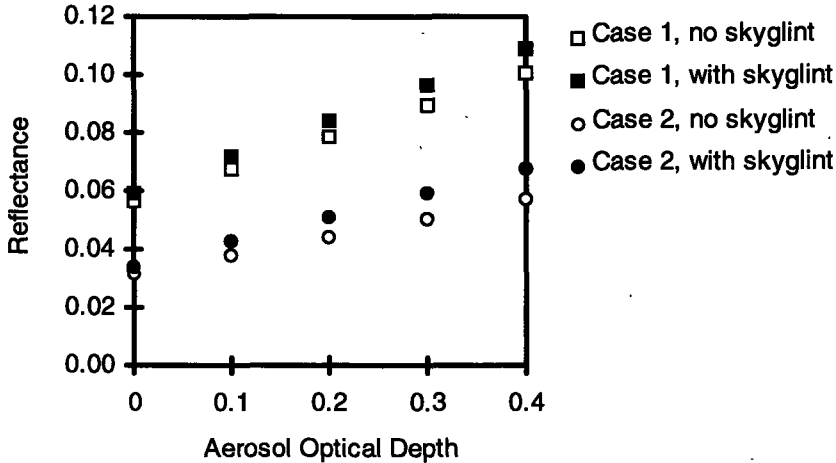


Figure 3.2: Computed top of the atmosphere reflectance at $0.55 \mu\text{m}$ with and without skylint. Case 1 is for a Sun/satellite geometry defined by $\theta_0=30^\circ$, $\theta=45^\circ$, and $\phi - \phi_0=0^\circ$; Case 2 is $\theta_0=0^\circ$, $\theta=45^\circ$, and $\phi - \phi_0=180^\circ$.

reflection by oceanic whitecaps and the subsurface reflection can in first order be approximated as isotropic [Koepke, 1984, Gordon et al., 1988]. Therefore, the four surface reflection terms in equation (3.1) differ only for the contribution of the Fresnel reflection, the other contributions are assumed Lambertian. As illustrated in Figure 3.1, Fresnel reflection contributes in two ways to the top of the atmosphere reflectance: light can reach a satellite sensor after being Fresnel reflected at the ocean surface and transmitted on its down-and upward path through the atmosphere, which is referred to as sunglint, and photons can reach the satellite sensor after being Fresnel reflected on the ocean surface and - at least once - scattered in the atmosphere. In analogy to sunglint, this is referred to as skylint.

The contribution of sunglint to the TOA reflectance is described by the Fresnel contribution to $\rho_{s,dif}$, which is computed using the formula's of Cox and Munk [1954]. The contribution of sunglint to the top of the atmosphere reflectance varies strongly with the Sun/satellite geometry. In most geometries the sunglint contribution can be neglected. By estimating the sunglint contribution, those geometries for which sunglint contributes significantly are avoided. When the sunglint contributes significantly to the TOA reflectance, the pixel is marked sunglint contaminated and is excluded from further processing. Skylint accounts for the Fresnel reflection contribution to the other surface reflection terms ($\rho_{s,dif\downarrow}$, $\rho_{s,dif\uparrow}$ and $\rho_{s,iso}$). While sunglint can be avoided by disregarding certain Sun/satellite geometry's, this does not apply to skylint. In fact, for almost all geometry's the contribution of skylint to the TOA reflectance is significant. For the calculation of the contribution of Fresnel reflection to terms $\rho_{s,dif\downarrow}$, $\rho_{s,dif\uparrow}$ and $\rho_{s,iso}$, a flat ocean surface is assumed. Simulations show that

this assumption will cause only minor errors [Takahshima and Masuda, 1985].

In Figure 3.2 the reflectance with and without skylint is plotted as a function of the aerosol optical depth. Figure 3.2 shows that the quasi-linear relationship between reflectance and aerosol optical depth is still valid when the effect of skylint is taken into account. Ignoring the skylint will introduce serious errors in the retrieved aerosol optical depth. These errors will vary with the Sun/satellite geometry, and the aerosol optical properties. A phase function that is more peaked into the forward direction, due to more larger aerosol particles, will result in more contribution by skylint. For the aerosol size distribution and geometries shown in Figure 3.2 the overestimation in the retrieval for a 'true' aerosol optical depth of 0.2 when neglecting skylint is +10% and +46% for case 1 and case 2, respectively. This clearly demonstrates that skylint should be taken into account in satellite retrieval of aerosol optical depth.

The reflectance of oceanic whitecaps depends on the area of the ocean covered by foam, and on the effective reflectance of the whitecaps [Koepke, 1984]. The area of the ocean covered with foam is related to the surface windspeed [Monahan and OMuircheartaigh, 1980]. The effective reflectance in the visible and near-infrared is almost invariable with the wavelength. An effective reflectance for the whitecaps of $22 \pm 11\%$ as reported by Koepke [1984] is used.

The contribution to the reflectance by the ocean of subsurface scattering is called the water-leaving reflectance. For open ocean conditions, the water-leaving reflectance can be modeled as a function of the chlorophyll concentration [Morel, 1988, Gordon et al., 1988]. The effect of the chlorophyll concentration on the water-leaving reflectance is illustrated in Figure 3.3 for four chlorophyll concentrations. For wavelengths $> 0.800 \mu\text{m}$ the contribution of water-leaving reflectance is neglected. In the AOD retrieval algorithm, the chlorophyll concentration can either be specified, or a value from the climatology obtained from measurements with the Color Zone Coastal Scanner (CZCS) [Feldman et al., 1994] can be used.

Retrieval of AOD from satellite radiometer measurements is not possible without application of an aerosol model. The AOD retrieval algorithm applies to open ocean and coastal regions. The aerosol in these regions is assumed to be an external mixture of anthropogenic and sea-salt aerosol. The Navy Oceanic Vertical Aerosol Model (NOVAM) [de Leeuw et al., 1989, Gathman et al., 1989] was developed to predict the aerosol concentration and size distribution from meteorological parameters, such as windspeed, temperature and relative humidity. NOVAM was developed from extensive marine aerosol studies, and has been tested in different marine environments. In NOVAM, the aerosol size distribution is the sum of four modes. The four modes represent respectively industrial dust, water solubles (sulfates and nitrates), stationary sea-salt, and freshly produced sea-salt. The size distributions of the individual modes are slightly different from the popular lognormal size distributions, and are described by:

$$\frac{dN}{dr} = \frac{A}{f} \exp\left[-\ln^2\left(\frac{r}{f \cdot r_0}\right)\right], \quad (3.2)$$

where:

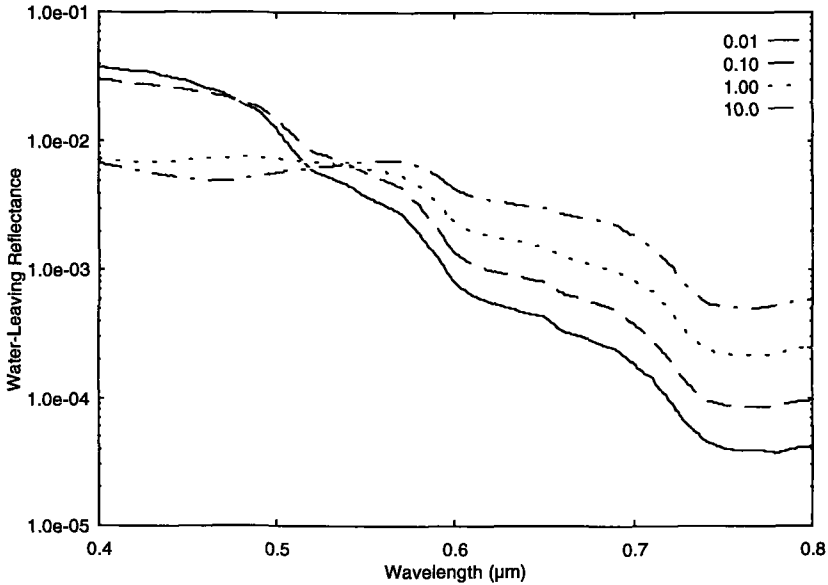


Figure 3.3: Water leaving reflectance as a function of wavelength for chlorophyll concentrations of 0.01, 0.1, 1.0 and 10.0 mg/m^3 .

N is the total number of particles per cm^3 ;

r is the radius of the particles;

r_0 is the mode radius,

A is the amplitude; and

f is the swelling factor depending on the relative humidity and defined as 1 for 80% relative humidity.

The mode radii for industrial dust and water solubles are taken as $r_0 = 0.03 \mu\text{m}$. For stationary sea-salt and freshly produced sea-salt the mode radii are $r_0 = 0.24$ and $r_0 = 1.0 \mu\text{m}$ respectively. Based on the four NOVAM modes, two aerosol types are defined. The first type is based on the first two aerosol modes. This type represents aerosols mainly produced by fossil fuel combustion and industrial activities, and will thus be referred to as the anthropogenic type. For the retrieval of column-integrated AOD, only the stationary sea-salt mode is taken into account. Contributions from the freshly produced sea-salt are neglected, based on simulations showing that usually they contribute negligibly to the column integrated AOD in the visible and near-infrared.

The optical properties of the individual aerosol contributions were computed using a Mie scattering code by De Rooij and Van der Stap [1984], with the relative humidity fixed to 80%, the rationale for this procedure is explained below.

3.2.2 Aerosol Optical Depth Retrieval

The spectral AOD is computed from the spectral TOA reflectance measured by the ATSR-2, and from the spectral TOA reflectance from the radiative transfer calculations, as described above. The AOD retrieval is based on two assumptions. The first assumption is that the TOA reflectance can be approximated as a linear function of the AOD [Durkee et al., 1986]. The second assumption is that the multiple scattering reflectance from a mixture of two aerosol types can be approximated by the weighted average of the reflectance of the individual modes [Wang and Gordon, 1994].

The first step in the AOD retrieval is to exclude sunglint and cloud contaminated pixels from further processing. In this study the SADIST-2 ATSR-2 data products [Bailey, 1995] were used. The cloud and land flags provided in this data product were used to screen for cloud and land regions. The sunglint contribution was computed using the formula's of Cox and Munk [1954], when the sunglint reflectance was $> 1 \times 10^{-3}$ the pixel was marked as sunglint contaminated.

The 0.555 and 0.659 μm channels of the ATSR-2 are affected by absorption by ozone. To correct for this absorption, all ozone is assumed to be situated in a layer at the top of the atmosphere. The ozone correction as a function of total columnar ozone amount and the Sun/satellite geometry was determined using the 6S model [Tanré et al., 1997a]. The TOA reflectance is assumed linear with the aerosol optical depth. Therefore, the TOA reflectance can be divided into contributions from an aerosol free-atmosphere, and from the TOA reflectance due to the aerosol. The latter contribution is assumed directly proportional to the AOD. From equation (3.1), the TOA reflectance for an aerosol-free (Rayleigh) atmosphere overlying the ocean surface (ρ_0) is computed. The measured TOA reflectance is corrected for ρ_0 , to obtain the TOA reflectance due to the aerosol ($\rho_{aer,meas}$):

$$\rho_{aer,meas} = \rho - \rho_0 \quad (3.3)$$

The aerosol reflectances are also computed assuming that the aerosol are only of the anthropogenic ($\rho_{aer,ant}$) or the sea-salt ($\rho_{aer,sea}$) aerosol type. Based on the assumption that the aerosol is an external mixture of the anthropogenic and the sea-salt aerosol, $\rho_{aer,meas}$ is fitted by a linear combination of the contributions from the aerosol types:

$$\rho_{aer,meas}(\lambda_i) + \varepsilon(\lambda_i) = k_1 \rho_{aer,ant}(\lambda_i) + k_2 \rho_{aer,sea}(\lambda_i) \quad (3.4)$$

where $\varepsilon(\lambda_i)$ accounts for the deviation between the measured and fitted ρ_{aer} (note that for two wavelengths $\varepsilon(\lambda_i)=0$), and k_1 and k_2 are the relative contributions of the anthropogenic and the sea-salt type, which are independent of the wavelength.

To solve this equation for k_1 and k_2 , data are needed for at least two wavelengths. The mixture of the anthropogenic and the sea-salt type that fits the spectral measurements best is determined by application of the least squares

fitting method, thus minimizing $\sum_i \varepsilon^2(\lambda_i)$. When $k_1 < 0$ the best fit aerosol model is assumed to consist of the sea-salt type only, and when $k_2 < 0$ the best fit aerosol model is assumed to consist of the anthropogenic type only. Finally, the best fit aerosol mixture is used to compute the spectral AOD, assuming a linear relation between ρ_{aer} and the AOD:

$$AOD(\lambda_i) = \frac{k_1 AOD_{ant} + k_2 AOD_{sea}}{k_1 \rho_{aer,ant}(\lambda_i) + k_2 \rho_{aer,sea}(\lambda_i)} \rho_{aer,meas}(\lambda_i) \quad (3.5)$$

where AOD_{ant} is the aerosol optical depth for the anthropogenic aerosol type, and AOD_{sea} is the aerosol optical depth for the sea-salt aerosol type.

3.3 Sensitivity Study

A study was performed to determine the sensitivity of the AOD to variations for surface windspeed, chlorophyll concentration, surface air pressure and aerosol size distribution that are used in radiative transfer calculations. To this end, a reference data set was computed, containing the TOA reflectance as a function of geometry and wavelength, for both the anthropogenic and the sea-salt aerosol type, for a surface air pressure of 1013 hPa, a chlorophyll concentration of 0.3 mg/m³, and a surface windspeed of 8 ms⁻¹. This reference data set was used as input for the AOD retrieval algorithm, as described in the previous section. To test the dependence of the retrieved AOD on the values of the input parameters, the AOD was retrieved from the reference data set with input parameters that were varied over a wide range. Two groups of error sources can be identified: the effect of variation of the air pressure, the chlorophyll concentration, or the surface windspeed is (almost) independent of the AOD, while the effect of variation in the aerosol size distribution is directly proportional to the AOD.

The effect of using a surface windspeed of 13 ms⁻¹ (instead of the “true” 8 ms⁻¹) is illustrated in Figure 3.4, where the difference between the retrieved AOD’s (wavelength 0.659 μm) is plotted as a function of the solar zenith angle. For the nadir view the difference between the “true” and the retrieved AOD varies in the range between -0.04 and -0.16, for the forward view this range is between -0.02 and -0.05. Geometries for which sunglint can be expected were avoided, therefore these errors are caused by oceanic whitecaps. Underestimating the surface windspeed in the retrieval causes smaller errors than overestimation, because the contribution of oceanic whitecaps to the TOA reflectance increases non-linearly with the windspeed. The effect of variations of the air pressure and chlorophyll concentration from their real values are small as compared to those for the windspeed. Varying the air pressure in the range between 1000 and 1025 hPa (reference is 1013 hPa) or the chlorophyll concentration from 0.003 to 3 mg/m³ (reference is 0.3 mg/m³) caused variations in the retrieved AOD at 0.659 μm of <0.02 for the nadir view and <0.01 for the forward view.

The effect of the choice of the aerosol size distribution on the retrieved AOD was tested as follows. Instead of fitting the aerosol model to the spectral input

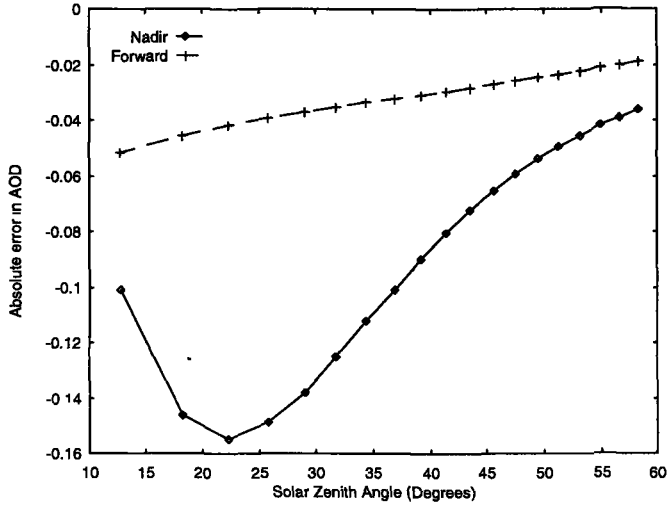


Figure 3.4: Absolute change in the retrieved AOD from the nadir and the forward view due to a 5 ms^{-1} increase of the surface windspeed with respect to the “true” data, plotted as a function of the Solar zenith angle. Results are averages over a relative Sun/satellite azimuth angle from 0 to 90° .

data (equation (3.4)), the aerosol size distribution was set to either the anthropogenic or the sea-salt type in the retrieval algorithm. The AOD was retrieved for two ‘worst case’ scenario’s: (1) using the sea-salt aerosol type to retrieve the AOD for the reference data set which was computed with the anthropogenic aerosol type, or (2) using the anthropogenic aerosol type to retrieve the AOD for the reference data set which was computed with the sea-salt aerosol type. Because the errors due to a wrong choice of the aerosol size distribution is directional proportional to the AOD, it will be presented as a relative error. The relative error in the AOD for the two worst case scenario’s are plotted as a function of the across track (West to East) distance in an ATSR-2 image in Figures 3.5 and 3.6. As expected, the relative errors for these two worst case scenario’s are large (-40 to $+60$ %). These relative errors correspond to absolute errors of -0.05 to $+0.09$ for Figure 3.5, and -0.02 to $+0.03$ for Figure 3.6. Figures 3.5 and 3.6 show that when an unrealistic aerosol size distribution is used, a large error will be introduced. Another good indication of an unrealistic aerosol size distribution is the jump in the retrieved AOD in the middle of the scan line (around a scan distance of 250 km) for the nadir view (Figure 3.5 and 3.6). This jump is caused by a sudden change of the satellite azimuth angle in the middle of the scan for the nadir view. Since such a change does not occur for the forward view, the sudden change in the AOD is absent. Figures 3.5 and 3.6 also indicate the order of magnitude of the relative errors in the retrieved AOD when a single size distribution is used instead of a variable aerosol model.

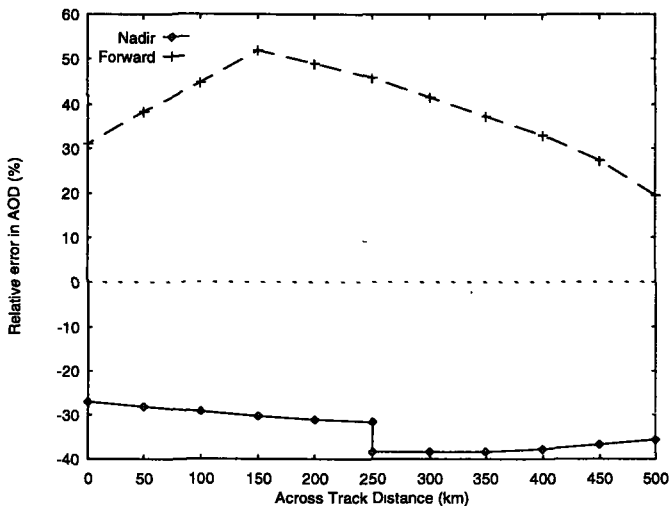


Figure 3.5: Relative change in the retrieved AOD at $0.659 \mu\text{m}$ for a single West to East line in an ATSR-2 image, caused by computing the AOD using the sea-salt aerosol type, whereas the input data was computed using the anthropogenic aerosol type (see text). The solar zenith angle was 53° .

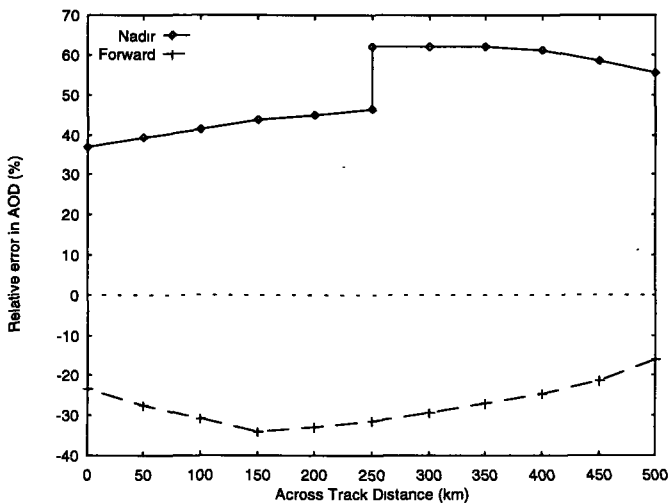


Figure 3.6: Relative change in the retrieved AOD at $0.659 \mu\text{m}$ for a single West to East line in an ATSR-2 image, caused by computing the AOD using the sea-salt aerosol type, whereas the input data was computed using the anthropogenic aerosol type (see text). The solar zenith angle was 53° .

3.4 Results and Discussion

The AOD retrieval algorithm was applied to ATSR-2 data of 23 July 1995. The dual view capability of the ATSR-2 was used to make independent retrievals for the nadir and the forward view. As explained in the previous section, comparisons between the AOD retrieved from the nadir and the forward view can be used as an internal check for the algorithm. Three relatively clear images on the southern hemisphere were selected, the locations of the center of the images are given in Table 3.1. These images are situated in the South Pacific, the South Atlantic, and in the Indian Ocean. All three are from regions without anthropogenic aerosol sources. The AOD in these regions is expected to be low (<0.1). These low AOD cases are the most difficult for AOD retrieval from satellite radiometers, because the relative error due to assumptions, on for example the surface windspeed, tend to be large.

The spatial resolution of the data is about $1 \times 1 \text{ km}^2$ at nadir. For the nadir images part of the data from the $0.555 \mu\text{m}$ channel is missing. For the forward view most of the $0.555 \mu\text{m}$ and most of the $1.6 \mu\text{m}$ data is missing. Also, the forward view data is interlaced, meaning that only 50 % of the pixels is obtained, forming a ‘checkerboard’ pixel pattern. The data rate for the images is 8 bit for each of the channels.

The AOD retrieval algorithm was applied to retrieve the AOD for the nadir and the forward views independently. The cloud and land flags provided in the ATSR-2 data were used to identify cloud-free pixels over the ocean. Daily averaged meteorological data was obtained from the NCEP/NCAR database [Kalnay and Co-authors, 1996]. The surface air pressure and surface windspeed were similar: (for all the three images) surface air pressure around 1021 hPa and surface windspeed in the range 7 to 8 ms^{-1} . The total column ozone amount was obtained from the Global Ozone Monitoring Experiment (GOME) [Stammes, personal communication], which is on the same satellite as the ATSR-2.

Figure 3.7 shows the retrieved AOD at $0.659 \mu\text{m}$ for the nadir and the forward view, for the South Atlantic image. Figure 3.7 shows that retrieved AOD compares best in large cloud-free regions. In between clouds and at their edges, the retrieved AOD for the nadir view is higher than the forward view retrieval. This is caused by a combination of two effects: firstly, the slant path of the forward view causes the pixels to be larger for the forward than for the nadir

Image	Location	AOD nadir	AOD forward
South Atlantic	26.86° S 30.52° W	0.06±0.03	0.07±0.02
South Pacific	29.19° S 80.43° W	0.08±0.03	0.07±0.02
Indian Ocean	31.72° S 43.63° E	0.10±0.06	0.09±0.04

Table 3.1: Location, mean and standard deviation for aerosol optical depth at $0.659 \mu\text{m}$ for the nadir and forward retrievals. Data are for the ATSR-2 overpass on 23 July, 1995.

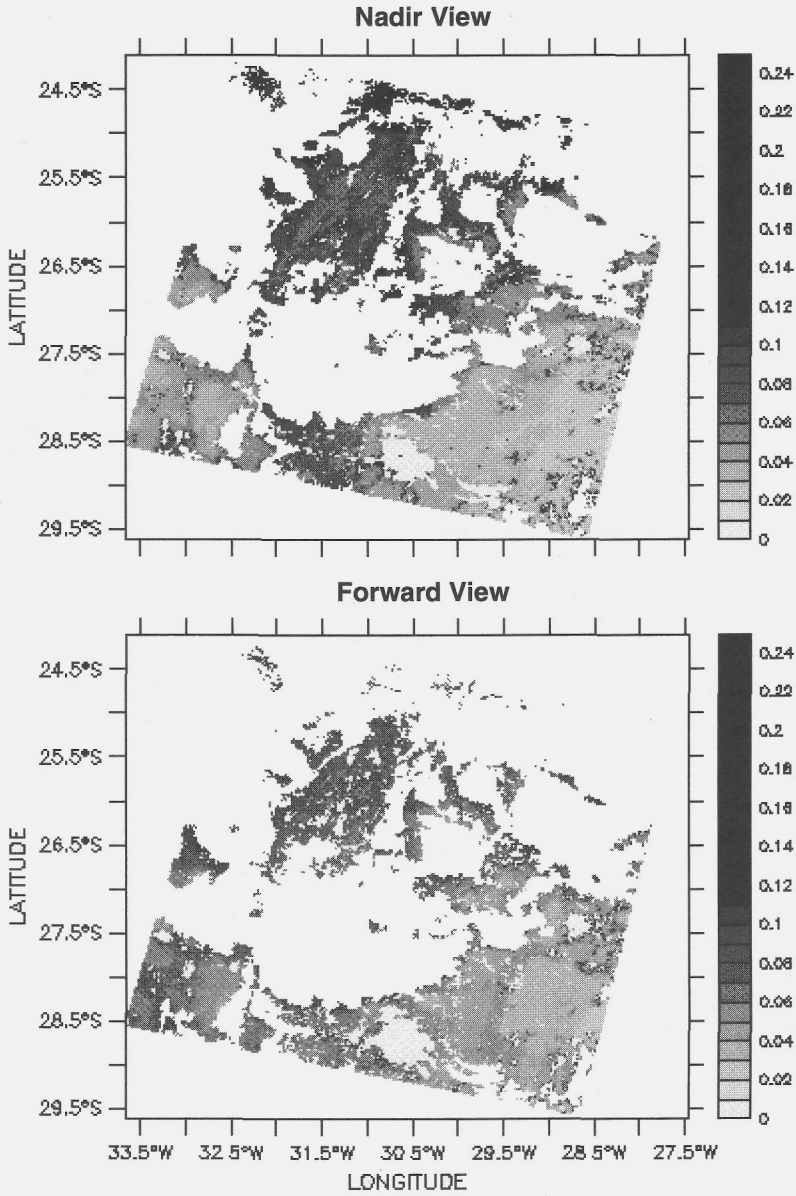


Figure 3.7: AOD at $0.659 \mu\text{m}$ over the South Atlantic Ocean retrieved from the nadir view (upper panel), and the forward view (lower panel) of the ATSR-2 overpass on 23 July, 1995.

view. Therefore, sudden changes in the TOA reflectance are averaged of a larger area, causing a more blurred image. Secondly, the atmospheric properties change rapidly near clouds. The combined nadir and forward view measurement covers a horizontal distance in the lower troposphere of about 10 km. Changes in the atmosphere on scales smaller than 10 km will therefore result in differences in the retrieved AOD for the nadir and forward view. Because the nadir viewing direction makes it possible to measure closer to the edges of the clouds, the AOD is expected to be higher because of the high relative humidities in these regions which in turn affect the aerosol size distribution.

In Figure 3.8 the AOD for both the nadir and the forward view AOD are plotted as a function of the longitude for the Indian Ocean image. The spikes in the retrieved AOD for the nadir view are caused by cloud edges, apparently the cloud mask didn't work properly for these few cases. The comparison between nadir and forward AOD is very good, except for the longitudes larger than 46.3° E. This area could be identified as an area with increased cloudiness, causing larger values for the nadir AOD, as described above. For all three images, the nadir and forward AOD for large cloud-free regions are within ± 0.02 of each other. Systematic differences between nadir and forward view AOD, as would be caused by using an unrealistic aerosol size distribution (see Figures 3.5 and 3.6), are not present. Also, sudden changes in the retrieved nadir AOD in the middle of the image did not occur.

The averages and standard deviations for the AOD retrieved from the forward and nadir images are presented in Table 3.1. These values are based on only those pixels for which both a nadir and forward AOD were available. The mean AOD for the nadir and the forward views compare favorably. In two out of three cases the mean AOD for the nadir view is somewhat larger, due to cloud edge effects described above. Also, the standard deviations are larger for the nadir view. The sensitivity study showed that the nadir view retrieval is more sensitive to assumptions for the windspeed, air pressure and chlorophyll concentration. However the larger standard deviation can also be explained by the effect of the 8 bit digitization of the ATSR-2 data. Figure 3.9 shows the retrieved AOD for the nadir view as a function of the latitude for a single scan line. Between 29.0 and 28.0° S the AOD decreases stepwise, which is caused by the digitization step in the data. In AOD units, the digitization step is about 0.03 for the nadir view retrieval. For the forward view, this is about 0.01.

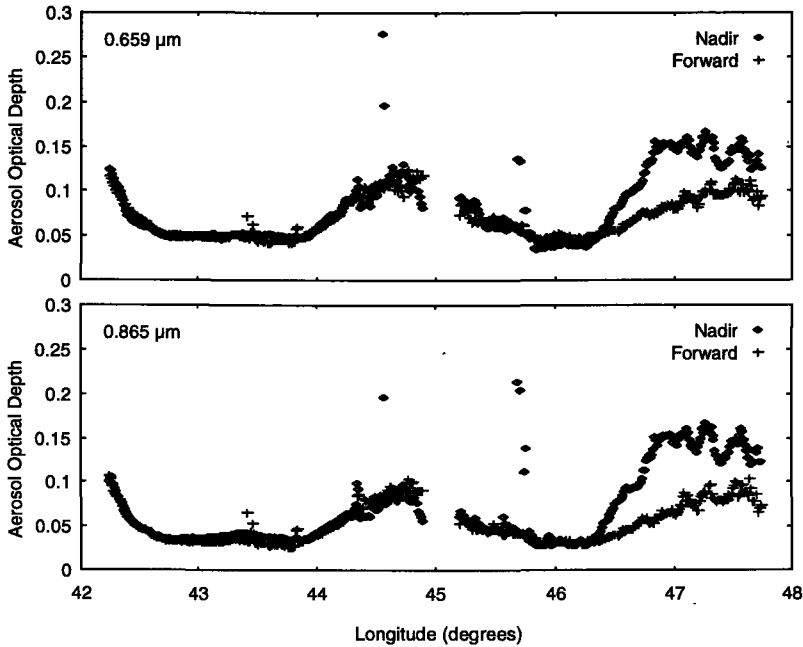


Figure 3.8: AOD retrieved from the nadir and the forward view of the ATSR-2, plotted as a function of the longitude for the region 26.8S to 29S, for 23 July 1995. Upper panel is for $0.659 \mu\text{m}$, and the lower panel is for $0.865 \mu\text{m}$.

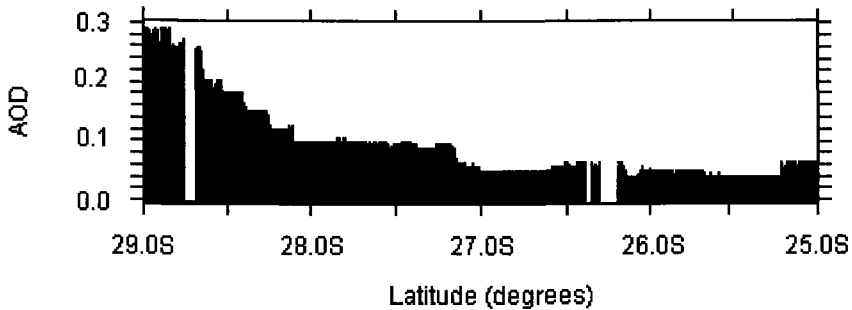


Figure 3.9: AOD retrieved from the nadir view of the ATSR-2 for 23 July 1995, plotted as a function of the latitude.

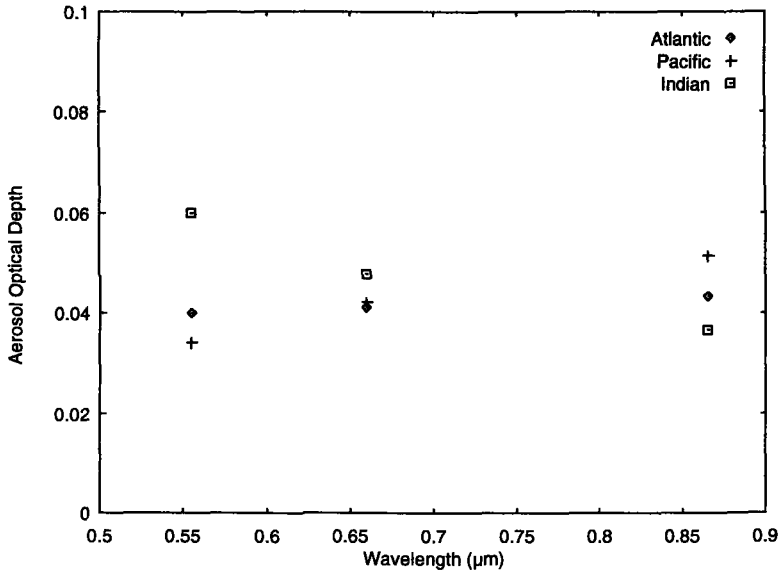


Figure 3.10: AOD retrieved from the nadir view of the ATSR-2, for 23 July 1995, plotted as a function of the wavelength, for large cloud-free regions in the South Atlantic, South Pacific, and Indian Ocean images (see Table 3.1).

The spectral AOD for large cloud-free regions in each of the images of Table 3.1 are plotted as a function of wavelength in Figure 3.10. Figure 3.10 was made using the nadir view, for which data was present for the 0.555, 0.659 and 0.865 μm channels, whereas for the forward view the data for the 0.555 μm data was missing. The AOD at 0.659 μm for these large cloud-free regions is <0.06 , in good agreement with expected values for these clean marine environments [IPCC, 1995].

The spectral behavior of the AOD contains information on the aerosol size distribution. A steep decrease of the AOD with the wavelength indicates that the AOD is dominated by particles with a diameter smaller than the wavelength. When there is little decrease or even an increase, this indicates that the AOD is dominated by particles larger than the wavelength. The latter is observed for the South Atlantic and South Pacific cases shown in Figure 3.10. For the Indian Ocean case, the AOD decreases with the wavelength, but the decrease is such that aerosol size distribution is dominated by the larger (sea-salt) particles, as expected in these clean marine environments.

3.5 Conclusions

A new aerosol retrieval algorithm was applied to ATSR-2 data. The algorithm was tested by comparing independent aerosol optical depth retrievals from the

forward and the nadir view. This method is applied to data from the Southern hemisphere from 23 July 1995. There is good agreement between the aerosol optical depths from the forward and the nadir view for larger cloud-free regions. In between clouds and at their edges the aerosol optical depth retrieved from the nadir view is higher than for the forward view. This is caused by a combination of the larger pixel size for the forward view, and the horizontal inhomogeneity of the atmosphere near the clouds. The 8 bit digitization of the data causes digitization steps in aerosol optical depth units of approximately 0.01 for the forward view and 0.03 in the nadir view. The retrieved aerosol optical depths and the spectral behavior are in agreement with expected literature values for clean marine environments. Together these results give confidence in the retrieval algorithm. An assessment of the sensitivity of the algorithm to the input parameters was presented. In the near future the algorithm will be tested against ground based sunphotometer measurements.

Acknowledgments

The work described in this paper is supported by the Netherlands Space Research Organization (SRON), contract EO-008. The ATSR-2 data were kindly provided by the European Space Agency (ESA-ESRIN). The authors thank Robert Koelemeijer of the Royal Netherlands Meteorological Institute (KNMI) for his help with the ATSR-2 data. The radiative transfer calculations on Fresnel reflection were performed by Daphne Stam of the Free University of Amsterdam. The Free University of Amsterdam, department of physics and astronomy, is thanked for making available their Mie-scattering code "Meerhoff Mie Program". The Ferret analysis package, developed by NOAA-PMEL, was used in the preparation of this work (available at <http://ferret.wrc.noaa.gov>).

Bibliography

- Bailey, P. (1995). Sadist-2 v100 products. Technical Report RAL Report ER-TN-RAL-AT-2164, RAL, Didcot, UK.
- Cox, C. and Munk, W. (1954). Statistics of the sea surface derived from sun glitter. *J. Mar. Res.*, 13:198–227.
- de Leeuw, G., Davidson, K. L., Gathman, S. G., and Noonkester, R. V. (1989). Modeling of aerosols in the marine mixed-layer. In *SPIE Proceedings 1115, Propagation Engineering*, pages 287–294.
- De Rooij, W. A. and Van der Stap, C. C. A. H. (1984). Expansion of mie scattering in generalized spherical functions. *Astron. Astrophys.*, 131:237–248.
- Durkee, P. A., Jensen, D. R., Hindman, E. E., and VonderHaar, T. H. (1986). The relationship between marine aerosols and satellite detected radiance. *J. Geophys. Res.*, 91:4063–4072.

- Feldman, G., McClain, C., and Esaias, W. (1994). Czcs dataset guide document. Technical report, NASA. available at <http://eosdata.gsfc.nasa.gov>.
- Gathman, S. G., de Leeuw, G., Davidson, K. L., and D., J. (1989). The naval oceanic vertical aerosol model: Progress report. In *AGARD 45th symposium of the Electromagnetic Wave Propagation Panel on Atmospheric propagation in the UV, visible, IR and mm-wave region and related systems aspects*, Copenhagen, Denmark.
- Gordon, H. R., Brown, O. B., Evans, R. H., Brown, J. W., Smith, R. C., Baker, K. S., and Clark, D. K. (1988). A semianalytic radiance model of ocean color. *J. Geophys. Res.*, 93:10,909–10,924.
- IPCC (1995). Radiative forcing of climate. In Houghton, J., Filho, L. G. M., Bruce, J., Lee, H., Haites, E., Harris, N., and Maskell, K., editors, *Climate change 1994*, pages 1–231. Cambridge UP, Cambridge.
- Kalnay, E. and Co-authors (1996). The ncep/ncar 40-year reanalysis project. . *Bull. Amer. Meteor. Soc.*, 77:437–471.
- Kaufman, Y. J. (1995). Remote sensing of direct and indirect aerosol forcing, in: Aerosol forcing of climate. In Charlson, R. J. and Heintzenberg, J., editors, *Aerosol forcing of climate*, pages 297–332. John Wiley, New York.
- Koepke, P. (1984). Effective reflectance of oceanic whitecaps. *Appl. Opt.*, 23:1816–1824.
- Monahan, E. C. and OMuircheartaigh, I. (1980). Optimal power-law description of oceanic whitecap dependence on wind speed. *J. Phys. Ocean*, 10:10, 2094.
- Morel, A. (1988). Optical modeling of the upper ocean in relation to its biogenous matter content (case i waters). *J. Geophys. Res.*, 93:10,749–10,768.
- Schwartz, S. E. (1996). The whitehouse effect- shortwave radiative forcing of climate by anthropogenic aerosols, an overview. *J. Aerosol Sci*, 27:359–382.
- Stamnes, K., Tsay, S., Wiscombe, W., and Jayaweera, K. (1988). Numerically stable algorithm for discrete-ordinate-method radiative transfer in multiple scattering and emitting layered media. *Appl. Opt.*, 27:2502–2509.
- Takhashima, K. and Masuda, K. (1985). Degree of radiance and polarization of the upwelling radiation from an atmosphere-ocean system. *Appl. Opt.*, 24:2423–2429.
- Tanré, Deuzé, J. L. H. M., and Morcette, J. J. (1997a). Second simulation of the satellite signal in the solar spectrum, 6s: an overview. *IEEE trans. on Geosci. and Rem. Sensing*, 35:675–686.
- Tanré, Kaufman, Y. J. H., M., M., and S, S. (1997b). Remote sensing of aerosol properites over oceans using the modis/eos spectral radiances. *J. Geophys. Res.*, 102:16971–16988.
- Wang, M. and Gordon, H. R. (1994). Radiance reflected from the ocean-atmosphere system: synthesis from individual components of the aerosol size distribution. *Appl. Opt.*, 33:7088–7095.

Chapter 4

Aerosol Optical Depth retrieval using ATSR-2 and AVHRR during TARFOX

This chapter has been published in the Journal of Geophysical Research : J.P. Veeffkind, G. de Leeuw, P.A. Durkee, P.B. Russell, P.V. Hobbs, and John M. Livingston, Aerosol Optical Depth Retrieval using ATSR-2 and AVHRR data during TARFOX, J. of Geophys. Res., vol. 104, D2, 2253-2260, 1999.

Abstract

Satellite retrieved aerosol optical properties are compared to aircraft measurements for a case study during the Tropospheric Aerosol Radiative Forcing Observational Experiment (TARFOX). Two satellite instruments are used: the Along Track Scanning Radiometer 2 (ATSR-2) and the Advanced Very High Resolution Radiometer (AVHRR). The aerosol optical depth in the mid-visible ($0.555 \mu\text{m}$) retrieved from the ATSR-2 data agrees within 0.03 with colocated sunphotometer measurements. Also, the spectral behavior of the aerosol optical depth is retrieved accurately. Good correlation is found between aerosol optical depths for AVHRR channel 1 ($0.64 \mu\text{m}$) and sunphotometer derived values, but the satellite retrieved values are 0.05 to 0.15 lower. The Ångström wavelength exponent is determined both from the ATSR-2 and the AVHRR data. The ATSR-2 derived Ångström exponents are in good agreement with the values computed from the sunphotometer data. The Ångström exponents determined from AVHRR data show very large variations. Both the ATSR-2 and the AVHRR aerosol optical depth images show a large gradient. Vertical profile data of temperature, relative humidity, and particle scattering indicate that this gradient is probably caused by changes in the dry aerosol properties, rather than a change in the relative humidity.

4.1 Introduction

Atmospheric aerosol particles influence the Earth's radiation balance in two ways: by scattering and absorption of the incoming solar radiation (direct effect), and by changing the albedo and lifetimes of clouds (indirect effect). The radiative forcing caused by anthropogenic aerosol particles due to the combined effects is estimated to be in a wide range between -0.4 and -3.0 W/m^2 on a global scale [Schwartz, 1996]. These estimates are of the same order of magnitude, but of opposite sign, as the radiative forcing by anthropogenic greenhouse gases. The impact of aerosol particles is considered the largest uncertainty in climate modeling. One of the main reasons for this large uncertainty is the lack of data on a global scale. Satellite monitoring can achieve the global coverage and the necessary spatial resolution to measure the inhomogeneous aerosol fields, necessary as input for climate models. The retrieval of aerosol properties from satellite data requires well-calibrated multispectral sensors [Kaufman, 1995]. These sensors should have narrow spectral bands outside the water vapor absorption regions. Most aerosol retrieval studies in the past have used the visible and near-infrared channels of the advanced very high resolution radiometer (AVHRR) [e.g., Durkee et al., 1991; Husar et al., 1997]. The calibration of these channels is a source of uncertainty [Kaufman, 1995], and the spectral information is limited because the AVHRR bands are broad and not sufficiently separated. Also, the near-infrared channel 2 suffers from severe absorption by water vapor.

The Along Track Scanning Radiometer 2 (ATSR-2) is the first of a series of satellite sensors that are more suitable for aerosol retrieval. These improved sensors require more advanced aerosol retrieval algorithms to fully utilize their potential. For validation of these algorithms, so-called "column" closure experiments are very useful. This was one of the major goals of the Tropospheric Aerosol Radiative Forcing Observational Experiment (TARFOX) [Russell et al., 1999a]. TARFOX was an intensive field program dedicated to measure the direct radiative forcing by tropospheric aerosol particles. TARFOX was conducted offshore from the eastern United States in July 1996, one of the most polluted regions on the globe.

In this contribution a comparison is presented between the results from an aerosol retrieval algorithm developed at the Netherlands Organization for Applied Scientific Research- Physics and Electronics Laboratory (TNO-FEL) (see chapter 3) and TARFOX data. This algorithm retrieves the spectral aerosol optical depth (AOD) over the ocean. It includes both multiple scattering and the bidirectional reflectance of the ocean surface. The algorithm was designed to be applicable to different sensors. In this chapter it is applied to ATSR-2 and AVHRR data.

The ATSR-2 is a radiometer aboard the European ERS-2 satellite, which was launched in April 1995. ATSR-2 has seven spectral bands, four of these bands are potentially useful for aerosol retrieval. The effective wavelengths of these four channels are 0.555 , 0.659 , 0.865 , and 1.6 μm . In-flight calibration is performed by measuring the Sun's irradiance during some parts of the orbit. The spatial resolution is approximately 1×1 km^2 at nadir. The swath width is

500 km. The ATSR-2 has a dual view: the reflectance is measured at nadir and at approximately 55° along track. Independent retrievals from the nadir and the forward image compare favorably, see chapter 3.

The AVHRR has two shortwave channels: one visible and one near-infrared. The effective wavelengths of the visible and near-infrared channels of the AVHRR aboard the NOAA-14 are 0.64 and 0.84 μm . The spatial resolution is 1.1 km^2 at nadir, and the swath width is approximately 2000 km. A detailed description of the AVHRR is given by Kidwell [1997].

The ATSR-2 is more suitable for aerosol retrieval than the AVHRR because it has more channels that cover a wider wavelength region. Also, the in-flight calibration is an advantage. The drawback of the ATSR-2 is the smaller swath width. The swath of the AVHRR is more than four times larger, providing better global coverage. Also, the AVHRR has a long historical database dating back to the late seventies.

The AOD retrieved from ATSR-2 and AVHRR data will be compared to the AOD measured with a sunphotometer mounted on an aircraft. When the aircraft is flying at low altitude, this is one of the most direct ways to validate aerosol satellite retrieval algorithms. Also, aircraft profile data are used together with satellite data to improve the interpretation of AOD images.

4.2 Retrieval Algorithm

A detailed description of the aerosol retrieval algorithm applied to ATSR-2 data is given in chapter 3. The algorithm was designed to be applicable to different sensors. Here it will be applied to ATSR-2 and AVHRR data. Specific details for these two sensors are discussed in some detail.

The algorithm applies only to cloud-free scenes over the open ocean. In the visible and near-infrared the reflectance of the ocean outside sunglint areas is low. For weakly absorbing aerosols, the upwelling radiance at the top of the atmosphere (TOA) over such dark surfaces increases with increasing AOD. In fact, there is a near-linear relationship between the TOA radiance and the AOD [Durkee et al., 1986]. In the following, reflectance will be used instead of radiance. The reflectance (ρ) is defined as $\pi L/F_0 \cos \theta_0$, where L is the radiance, F_0 is the extraterrestrial solar irradiance, and θ_0 is the solar zenith angle. The TOA reflectance contains contributions from scattering in the atmosphere, reflection at the surface, and combinations of atmospheric scattering and surface reflection. To compute the TOA reflectance properly, multiple scattering and the bidirectional reflectances of the ocean should be taken into account. To this end, the satellite measured reflectance is written as the sum of five components [Tanré et al., 1979]:

$$\rho = \rho_a + T_{\downarrow} \rho_{s,dir} T_{\uparrow} + t_{\downarrow} \rho_{s,dif\downarrow} T_{\uparrow} + T_{\downarrow} \rho_{s,dif\uparrow} t_{\uparrow} + t_{\downarrow} \rho_{s,iso} t_{\uparrow} \quad (4.1)$$

where ρ_a is the path reflectance by aerosols and molecules, T is the direct transmittance along an upward (\uparrow) or downward (\downarrow) path, t is the diffuse transmittance due to forward scattering by aerosols and molecules, and $\rho_{s,dir}$, $\rho_{s,dif\downarrow}$,

$\rho_{s,dift}$ and $\rho_{s,iso}$ describe the bidirectional surface reflection. All contributions in equation (1) depend on the wavelength and on the Sun/satellite geometry.

The first component in equation (1), the path reflectance, is due to atmospheric scattering by aerosols and molecules. The second component is the contribution of light that is reflected at the surface and transmitted along the downward and upward path through the atmosphere. The last three terms are due to combinations of scattering in the atmosphere and reflection at the surface. For the specular (Fresnel) reflecting ocean surface the contribution of these combinations is significant in almost all geometries. Simulations show that ignoring these terms will lead to serious errors in the retrieved AOD.

The ocean albedo is assumed to be the sum of subsurface reflection, reflection on oceanic whitecaps, and specular reflection. For the open ocean the subsurface reflection is a function of the chlorophyll concentration [Morel, 1988]. The reflection by oceanic whitecaps is taken to be a function of the surface wind speed [Koepke, 1984]. The direct contribution of specular reflection to the TOA reflectance is computed using the Cox and Munk [1954] sunglint formulas. A flat ocean surface is assumed for the computation of the diffuse contribution of specular reflection. Simulations show that this will cause only minor errors [Takhshima and Masuda, 1985].

Reflectances and transmissions for Rayleigh atmospheres and atmospheres containing both gases and aerosols were calculated as a function of wavelength and geometry and stored in look-up tables. These tables were computed using the DISORT multiple scattering code [Stamnes et al., 1988]. The major advantage of using look-up tables in combination with equation (1) is the computational speed, whereas bidirectional reflectance and multiple scattering are accounted for as well.

The first step in the retrieval of the spectral AOD is the correction for absorption by ozone. Next the TOA reflectance for a Rayleigh atmosphere overlying an ocean surface is subtracted from the measured reflectance. For the AVHRR this is followed by a water vapor absorption correction. The water vapor is assumed to be well mixed with the aerosol [Tanré et al., 1992]. The total column water vapor amount is computed using the split-window technique of Dalu [1986]. The reflectance left after subtraction of the contribution from a Rayleigh atmosphere overlying an ocean surface is due to the aerosol. The aerosol is assumed to be an external mixture of an anthropogenic and a sea-salt aerosol type. These two types are based on the Navy Oceanic Vertical Aerosol Model (NOVAM) [Gathman and Davidson, 1993]. The two aerosol types are mixed such that the spectral behavior of the reflectance due to the aerosol best fits the measurements. This assumes that the multiple scattering from a mixture of two aerosol types can be approximated by the weighted average of the reflectance of the two individual modes [Wang and Gordon, 1994]. The spectral AOD is computed for this mixture, assuming a linear relationship between the TOA reflectance and the AOD.

4.3 Experiments

During the TARFOX field campaign, measurements were performed from many different platforms. These included satellite observations from different polar and geostationary satellites, measurements from four aircraft platforms, ground-based observations from a number of different stations, and measurements from two research vessels. Satellite data from two sensors (ATSR-2 and AVHRR) will be compared with measurements from the University of Washington (UW) Convair C-131A aircraft [Hobbs, 1999]. Below a description is given of some of the measurements that were performed aboard the UW C-131A during TARFOX.

Aboard the UW C-131A was the six-wavelength NASA Ames Airborne Tracking Sunphotometer (AATS-6) [Matsumoto et al., 1987]. AATS-6 was used to derive the AOD of the column above the aircraft in four bands with center wavelengths 0.380, 0.451, 0.525, and 1.021 μm , with widths 0.005 μm . AOD values and uncertainties were derived as described by Russell et al. [1993, 1999]. Light scattering by aerosol particles was measured with two integrating nephelometers: an MRI model 1567 measuring at 0.540 μm , and an MS Electron three-wavelength nephelometer measuring at 0.450, 0.550, and 0.700 μm . Both instruments were measuring at low relative humidity. The aerosol size distribution, in the size range between 0.1 and 3.0 μm diameter, was measured using a Particle Measuring Systems (PMS) optical counter type PCASP, which was calibrated using latex spheres. During satellite overpasses the UW C-131A flew at low altitude (~ 30 m above the sea surface), thus being able to measure the AOD of (almost) the total column. Also profiles were flown to obtain information on the vertical structure of the atmosphere and the aerosol properties as a function of height.

4.4 Results and Discussion

During the TARFOX field campaign from July 10 to July 31, 1996, the ATSR-2 passed seven times over the area. Unfortunately, the majority of these overpasses were cloud contaminated. On other days there were no low-level flights during the ERS-2 overpass. However, on July 25, a day with very few clouds, both data from an ERS-2 overpass and from the sunphotometer are available. Results from this day are presented below. First, a brief overview of the synoptic conditions will be given. To validate the ATSR-2 aerosol retrieval algorithm, results will be compared with sunphotometer data. Also AVHRR retrieved AOD will be compared with sunphotometer data. Finally, profile data from the UW C-131A will be used to investigate the observed AOD pattern.

4.4.1 Synoptic Situation

Prefrontal conditions existed over the TARFOX area on July 25, 1996, with southeasterly flow at 3-5 ms^{-1} due to a 1015 hPa low-pressure center forming inland over the North Carolina/Virginia border. Figure 4.1a shows the ATSR-2

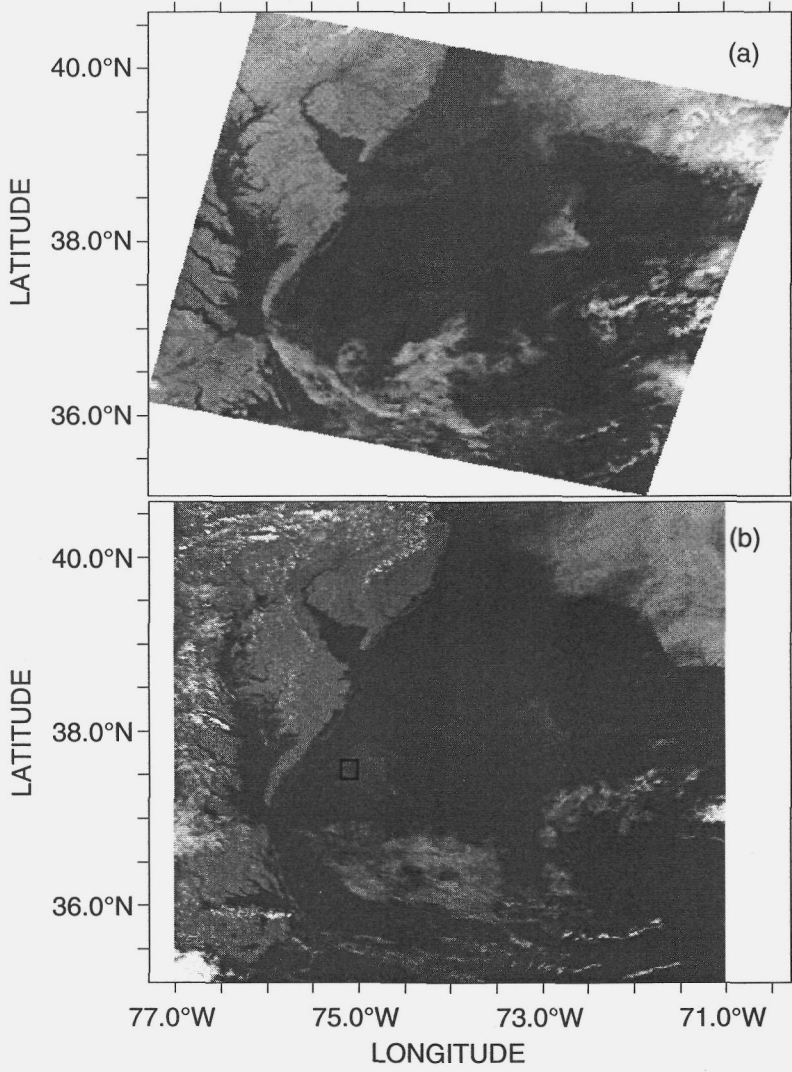
near-infrared ($0.865 \mu\text{m}$) image of the TARFOX area. A broad area of low clouds associated with an easterly moving low-pressure center is present in the northern part of the area. Some cumuloform cloudiness associated with the dissipating trailing cold front exists in the southern region of the image. Otherwise, the area is generally clear.

4.4.2 ATSR-2 Retrieval

On July 25, 1996, the ERS-2 passed the TARFOX experimental area at 1552 UTC. The aerosol retrieval algorithm was applied to retrieve the spectral AOD from the ATSR-2 data. To identify clear pixels over the ocean, the cloud and land flags provided in the ATSR-2 data product were used. Pixels for which the sunglint reflectance exceeded 1×10^{-2} were marked as sunglint contaminated and excluded from further processing. As mentioned above, the ATSR-2 has a dual view capability, providing two images for different viewing angles (forward and nadir) of the same region. The nadir image for July 25, 1996 is contaminated by sunglint. Therefore, only the forward view will be considered. The image for the AOD at $0.659 \mu\text{m}$ is presented in Figure 4.1c. The AOD image shows strong aerosol gradients in the TARFOX area. A region with lower optical depth values (~ 0.15 at $0.659 \mu\text{m}$) is centered around 38°N , 74°W . North of this region, the AOD increases by a factor of 2-3 over a distance of a few hundred kilometers. To the south and east of the region with lower optical depth, the AOD increases by a factor of 1.5-2. However, there are more clouds present in these regions which makes the interpretation more difficult.

Simultaneous with the ERS-2 overpass, the UW C-131A performed a flight track at low altitude (altitude $\sim 30 \text{ m}$) (a so-called satellite underflight). The ERS-2 underflight was performed between 1544 and 1554 UTC. The position of the aircraft was between 37.4 and 37.6°N , and 75.2 and 75.0°W (see Plate 1b). The sunphotometer aboard the UW C-131A measured the AOD of the total column (minus the lowest 30 m). In Figure 4.2 the mean spectral AOD over the low-altitude track is compared with the AOD retrieved from the ATSR-2 data, averaged over the underflight area. The ATSR-2 data and the sunphotometer data are not available at the same wavelengths. However, it is reasonable to assume a smooth variation of the AOD with the wavelength, and thus the data points of both methods can be interpolated. Application of this procedure shows that the ATSR-2 and sunphotometer AOD in the mid-visible ($0.555 \mu\text{m}$) compare within 0.03. Not only is the AOD at this single wavelength retrieved with good accuracy, but the retrieval also reproduces the spectral behavior of the AOD well. The latter contains valuable information on the aerosol size distribution.

The observed AOD is of the order of 0.3-0.7 at $0.659 \mu\text{m}$ (see Figure 4.1c). In oceanic background conditions, values of 0.05-0.08 are observed, see chapter 3. The high optical depth observed during TARFOX, together with the strong wavelength dependence (Figure 4.2), indicates that the aerosol is predominantly of anthropogenic origin.



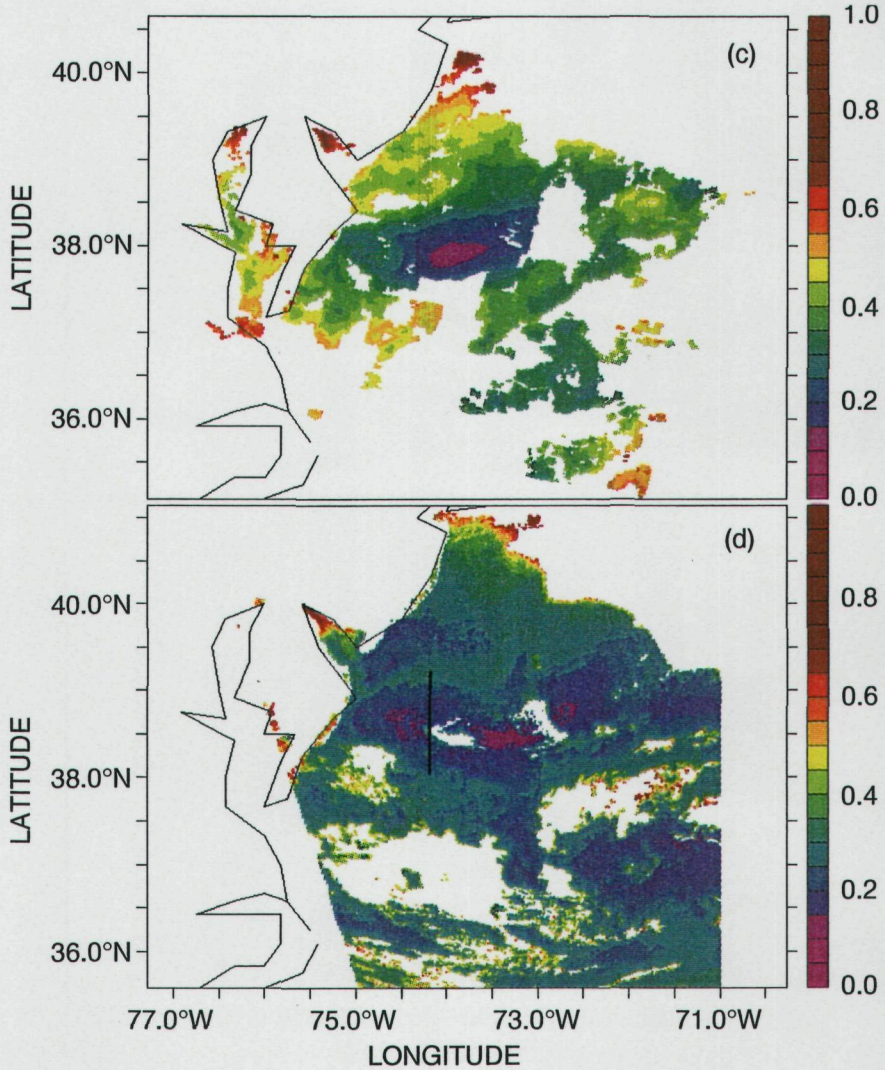


Figure 4.1: (a) ATSR-2 near-infrared ($0.865 \mu\text{m}$) image for July 25, 1996, 1552 UTC; (b) AVHRR near-infrared ($0.84 \mu\text{m}$) image for July 25, 1996, 1845 UTC; (c) ATSR-2 retrieved aerosol optical depth at $0.659 \mu\text{m}$ (the box indicates the position of the UW C-131A during the overpass); (d) AVHRR retrieved aerosol optical depth at $0.64 \mu\text{m}$, the UW C-131A flight track is indicated by the black line oriented in a S-N direction at 74.2°W .

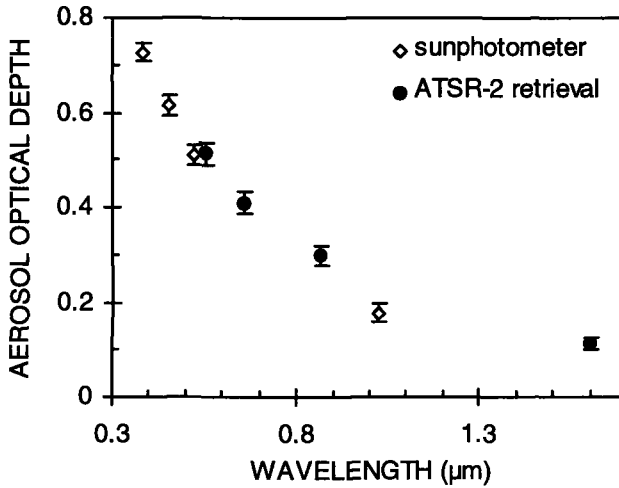


Figure 4.2: Aerosol optical depth retrieved from ATSR-2 data, and aerosol optical depth derived from colocated airborne sunphotometer measurements. Error bars indicate the standard deviation.

4.4.3 AVHRR Retrieval

On July 25, the NOAA-14 satellite passed over the TARFOX area at 1845 UTC, almost 3 hours after the ERS-2 pass. For application of the aerosol retrieval to the AVHRR data, the visible and near-infrared channels (channels 1 and 2) were calibrated using postlaunch calibration methods [Rao and Chen, 1996]. To identify cloud-free pixels over the ocean, a very simple empirical land/cloud screening method was used. For every pixel the channel 1 to channel 2 reflectance ratio, S_{12} , was computed. All pixels for which $1.5 < S_{12} < 3.5$ were identified as cloud-free ocean pixels [Wagner et al., 1997]. The same sunglint criteria as for the ATSR-2 were applied. The AVHRR near-infrared (channel 2) image together with the retrieved AOD for channel 1 ($0.64 \mu\text{m}$) is shown in Figures 4.1b and 4.1d. In general, the AVHRR AOD image (Figure 4.1d) shows similar features as the ATSR-2 image (Figure 4.1c). The region with relatively low AOD is also present in the AVHRR image, although less obvious because of the clouds in this region. Also, the observed AOD gradients in the AVHRR image are smaller than for the ATSR-2 retrieval.

During the NOAA-14 pass the UW C-131A aircraft was heading north at low altitude. This AVHRR underflight started at a latitude of 37.6°N at 1842 UTC and ended at 38.7°N at 1906 UTC. As shown in Figure 4.1d, the flight track starts in the region with low AOD and passes right through the AOD gradient. Before and after the low-altitude track, the airplane made a vertical profile. For comparison of the AVHRR optical depth with the sunphotometer data, the latter were converted to $0.64 \mu\text{m}$. The AOD can often be represented

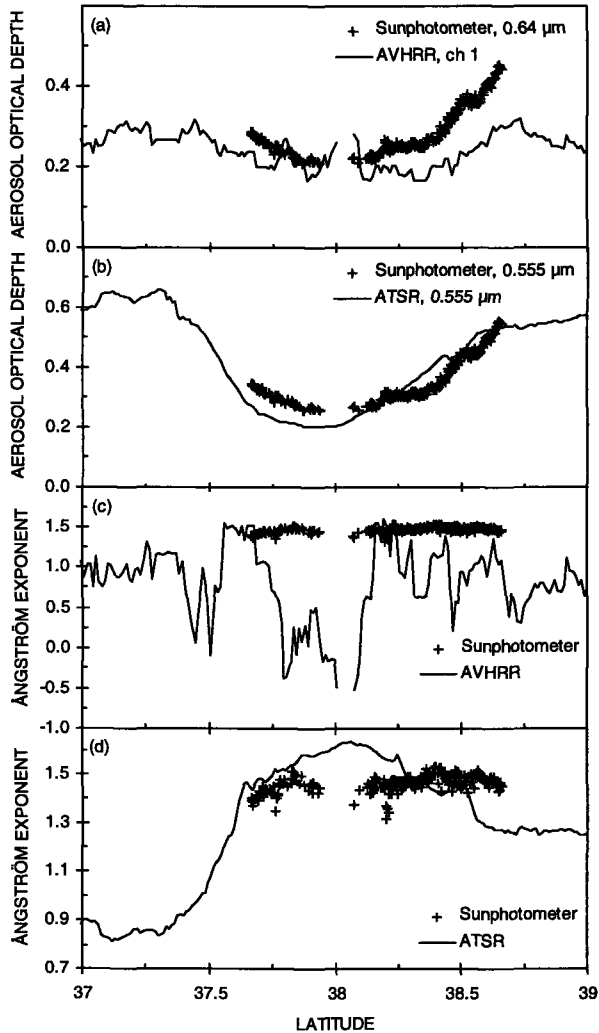


Figure 4.3: Aerosol optical depth and Ångström wavelength exponent derived from the six-wavelength sunphotometer aboard the UW C-131A, the ATSR-2, and the AVHRR. (a) AVHRR retrieved aerosol optical depth for channel 1 ($0.64 \mu\text{m}$) and sunphotometer derived aerosol optical depth at this wavelength, plotted as a function of latitude; (b) same as Figure 4.3a but for ATSR-2 retrieved aerosol optical depth at $0.555 \mu\text{m}$ and sunphotometer derived values at this wavelength; (c) Ångström wavelength exponent derived from AVHRR and from sunphotometer data, plotted as a function of latitude; (d) same as Figure 4.3c but for the Ångström wavelength exponent derived from ATSR-2 and from sunphotometer data.

by a power law function [Ångström, 1961]:

$$AOD(\lambda) \sim \lambda^{-\alpha} \quad (4.2)$$

where λ is the wavelength and α is the Ångström wavelength exponent.

Such a power law fit was used to convert the sunphotometer data to 0.64 μm . In Figure 4.3a the AVHRR channel 1 (effective wavelength 0.64 μm) AOD is compared with the sunphotometer derived AOD at 0.64 μm . The AVHRR AOD is averaged over a small longitude interval between 74.15 and 74.20° W. Figure 4.3a shows good correlation between the sunphotometer derived AOD and the AVHRR channel 1 AOD, except for two regions between 37.7 and 38.1° N. Both peaks in the retrieved AOD in that region are caused by clouds. Outside the cloud-contaminated areas, the trends and features in the data trace very well. Over the whole track the AVHRR retrieved AOD is 0.05-0.15 lower than the sunphotometer derived value. The ATSR-2 data and the size distributions measured with the PCASP on board the UW C-131A indicated that the aerosol was of anthropogenic origin. When the aerosol type in the AVHRR retrieval was fixed to the anthropogenic type, the difference between the retrieval and sunphotometer derived values was <0.1 .

Despite the 3 hour timespan between the ATSR-2 and AVHRR overpass, the AOD patterns (Figures 4.1c and 4.1d) compare well. Therefore it is interesting to compare the ATSR-2 retrieval with the sunphotometer data measured 3 hours later. Figure 4.3b compares the retrieved ATSR-2 AOD at 0.555 μm with the sunphotometer derived value at this wavelength. To take into account the consequences of advection, the retrieved AOD was averaged between 73.5 and 74.5° W. The difference between the ATSR-2 retrieval and the sunphotometer derived values is <0.1 over the entire flight track. In the center of the region with low optical depth, the ATSR-2 AOD is somewhat lower. This difference might be caused by the 3 hour timespan between the airplane and the satellite measurement. Also, the ATSR-2 retrieval was averaged over a large area, whereas the sunphotometer measures along one single track.

The spectral behavior of the AOD depends strongly on the aerosol size distribution. The Ångström wavelength exponent α (equation (2)) is related to the slope of the particle size distribution. When α increases, this indicates that the aerosol optical properties are increasingly dominated by particles smaller than the wavelength. When large particles dominate the aerosol optical properties, the Ångström wavelength exponent tends toward zero. In Figure 4.3d the Ångström wavelength exponent derived from the sunphotometer's 0.525 and 1.021 μm channels is plotted as a function of the latitude, together with the Ångström wavelength exponent computed from the ATSR-2 0.555 and 0.865 μm channels. The ATSR-2 data were averaged over the same longitude range as in Figure 4.3b. The absolute values of the sunphotometer and ATSR-2 Ångström wavelength exponent are in good agreement. At low latitude, the sunphotometer data seem to follow the trend in the ATSR-2 data. For higher latitudes the sunphotometer data seem to be fixed around 1.5, whereas the ATSR-2 Ångström wavelength exponent decreases. The retrieved AOD (Figure 4.3b) and the retrieved Ångström wavelength exponent (Figure 4.3d) are strongly anticorrelated.

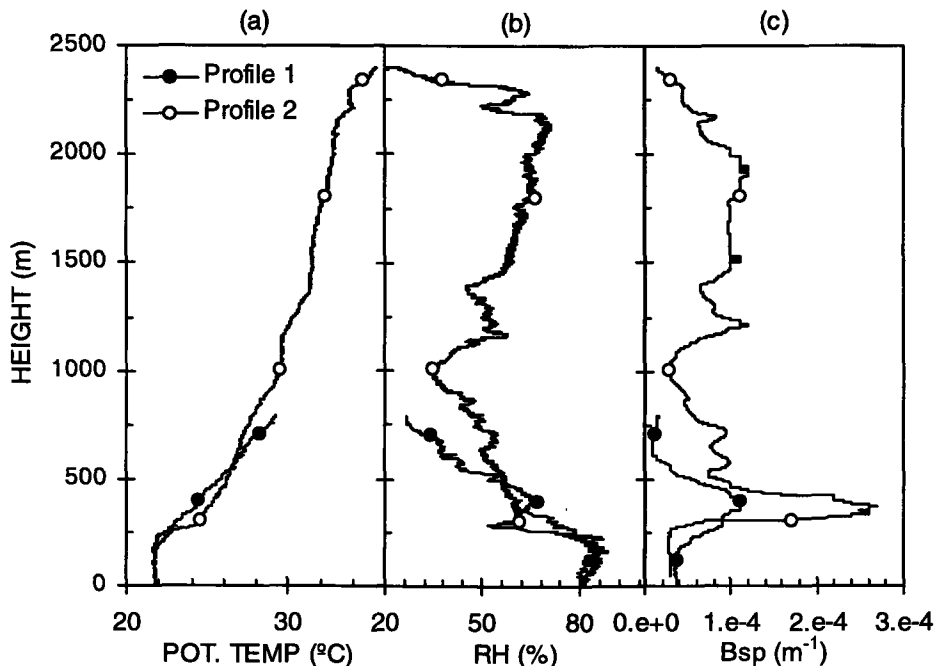


Figure 4.4: Comparison between profile 1 (near 37.8° N, 74.4° W) and profile 2 (near 38.6° N, 74.2° W). (a) Potential temperature plotted as a function of height; (b) relative humidity as a function of height; and (c) the dry aerosol scattering coefficient (B_{sp}) at 0.550 μm plotted as a function of height.

These figures show that when the AOD is at its maximum, the Ångström wavelength exponent is at its minimum, and vice versa. This observation indicates that in this case at low AOD the aerosol slope of the size distribution is steeper (relatively more small particles) than at higher AOD.

In Figure 4.3c the Ångström wavelength exponent derived from the AVHRR retrieval is plotted together with the sunphotometer derived data. The AVHRR derived values for the Ångström wavelength exponent clearly show large variations. This variability is caused by the lack of spectral information due to the wide spectral bands of the AVHRR, and the large digitization step, especially in channel 2.

4.4.4 Aerosol Optical Depth Gradient

AOD gradients as observed in Figures 4.1c and 4.1d can be caused by a difference in the “dry” aerosol properties, by a difference in relative humidity, or by a combination of these effects. Most aerosol particles are hygroscopic; they accrete water when the relative humidity increases. Therefore the scattering coefficient

(and thus the AOD) also increases with increasing relative humidity. A change in the dry aerosol properties includes all changes in concentration, size distribution, and chemical composition, except changes due to relative humidity. The question is whether it is possible to distinguish between an AOD gradient due to a change in the dry aerosol properties and a gradient caused by a change in the relative humidity.

To investigate the nature of the optical depth gradient, the UW C-131A vertical profile data were used. As mentioned above, two profiles were measured around the time of the AVHRR overpass, one in the region with low AOD (profile 1), and one in the region with high optical depth (profile 2). Profile 1 was measured from 750 m down to the surface near 37.9° N, 74.4° W, and profile 2 from the surface up to about 2.5 km, near 38.6° N, 74.2° W. The ratio between the AOD for the profile 2 area to the profile 1 area, as derived from the sunphotometer data, is 1.7 ± 0.1 at $0.550 \mu\text{m}$. The potential temperature and relative humidity for the two profiles are shown in Figures 4.4a and 4.4b, respectively. Both profiles show a mixed layer depth of approximately 250 m. The relative humidity in this layer is about 85%. Above this mixed layer the atmosphere is stable. In Figure 4.4c the dry aerosol scattering coefficient as a function of height is presented. In the mixed layer the dry scattering coefficient is relatively low and constant with height. Just above this layer there is a strong peak in the dry scattering coefficient. This peak is much stronger for profile 2 than for profile 1. Above this maximum the scattering coefficient is still higher than in the mixed layer. This vertical aerosol distribution can be explained by a mixed layer of marine origin, with layers containing anthropogenic aerosol at altitudes aloft. The dry AOD between the surface and 790 m for profiles 1 and 2 was computed by integrating the dry scattering coefficient. The ratio between the AODs in this layer for profiles 2 and 1 is 2.0, 1.9, and 1.7 for 0.450 , 0.550 , and $0.700 \mu\text{m}$, respectively. These numbers are similar to the AOD ratio of 1.7 ± 0.1 at $0.550 \mu\text{m}$, as derived from the sunphotometer. The relative humidity profiles are very similar, and thus cannot explain a 70% higher total AOD for profile 2. Therefore the observed AOD gradient is likely due to a change in the dry aerosol properties. It is noted that only a small part of the AOD is in the layer below 790 m (see Figure 4.4c). Unfortunately, we have no data above 790 m to support this conclusion.

4.5 Conclusions

AOD retrieved from satellite data have been compared to aircraft sunphotometer data. The data were obtained on the eastern seaboard of the United States on July 25, 1996. Aerosol retrieval using ATSR-2 data compares very well with collocated measurements of an airborne sunphotometer. In the mid-visible the difference between the ATSR-2 retrieval and the sunphotometer values was < 0.03 . Also the spectral behavior of the AOD was retrieved accurately. The latter contains valuable information on the aerosol size distribution. AVHRR retrievals for the same day were somewhat more problematic. The AOD for AVHRR channel

1 ($0.64 \mu\text{m}$) correlated well with the sunphotometer data, but the absolute values of the satellite retrieval were 0.05 to 0.15 lower. The Ångström wavelength exponent was determined from both the ATSR-2 and AVHRR. The ATSR-2 derived values are in good agreement with the values from the sunphotometer. The Ångström exponent determined from the AVHRR shows very large variations, caused by the lack of spectral information due to the wide spectral bands, and the large digitization steps in the data.

Both the ATSR-2 and the AVHRR retrieval showed a strong horizontal aerosol gradient. These gradients could have been caused by either a change in the relative humidity or changes in the dry aerosol properties. To investigate the nature of the aerosol gradient, aircraft profile data of temperature, relative humidity, and (dry) aerosol scattering coefficient were used. It was concluded that the aerosol gradient was likely due to changes in the dry aerosol properties.

Acknowledgments

The work described in this paper is supported by the Netherlands Space Research Organization (SRON), contract EO-008. The ATSR-2 data were kindly provided by the European Space Agency (ESA-ESRIN), contract NL-108. The University of Washington contribution to this study was supported by NSF grants ATM-9412082 and ATM-9408941, and the NASA EOS SAGE-III Science Program. This research was conducted as part of the Tropospheric Aerosol Radiative Forcing Observational Experiment (TARFOX), which is a contribution to the International Global Atmospheric Chemistry (IGAC) core project of the International Geosphere-Biosphere Programme (IGBP). Financial support for the measurements and analyses was provided by the U.S. National Aeronautics and Space Administration and the U.S. National Science Foundation. The authors like to thank Robert Koelemeijer of the Royal Netherlands Meteorological Institute (KNMI) for his help with the ATSR-2 data. Part of the work described here was performed while J.P. Veefkind was visiting the Naval Postgraduate School, Department of Meteorology. The Ferret analysis package was used in the preparation of this work (available at <http://ferret.wrc.noaa.gov/>).

Bibliography

- Ångström, A. (1961). Techniques of determining the turbidity of the atmosphere. *Tellus*, 13:214–223.
- Cox, C. and Munk, W. (1954). Statistics of the sea surface derived from sun glitter. *J. Mar. Res.*, 13:198–227.
- Dalu, G. (1986). Satellite remote sensing of atmospheric water vapour. *Int. J. Remote Sens.*, 7:1089–1097.
- Durkee, P. A., Jensen, D. R., Hindman, E. E., and VonderHaar, T. H. (1986). The relationship between marine aerosols and satellite detected radiance. *J. Geophys. Res.*, 91:4063–4072.

- Durkee, P. A., Pfeil, F., Frost, E., and Shema, R. (1991). Global analysis of aerosol particle characteristics. *Atmos. Environ.*, 24A:2457–2471.
- Gathman, S. G. and Davidson, K. L. (1993). The navy oceanic vertical aerosol model. Technical report, NRAD, San Diego, Calif.
- Hobbs, P. V. (1999). An overview of the university of washington airborne measurements and results from the tropospheric aerosol radiative forcing observational experiment (tarfox). *J. Geophys. Res.*, 104:2233–2238.
- Husar, R. B., Prospero, J. M., and Stowe, L. L. (1997). Characterization of tropospheric aerosols over the oceans with the noaa advanced very high resolution radiometer optical thickness operational product. *J. Geophys. Res.*, 102:16,889–16909.
- Kaufman, Y. J. (1995). Remote sensing of direct and indirect aerosol forcing, in: *Aerosol forcing of climate*. In Charlson, R. J. and Heintzenberg, J., editors, *Aerosol forcing of climate*, pages 297–332. John Wiley, New York.
- Kidwell, K. B. (1997). Noaa polar orbiter data users guide, aug. 1997 revision. Technical report, Natl. Oceanic and Atmos. Admin., Silver Spring, Md. (Available at <http://www2.ncdc.noaa.gov/docs/podug>).
- Koepke, P. (1984). Effective reflectance of oceanic whitecaps. *Appl. Opt.*, 23:1816–1824.
- Matsumoto, T., Russell, P. B., Mina, C., and Ark, W. V. (1987). Airborne tracking sunphotometer. *J. Atmos. Oceanic Technol.*, 4:336–339.
- Morel, A. (1988). Optical modeling of the upper ocean in relation to its biogenous matter content (case i waters). *J. Geophys. Res.*, 93:10,749–10,768.
- Rao, C. R. N. and Chen, J. (1996). Post-launch calibration of the visible and near-infrared channels of the advanced very high resolution radiometer on the noaa-14 spacecraft. *Int. J. Remote Sens.*, 17:2743–2747.
- Russell, P. B., Hobbs, P. V., Stowe, S. L., and L., L. (1999a). Aerosol properties and radiative effects in the u.s. east coast haze plume: An overview of the tropospheric aerosol radiative forcing observational experiment (tarfox). *J. Geophys. Res.*, 104:2213–2221.
- Russell, P. B., Livingston, J. M., Dutton, E. G., Pueschel, R. F., Reagan, J. A., DeFoor, T. E., Box, M. A., Allen, D., Pilewskie, P., Herman, B. M., Kinne, S. A., and Hofmann, D. J. (1993). Pinatubo and pre-pinatubo optical depth spectra: Mauna loa measurements, comparisons, inferred particle size distributions, radiative effects, and relationship to lidar data. *J. Geophys. Res.*, 98:22,969–22,985.
- Russell, P. B., Livingston, J. M., Hignett, P., Kinne, S., Wong, J., Chien, A., Bergstrom, R., Durkee, P. A., and Hobbs, P. V. (1999b). Aerosol-induced radiative flux changes off the united states mid-atlantic coast: Comparison of values calculated from sunphotometer and in situ data with those measured by airborne pyranometer. *J. Geophys. Res.*, 104:2289–2307.

- Schwartz, S. E. (1996). The whitehouse effect- shortwave radiative forcing of climate by anthropogenic aerosols, an overview. *J. Aerosol Sci*, 27:359–382.
- Stamnes, K., Tsay, S., Wiscombe, W., and Jayaweera, K. (1988). Numerically stable algorithm for discrete-ordinate-method radiative transfer in multiple scattering and emitting layered media. *Appl. Opt.*, 27:2502–2509.
- Takhashima, K. and Masuda, K. (1985). Degree of radiance and polarization of the upwelling radiation from an atmosphere-ocean system. *Appl. Opt.*, 24:2423–2429.
- Tanré, D., Herman, M., Deschamps, P. Y., and De, L. A. (1979). Atmospheric modeling for space measurements of ground reflectances including bi-directional properties. *Appl. Opt.*, 18:3587–3594.
- Tanré, D., Holben, B. N., and Kaufman, Y. J. (1992). Atmospheric correction for noaa-avhrr products: Theory and application. *IEEE Trans. Geosci. Remote Sens.*, 30:231–248.
- Wagener, R., Nemesure, S., and Schwartz, S. E. (1997). Aerosol optical depth over oceans: High space and time resolution retrieval and error budget from satellite radiometry. *J. Atmos. Oceanic Technol.*, 14:577–590.
- Wang, M. and Gordon, H. R. (1994). Radiance reflected from the ocean-atmosphere system: synthesis from individual components of the aerosol size distribution. *Appl. Opt.*, 33:7088–7095.

Chapter 5

Retrieval of Aerosol Optical Depth over Land using two-angle view Satellite Radiometry during TARFOX

*This chapter was published in Geophysical Research Letters:
J.P. Veeffkind, G. de Leeuw, and P.A. Durkee, Retrieval of Aerosol Optical Depth
over Land using two-angle view Satellite Radiometry during TARFOX, Geophys.
Res. Lett., 25, 3135-3138, 1998.*

Abstract

A new aerosol optical depth retrieval algorithm is presented that uses the two-angle view capability of the Along Track Scanning Radiometer 2 (ATSR-2). By combining the two-angle view and the spectral information this so-called dual view algorithm separates between aerosol and surface contributions to the top of the atmosphere radiance. First validation of the dual view algorithm was performed during the Tropospheric Aerosol Radiative Forcing Observational Experiment (TARFOX), which was conducted at the mid-Atlantic coast of the United States in July 1996. The satellite retrieved spectral aerosol optical depth is in good agreement with the aerosol optical depth from ground-based Sun/sky radiometers in three out of four cases. This shows the potential of aerosol retrieval over land using two-angle view satellite radiometry.

5.1 Introduction

Atmospheric aerosol particles play an important role in the Earth's radiation balance. They scatter and absorb solar radiation (direct effect) and affect the albedo and lifetimes of clouds (indirect effect). The radiative forcing by man-made aerosols of the combined direct and indirect effects is estimated to be of the same order of magnitude, but opposite of sign, as the radiative forcing by the anthropogenic greenhouse gases. Aerosols are considered one of the largest uncertainties in today's climate modeling. To a large extent this uncertainty is caused by a lack of data on a global scale. Due to the short lifetimes of aerosols in the troposphere (hours to days) and due to the occurrence of many different sources with different spatial extents and emissions, the aerosol is highly variable in both space and time. This applies to the concentration, the size distribution, and the chemical composition, and therefore also to the aerosol optical properties. Only satellite remote sensing can provide the spatial and temporal resolution to measure the inhomogeneous aerosol fields. However, retrieval of aerosol properties from satellite measured radiances is not straightforward. The radiance at the top of the atmosphere is the sum of several components, including aerosol scattered light and light reflected by the underlying surface. When the surface albedo is high, as is often the case over land, the contribution of aerosol scattering to the total radiance may be relatively small, which renders the retrieval of the aerosol contribution rather uncertain. Several methods have been proposed to distinguish between contributions to the satellite measured radiance by aerosols and by the surface (for a review see Kaufman et al. [1997a]). The use of *multi-angle satellite radiometry for aerosol retrieval* was proposed by Martonchik and Diner [1992]. However, data from multi-angle satellite radiometers is scarce. Flowerdew and Haigh [1996] presented an algorithm that uses the two-angle view data from the Along Track Scanning Radiometer 2 (ATSR-2).

In this contribution, we present a new algorithm based on ATSR-2 data in which the surface reflection is treated in a similar way as by Flowerdew and Haigh [1996]. However, the new algorithm uses not only the information from the two-angle view, but also the spectral information to distinguish between atmospheric and surface contributions to the top of the atmosphere radiance. The spectral aerosol optical depth (AOD) is computed using an aerosol model that fits the spectral measurements best. First validation of the dual view algorithm was performed during the Tropospheric Aerosol Radiative Forcing Observational Experiment (TARFOX), which was conducted at the mid-Atlantic coast of the United States, in July 1996 [Russell et al., 1999] by comparing satellite retrievals to ground based measurements. Validation in these so-called column closure experiments permits the assessment of measurement uncertainties, and can establish credibility for satellite remote sensing of aerosol properties.

5.2 The ATSR-2 sensor

The ATSR-2 was launched on board the European ERS-2 satellite in April 1995. ATSR-2 is a radiometer with 7 wavelengths, 4 of these bands are in the visible and near-infrared (effective wavelengths 0.555, 0.659, 0.865, and 1.6 μm) and potentially useful for aerosol retrieval. The spatial resolution of the ATSR-2 is $1 \times 1 \text{ km}^2$ at nadir, and the swath width is 500 km. The ATSR-2 has a conical scanning mechanism, thus producing two views of each region: first a forward view (zenith angle approximately 55°) and about two minutes later a nadir view. The horizontal distance of the lower troposphere covered by the combined forward and nadir measurements is less than 10 km. On these spatial and temporal scales the atmosphere is assumed to be invariable and horizontally homogeneous.

5.3 The Dual View Algorithm

The dual view algorithm applies only to cloud-free scenes. For such cases, the total (aerosol + Rayleigh) optical depth in the visible and near-infrared is usually less than 1. Over land, the contribution of the surface reflection in this optical depth regime is dominated by the direct contribution, i.e. photons that are reflected at the surface and transmitted on their downward and upward path through the atmosphere. Away from the surface hot-spot, a Lambertian surface may be assumed in such cases [Flowerdew and Haigh, 1996]. The orbit of the ERS-2 is such that the ATSR-2 rarely observes the surface hot-spot in the Northern Hemisphere [Godsalve, 1995]. For a Lambertian surface the reflectance at the top of the atmosphere (ρ) is given by:

$$\rho(\lambda) = \rho_{atm}(\lambda) + \frac{\rho_{sfc}(\lambda)}{1 - \rho_{sfc}(\lambda) \cdot s(\lambda)} T(\lambda) \quad (5.1)$$

where:

ρ_{atm} is the contribution of atmospheric scattering;

ρ_{sfc} is the surface albedo;

s is the spherical albedo of the atmosphere;

T is the transmittance of the atmosphere;

and λ is the wavelength.

The surface reflection depends both on the wavelength and on the geometry. However, the surface reflection can be approximated by a part that describes the variation with the wavelength and a part that describes the variation with the geometry [Flowerdew and Haigh, 1995]. Under this assumption, the forward view surface albedo ($\rho_{sfc,f}$) may be written as:

$$\rho_{sfc,f}(\lambda) = k \cdot \rho_{sfc,n}(\lambda) \quad (5.2)$$

where $\rho_{sfc,n}$ is the nadir view albedo; and k is the ratio between the forward and the nadir surface reflection.

The ratio k depends only on the variation of the surface reflection with the geometry and is assumed to be independent of the wavelength. Experimental data shows that the surface reflectances at wavelengths in the visible (0.555 and 0.659 μm) are proportional to those in the mid-infrared (1.6 and 2.1 μm) [Kaufman et al., 1997b]. Note that this does not apply to the 0.865 μm channel, which therefore can not be used.

For the forward view, substituting equation (5.2) into equation (5.1) yields:

$$\begin{aligned}\rho_f(\lambda) &= \rho_{atm,f}(\lambda) + \frac{k \cdot \rho_{sfc,n}(\lambda)}{1 - k \cdot \rho_{sfc,n}(\lambda) \cdot s(\lambda)} T_f(\lambda) \\ &\approx \rho_{atm,f}(\lambda) + \frac{k \cdot \rho_{sfc,n}(\lambda)}{1 - \rho_{sfc,n}(\lambda) \cdot s(\lambda)} T_f(\lambda)\end{aligned}\quad (5.3)$$

where the subscripts f are for the forward view. The approximation in equation (5.3) has been made because in general $k \cdot \rho_{sfc,n}(\lambda) \cdot s(\lambda) \ll 1$.

For most continental aerosol types, except for desert dust, the aerosol extinction decreases rapidly with wavelength and the AOD at 1.6 μm will be small as compared to the AOD in the visible. Ignoring the atmospheric contribution at 1.6 μm , k is approximated as the ratio between the top of the atmosphere reflectances for the forward and for the nadir view at this wavelength. Since k is assumed independent of the wavelength, this value for k can also be used for the visible channels of the ATSR-2 (0.555 and 0.659 μm). The unknown surface albedo can be eliminated by using equation (5.1) for the nadir view and equation (5.3) for the forward view:

$$\frac{\rho_n(\lambda) - \rho_{atm,n}(\lambda)}{T_n(\lambda)} = \frac{\rho_f(\lambda) - \rho_{atm,f}(\lambda)}{k \cdot T_f(\lambda)} \quad (5.4)$$

where the subscripts n are used for the nadir view.

In equation (5.4), ρ_n and ρ_f are measured and k is approximated as described above. All other terms are a function of the AOD. To compute the AOD from equation (5.4), an aerosol model is applied. The dual view algorithm has been applied to an area at the east coast of the United States. The aerosol in this region is assumed to be an external mixture of sea-salt aerosol and aerosol from anthropogenic sources. These two aerosol types are defined from the Navy Oceanic Vertical Aerosol Model (NOVAM) [de Leeuw et al., 1989]. The mixture of the two aerosol types that fits the spectral behavior of the measured reflectance in the 0.555, 0.659 and 1.6 μm channels best, is used to compute the AOD and the surface albedo for these channels.

5.4 Results and Discussion

During the TARFOX intensive field campaign from 10 to 31 July 1996, the ATSR-2 passed seven times over the area. Figure 5.1 shows the near-infrared image and the AOD as determined by the dual view algorithm for the ATSR-2 pass on 25 July 1996. Figure 5.1 illustrates the potential of the dual view algorithm for

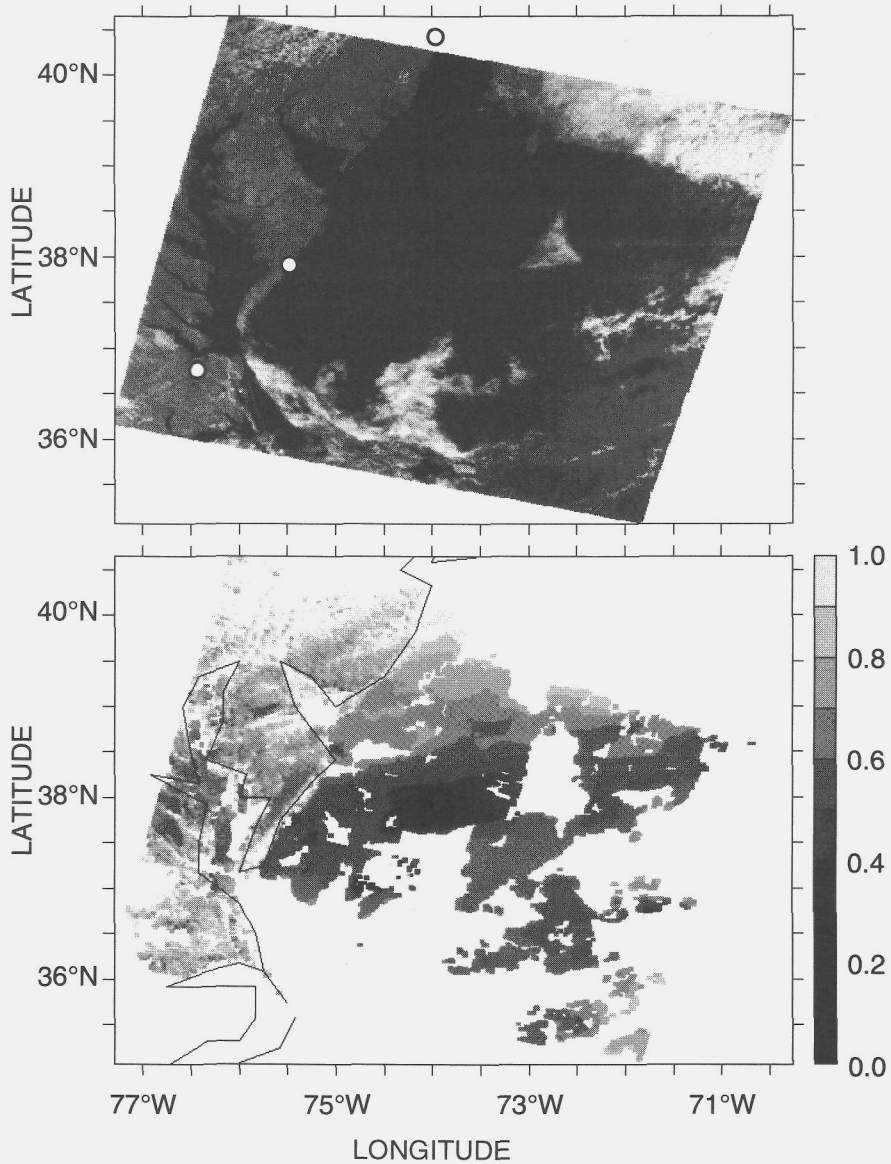


Figure 5.1: Near-infrared image ($1.6 \mu\text{m}$) (upper) and aerosol optical depth retrieved using the dual view algorithm for $0.659 \mu\text{m}$ (lower), for the ATSR-2 overpass over the TARFOX area on July 25, 1996, 15:52 UTC. In the near-infrared image, the symbols indicate the ground stations used in this study (see text).

AOD retrieval over both land and water surfaces. The AOD image for this day shows a strong spatial gradient. A region with relatively low AOD values (0.2 at $0.659 \mu\text{m}$) is centred around 38°N 74°W . This AOD pattern was supported by satellite retrievals from algorithms that compute the AOD over the ocean (see chapter 4), as well as by airborne Lidar measurements [Ferrare et al., 1997]. Despite the differences in surface reflective properties between land and ocean, Figure 5.1 does not show distinct jumps in the retrieved AOD across the land to sea boundaries. Over land, the uncertainty in the retrieved AOD is larger than over the ocean, due to the higher and less homogeneous surface albedo, and the non-perfect match between the forward and nadir view pixel. At the land to sea boundary the dual view algorithm tends to fail. This is caused by the small difference in scene between the forward and the nadir view of the ATSR-2, in combination with the suddenly changing surface albedo at the coastline.

During TARFOX the aerosol optical depth was measured at five ground-based stations. At each station a Sun/sky radiometer measured the direct solar radiation in six spectral bands (0.340, 0.380, 0.440, 0.670, 0.940 and $1.020 \mu\text{m}$) [Holben et al., 1998]. Figure 5.2a shows the comparison between the aerosol optical depth as determined with the Sun/sky radiometer at Wallops Island (37.93°N , 75.47°W) and the colocated AOD from the dual view algorithm, for 25 July 1996. The Sun/sky radiometer measurements and the ATSR-2 image were within 3 minutes of each other. The AOD from the Sun/sky radiometer and the AOD retrieval over land are in excellent agreement. Not only the AOD at a single wavelength is retrieved accurately, but also the spectral behavior of the AOD. The latter contains important information on the aerosol size distribution. The high AOD observed on 25 July 1996, in combination with the rapid decrease of the AOD with the wavelength, indicates that the aerosol is predominantly of anthropogenic origin. This is supported by in situ measurements of physical and chemical aerosol properties [Hegg et al., 1997].

The difficulty of comparisons, similar to the one shown in Figure 5.2a, is to find co-located ground-based and satellite measurements. Often the satellite retrieval or the Sun/sky radiometer data is missing due to clouds over the ground station at the time of the satellite overpass. When the AOD varies little in space and time, the Sun/sky radiometer measurements closest to the time of the overpass can be compared to satellite retrieval data closest to the ground station. Such a comparison is shown in Figure 5.2b for Wallops Island for 31 July 1996. In this case the Sun/sky radiometer measurement was taken approximately 1 hour after the satellite overpass, and the satellite retrieval is for an area within 20 km of the ground station. Figures 5.2c and 5.2d show similar comparisons for Sandy Hook (40.43°N , 73.98°W) for 28 July 1996, and for Hampton Road (36.77°N , 76.43°W) for 31 July. All the cases with high AOD (Figures 5.2a, b and d) show good agreement between AOD determined from the Sun/sky radiometer and from the dual view algorithm. Figure 5.2c shows the performance of the dual view algorithm for low AOD. For this case the retrieval in the visible is about a factor of two larger than Sun/sky radiometer derived AOD. However, the standard deviation in the retrieval is relatively large, and the satellite retrieved and Sun/sky radiometer derived values are within the experimental uncertainty.

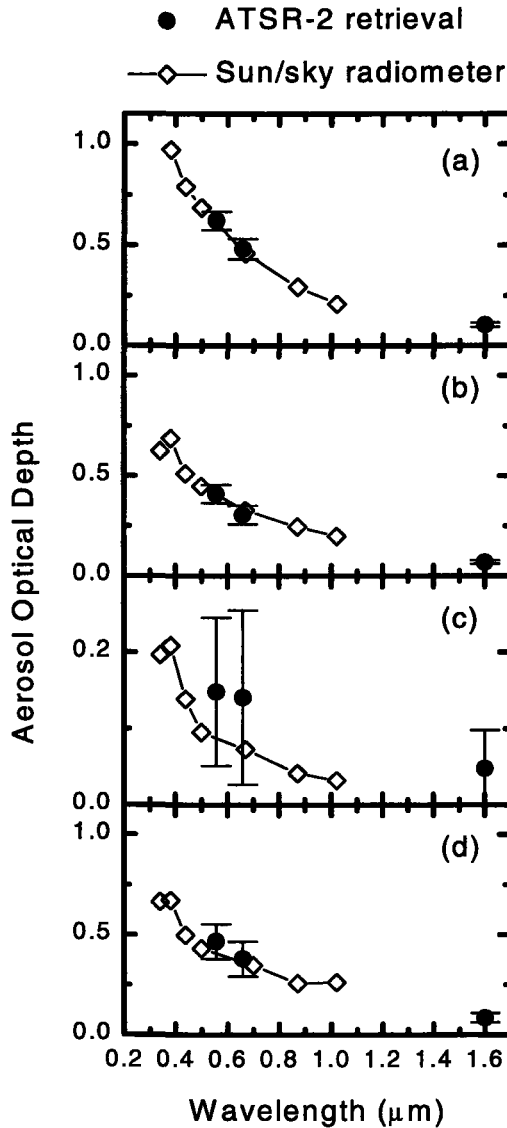


Figure 5.2: AOD determined from the Sun/sky radiometer measurements, and AOD from the dual view algorithm using ATSR-2 data. Error bars indicate the standard deviation. Fig. 5.2a is for Wallops Island (37.93° N, 75.47° W) for 25 July 1996; Figure 5.2b is for Wallops Island for 31 July 1996, Fig. 5.2c is for Sandy Hook (40.43° N, 73.98° W) for 28 July 1996, and Fig. 5.2d for Hampton Roads (36.77° N, 76.43° W) for 31 July, 1996.

The large variation is caused by the difference scene between the forward and nadir view, in combination with the inhomogeneous surface albedo over land.

5.5 Conclusions

An aerosol optical depth retrieval algorithm is presented that uses both the two-angle view and the spectral information of the ATSR-2 measurements. This so-called dual view algorithm applies both over land and over the ocean. Aerosol optical depth retrievals over land are compared to Sun/sky radiometer measurements during TARFOX. For three cases with high aerosol optical depth (0.3-0.5 at $0.659 \mu\text{m}$), the satellite retrieved aerosol optical depth and that derived from the Sun/sky radiometers are in good agreement. For one case with lower aerosol optical depth (~ 0.1 at $0.659 \mu\text{m}$) the agreement is less good (difference about 100%), but still within the experimental uncertainty. The results of this validation are very encouraging, and new validation studies for different regions will be performed in the near future.

Acknowledgments

The work described in this paper is supported by the Netherlands Space Research Organization (SRON), under contract EO-008. The ATSR-2 data was kindly provided by the European Space Agency (ESA-ESRIN). The authors thank Brent Holben from NASA Goddard Space Flight Center for the AERONET Sun/sky radiometer data. The Ferret analysis package was used in the preparation of this work (available at <http://ferret.wrc.noaa.gov>). Ferret was developed by the NOAA-PMEL, Ocean Climate Research Division.

Bibliography

- de Leeuw, G., Davidson, K. L., Gathman, S. G., and Noonkester, R. V. (1989). Modeling of aerosols in the marine mixed-layer. In *SPIE Proceedings 1115, Propagation Engineering*, pages 287–294.
- Ferrare, R., Schwemmer, G., Melfi, S., Whiteman, D., Guerra, D., and Wooten, D. (1997). Scanning raman lidar measurements of aerosol backscatter and extinction profiles during tarfox. *EOS, Trans. Amer. Geophys. Union*, 78:S81.
- Flowerdew, R. and Haigh, J. (1995). An approximation to improve accuracy in the derivation of surface reflectances from multi-look satellite radiometers. *Geophys. Res. Lett.*, 22:1693–1696.
- Flowerdew, R. and Haigh, J. (1996). Retrieval of aerosol optical thickness over land using the atsr-2 dual-look satellite radiometer. *Geophys. Res. Lett.*, 23:351–354.
- Godsalve, C. (1995). Bi-directional reflectance sampling by atsr-2: a combined orbit and scan model. *Int. J. Rem. Sensing*, 16:269–300.

- Hegg, D. A., Livingston, J., Hobbs, P. V., Novakov, T., and Russell, P. B. (1997). Chemical apportionment of aerosol column optical depth off the mid-atlantic coast of the united states. *J. Geophys. Res.*, 102:25293–25303.
- Holben, B., Eck, T., Slutsker, I., Tanré, D., Buis, J., Setzer, A., Vermote, E., Reagan, J., Kaufman, Y., Nakajima, T., Lavenu, F., Jankowiak, I., and Smirnov, A. (1998). Aeronet- a federated instrument network and data archive for aerosol characterization. *Remote Sens. Environ.*, 66:1–16.
- Kaufman, Y. J., Tanre, D., Nakajima, T., Lenoble, J., Frouin, R., Grassl, H., Herman, B. M., King, M. D., and Teillet, P. M. (1997a). Passive remote sensing of tropospheric aerosol and atmospheric correction for the aerosol effect. *J. Geophys. Res.*, 102:16,815–16,830.
- Kaufman, Y. J., Wald, A. E., Remer, L. A., Gao, B. C., Li, R. R., and Flynn, L. (1997b). The modis 2.1 μm channel correlation with visible reflectances for use in remote sensing of aerosol. *IEEE Trans. on Geosci. and Remote Sens.*, 35:1286–1298.
- Martonchik, J. and Diner, D. (1992). Retrieval of aerosol properties from multi-angle imagery. *IEEE Trans. on Geosci. and Rem. Sensing*, 30:223–230.
- Russell, P. B., Hobbs, P. V., Stowe, S. L., and L., L. (1999). Aerosol properties and radiative effects in the u.s. east coast haze plume: An overview of the tropospheric aerosol radiative forcing observational experiment (tarfox). *J. Geophys. Res.*, 104:2213–2221.

Chapter 6

Regional Distribution of Aerosol over Land derived from ATSR-2 and GOME data

This chapter has been accepted for publication in Remote Sensing of the Environment:

J.P. Veefkind, G. de Leeuw, P. Stammes, and R.B.A. Koelemeijer: Regional Distribution of Aerosol over Land derived from ATSR-2 and GOME data

Abstract

Two aerosol optical depth retrieval algorithms, using different instruments and different methods, are compared. The first method uses both the directional and the spectral information of the Along Track Scanning Radiometer 2 (ATSR-2) to compute the aerosol optical depth in the visible and near-infrared. The second algorithm uses data in the wavelength range between 0.340 and 0.400 μm from the Global Ozone Monitoring Experiment (GOME) to determine the aerosol optical depth in the UV. Both ATSR-2 and GOME are on board the ERS-2 satellite. The two methods are applied to data from the ERS-2 overpass over northwestern Europe on 25 July 1995. The retrieved aerosol optical depths compare favorably. Also, there is good comparison between the satellite retrievals and ground based measurements. Optical depth images show a large aerosol plume over Belgium and northern France. Back-trajectories indicate that the sources for this aerosol plume are the industrialized regions in Germany and Belgium.

6.1 Introduction

Over the past decade, it has been recognized that aerosol particles play an important role in climate and atmospheric chemistry. Aerosol particles affect the Earth's radiation balance in two ways: directly by scattering part of the incoming solar radiation back to space, and indirectly by modifying the albedo and lifetimes of clouds. In a pioneering study, Charlson et al. [1992] showed that the total (direct + indirect) radiative forcing by anthropogenic sulfate aerosol particles is of the same order of magnitude, but opposite of sign, as the radiative forcing by man-made greenhouse gases. Downwind of the major industrial regions, the radiative forcing by the man-made greenhouse gases might be (over)compensated by the combined direct and indirect aerosol effects. It should be noted that besides anthropogenic sulfate aerosols, also anthropogenic carbonaceous and anthropogenic nitrate aerosols contribute significantly to the radiative forcing [Hegg et al., 1997, ten Brink et al., 1996].

The lifetimes of anthropogenic aerosols in the troposphere are of the order of days to a week, which is small as compared to the lifetimes of most of the greenhouse gases. Due to these short lifetimes, in combination with the many different aerosol sources with different spatial extents and emission strengths, the aerosol is highly variable in both space and time. This applies to their concentration, size distribution as well as the chemical composition. Aerosols are considered one of the major uncertainties in today's climate models. To a large extent this uncertainty is caused by a lack of knowledge of the aerosol properties on a global scale. Only satellite remote sensing has the potential to measure the highly variable aerosol field [IPCC, 1995].

Until recently, it was thought that satellite aerosol retrieval was only possible over dark surfaces, such as the ocean. However, new sensors with improved calibration and spectral information over a range of wavelengths, make it possible to retrieve aerosol properties over land [Kaufman et al., 1997a]. The key problem in aerosol retrieval over land is to distinguish between contributions from the aerosol and those from surface reflections to the top-of-the-atmosphere (TOA) radiance. In the UV, the albedo of most land surfaces is relatively low. This property was used by Herman et al. [1997] to detect UV-absorbing aerosols from data obtained by the Total Ozone Mapping Spectrometer (TOMS). Another promising technique for aerosol retrieval over land is the use of two- or multi-angle radiometry. In chapter 5 it was shown that aerosol retrieval over land using data from the Along Tracking Scanning Radiometer 2 (ATSR-2), a dual-view imaging radiometer on board the European ERS-2 satellite, compared favorably with ground based sunphotometer measurements. Using the dual-view algorithm proposed in chapter 5, both the aerosol optical depth at a single wavelength, and its spectral behavior can be retrieved. Hence, also important information on the aerosol size distribution can be obtained.

Besides the two-angle view radiometer (ATSR-2), there is also a spectrometer on board the ERS-2 satellite, namely the Global Ozone Monitoring Experiment (GOME). It measures the spectrum of the TOA radiance at wavelengths from 0.240 to 0.790 μm with a spectral resolution of 0.2 to 0.4 nm. The large wave-

length range and high spectral resolution provides the opportunity to apply different aerosol retrieval algorithms to GOME data. However, due to the large pixel size of $320 \times 40 \text{ km}^2$ the application of GOME is limited because most of the retrieval algorithms apply only to cloud-free scenes, which are difficult to find for such large areas. Fortunately, there is a large amount of GOME data from the validation phase (1995-1996) for which the pixel size is $80 \times 40 \text{ km}^2$. This pixel size has been used here. In this contribution a method is presented that uses GOME data in the UV, where the surface albedo is low both over land and over the ocean [Herman and Celarier, 1997]. This method is based on scattering by aerosols in the UV, and therefore differs from the method by Herman et al. [1997], which is based on the extinction by aerosols.

Having both a spectrometer (GOME) and a two-angle view radiometer (ATSR-2) on the same satellite makes it possible to directly compare the two different aerosol retrieval techniques. This is illustrated with data from a case study over northwestern Europe, for a completely cloud-free case on 25 July 1995. To further validate the satellite retrieval methods, the aerosol optical depth determined from the ATSR-2 and GOME data are compared to ground based measurements. Finally, the regional distribution of the aerosol for this case is discussed.

6.2 Aerosol Remote Sensing Methods

Like most remote sensing applications, satellite aerosol retrieval is a so-called ill-posed problem, meaning that there are more unknowns than equations. Retrieval of the aerosol optical depth (AOD) is therefore impossible without applying an aerosol model. In section 6.2.1 we will describe the aerosol model that will be used in the retrieval algorithms. The radiative transfer models used to compute the TOA reflectance will be described in section 6.2.2. In section 6.2.3 and 6.2.4 the algorithms to retrieve aerosol properties from ATSR-2 and GOME data are described. The cloud screening procedure is described in section 6.2.5.

6.2.1 Aerosol Model

The aerosol size distribution and their chemical composition are determined by the geographic locations of emission sources, type of emission, transport and removal processes. Because most aerosol particles are hygroscopic, their size and chemical composition are a function of the relative humidity. In this contribution, retrievals over northwestern Europe will be presented. Large amounts of aerosol precursor gases, such as SO_2 and NO_x , are emitted by the heavily industrialized areas in this region. In the coastal regions aerosol particles from marine origin will be present when the air-mass is advected from the sea. In general, these marine particles which are produced by the breaking of waves, are much larger compared to those from (anthropogenic) continental origin. In the aerosol retrieval algorithms described below, a two-mode aerosol size distribution is used. The smaller mode represents the aerosol particles from anthropogenic (continental) origin, and the larger mode represents the aerosol particles

Wavelength (μm)	Anthropogenic	Marine
0.400	$1.40 - 5.00 \times 10^{-3}$	$1.40 - 5.00 \times 10^{-4}$
0.555	$1.41 - 2.41 \times 10^{-3}$	$1.39 - 5.38 \times 10^{-9}$
0.659	$1.41 - 2.41 \times 10^{-3}$	$1.38 - 3.24 \times 10^{-8}$
0.865	$1.40 - 2.42 \times 10^{-3}$	$1.38 - 2.95 \times 10^{-6}$
1.600	$1.35 - 2.63 \times 10^{-3}$	$1.36 - 2.87 \times 10^{-4}$

Table 6.1: Complex refractive index for the anthropogenic and marine modes at 80% relative humidity.

from marine origin. The size distributions of the individual modes are slightly different from the popular lognormal size distributions, and are described by [Gathman et al., 1989, Gathman and Davidson, 1993]:

$$\frac{dN}{dr} = \frac{A}{f} \exp\left[-\ln^2\left(\frac{r}{f \cdot r_0}\right)\right], \quad (6.1)$$

where:

N is the total number of particles per cm^3 ;

r is the radius of the particles;

r_0 is the mode radius;

A is the amplitude; and

f is the swelling factor depending on the relative humidity and defined as 1 for 80% relative humidity.

The mode radius for the anthropogenic mode is taken as $r_0=0.03 \mu\text{m}$, and for the marine aerosols as $r_0=0.24 \mu\text{m}$. The relative humidity is assumed to be 80%. The complex refractive indices for the two aerosol types at 80% relative humidity are listed in Table 6.1. The optical properties for the anthropogenic and marine modes were computed using the Mie scattering code MIEVU [De Rooij and Van der Stap, 1984]. Using Mie theory implies that the particles are assumed spherical. The anthropogenic aerosol particles are predominantly formed by gas-to-particle conversion, which will generally lead to spherical particles. In addition, most of the anthropogenic and sea salt aerosol particles are hygroscopic. The accretion of water vapor by the particles will also lead to particles that are quite spherical.

6.2.2 Radiative Transfer Model

The aerosol retrieval methods compare the measured TOA reflectance to values determined by radiative transfer modeling. Because radiative transfer calculations are time consuming, it is convenient to use pre-calculated lookup tables of the radiative transfer parameters used in the algorithms. Radiative transfer computations were performed to determine these parameters as a function of the Sun/satellite geometry and the wavelength. Lookup tables were created for atmospheres containing the anthropogenic and marine aerosol types (de-

scribed above), as well as for the aerosol-free (Rayleigh) case. Aerosol particles of anthropogenic and marine origin are predominantly situated in the atmospheric boundary layer. For this reason, the atmosphere was divided into two layers: the upper layer containing only molecules, and the lower layer with only aerosols. For the ATSR-2 retrieval algorithm, the lookup tables were computed using the discrete ordinates method [Stamnes et al., 1988], thus ignoring the effects of polarization. For the GOME UV retrieval algorithm the polarization effects are accounted for, by using a doubling-adding radiative transfer code [Evans and Stephens, 1991] to create the lookup tables.

6.2.3 The ATSR-2 dual view algorithm

The ATSR-2 is a radiometer with seven wavelength bands, four of these bands are in the visible and near infrared (effective wavelengths 0.555, 0.659, 0.865 and 1.6 μm) and potentially useful for aerosol retrieval. In-flight calibration of these channels is performed by measuring the solar irradiance during parts of the orbit. The spatial resolution of the ATSR-2 is approximately $1 \times 1 \text{ km}^2$ at nadir, and the swath width is 512 km. The ATSR-2 has a conical scanning mechanism, thus producing two views of each region: first a forward view (viewing zenith angle approximately 56° at the surface), and about two minutes later a nadir view.

The key problem in aerosol retrieval over land is to distinguish between contributions to the TOA reflectance from scattering in the atmosphere, and from reflection by the surface. The so-called dual-view algorithm uses both the directional and the spectral information in the ATSR-2 data to separate between atmospheric and surface contributions [chapter 5]. The dual view algorithm only applies to cloud-free scenes. For such cases the total (aerosol + Rayleigh) optical depth is usually less than 1 in the wavelength range of the ATSR-2. Over land, the contribution of the surface reflectance in this optical depth regime is dominated by the direct contribution, i.e. photons that are reflected at the surface and transmitted on their upward and downward path through the atmosphere. Ignoring the directional effect in the higher order atmosphere-surface interactions, the TOA reflectance measured by the satellite sensor may be approximated by:

$$\rho(\lambda) = \rho_a(\lambda) + \frac{\rho_s(\lambda)}{1 - R_s(\lambda) \cdot s(\lambda)} T(\lambda), \quad (6.2)$$

where:

ρ_a is the contribution of atmospheric scattering (path reflectance);

ρ_s is the directional surface reflectance;

R_s is the surface albedo;

T is the total (direct plus diffuse) transmittance along the downward and upward path through the atmosphere;

s is the spherical albedo of the atmosphere for upward directed irradiance; and

λ is the wavelength.

Note that ρ_a , ρ_s , and T all depend on the Sun/satellite geometry.

Because of the geometry dependence of the surface reflection, ρ_s will have different values for the forward and nadir viewing direction of the ATSR-2. However, the surface reflection can be approximated by a part describing the variation with the wavelength, and a part describing the variation with the geometry [Flowerdew and Haigh, 1995]. Using this approximation, it follows that the ratio between the surface reflectance for the ATSR-2 forward and nadir views is independent of the wavelength. Thus the forward view surface reflection ($\rho_{s,f}(\lambda)$) may be written as:

$$\rho_{s,f}(\lambda) = k \cdot \rho_{s,n}(\lambda), \quad (6.3)$$

where $\rho_{s,n}$ is the nadir view surface reflection; and k is the wavelength-independent ratio between forward and nadir view surface reflection that depends only on the Sun/satellite geometry.

For most continental aerosol types, except for desert dust, the aerosol extinction decreases rapidly with the wavelength and the AOD at 1.6 μm will be small compared to the AOD at wavelengths in the visible. Ignoring the atmospheric contribution at 1.6 μm , the value of k can be estimated from the TOA reflectances for the forward and nadir view at this wavelength. Data presented in Kaufman et al. [1997b] show that for a variety of land surfaces types the surface reflections at 0.555 and 0.659 μm are proportional to those in the mid-infrared (1.6 and 2.1 μm). This does not apply to the 0.865 μm channel, which therefore cannot be used in the dual view algorithm. Equation (6.2) is used to describe the TOA reflectance for the nadir and forward surface reflection, respectively. By combining the forward and nadir view information, the unknown surface reflectance ($\rho_{s,n}$) and the unknown surface albedo (R_s) can be eliminated [chapter 5]:

$$\frac{\rho_n(\lambda) - \rho_{a,n}(\lambda)}{T_n(\lambda)} = \frac{\rho_f(\lambda) - \rho_{a,f}(\lambda)}{k \cdot T_f(\lambda)}, \quad (6.4)$$

where the subscripts n and f refer to the nadir and forward view respectively. For computation of the AOD from equation (6.4) it is assumed that the path reflectance increases linearly with the AOD [Durkee et al., 1986]:

$$\rho_a(\lambda) = \rho_0(\lambda) + c(\lambda) \cdot AOD(\lambda), \quad (6.5)$$

where ρ_0 is the path reflectance for an aerosol free atmosphere; and c is the slope between ρ_a and AOD, which depends on the aerosol phase function.

The AOD is computed from equation (6.4) by substituting (6.5) in (6.4) and applying an iterative procedure. For the i -th iterative step the AOD is given by:

$$AOD^i(\lambda) = \left[\frac{\rho'_n(\lambda)}{T_n^{i-1}(\lambda)} - \frac{\rho'_f(\lambda)}{k^i \cdot T_f^{i-1}(\lambda)} \right] \cdot \left[\frac{c_n(\lambda)}{T_n^{i-1}(\lambda)} - \frac{c_f(\lambda)}{k^i \cdot T_f^{i-1}(\lambda)} \right]^{-1}, \quad (6.6)$$

where $\rho'_n = \rho - \rho_0$.

The ratio k for the i -th iterative step is computed from the 1.6 μm channel as:

$$k^i = \frac{\rho_f(1.6\mu\text{m}) - \rho_{a,f}^{i-1}(1.6\mu\text{m})}{\rho_n(1.6\mu\text{m}) - \rho_{a,n}^{i-1}(1.6\mu\text{m})}, \quad (6.7)$$

The iterative procedure is initiated using $AOD(1.6)=0$. Usually convergence of (6.6) is reached within a few iterative steps.

The spectral AOD is computed using (6.6) for different mixtures of the anthropogenic and marine modes. The method of least squares is used to find the mixture for which the spectral behavior of the retrieved AOD best fits the spectral behavior of the used model AOD.

6.2.4 GOME UV method

GOME is a four-channel grating spectrometer which measures the TOA radiance between 0.240 and 0.790 μm with a spectral resolution of 0.2 to 0.4 nm. The default size of the GOME pixels is $320 \times 40 \text{ km}^2$. However, in the validation phase the pixel size was $80 \times 40 \text{ km}^2$, and since June 1997 the pixel size is $80 \times 40 \text{ km}^2$ for three days per month. GOME is sensitive to the polarization of the light. To be able to correct for the polarization sensitivity, the polarization of the TOA radiance is measured by so-called Polarization Measuring Devices (PMDs). For calibration purposes, GOME is observing the Sun via a diffuser plate once per day. Spectral calibration is performed using an on board spectral line lamp.

Aerosol retrieval is best possible over surfaces with low and preferably constant albedo. Herman et al. [1997] showed that between 0.340 to 0.380 μm the albedo of most land surfaces is between 0.02 and 0.04, and nearly independent of the wavelength. The smooth variation of the aerosol optical properties over a wavelength range can usually be described by a few parameters [Tanré et al., 1996]. Therefore, using numerous wavelengths will add little information. For this reason, five wavelength bands at effective wavelengths of 0.342, 0.355, 0.368, 0.388, 0.400 μm with widths of 1 nm were selected from the GOME spectra. These wavelength bands were selected for their minimum in gaseous absorption and to avoid the so-called ring effect in solar Fraunhofer lines. In the absence of clouds, the TOA reflection of a cloud-free and vertically homogeneous atmosphere overlying a Lambertian surface with albedo R_s can be written as [Chandrasekhar, 1950]:

$$\rho(\lambda) = \rho_a(\lambda) + \frac{R_s(\lambda)}{1 - R_s(\lambda) \cdot s(\lambda)} T(\lambda), \quad (6.8)$$

where the same notation as in equation (6.2) is used.

To separate the atmospheric and surface contributions to the TOA reflectance, an assumption on the surface albedo, R_s , is made. The aerosol is assumed to be an external mixture of the anthropogenic and marine aerosol type. The TOA reflectance for different aerosol mixtures and AOD are computed from the lookup tables using equation (6.8). To find the best-fitting combination of mixture and AOD the method of least-squares is applied, thus minimizing ε^2 , which is defined as:

$$\varepsilon^2 = \sum_i [\rho(\lambda_i) - \rho_m(\lambda_i)]^2, \quad (6.9)$$

where: ρ is the computed reflectance for a given aerosol model and AOD; and ρ_m is the measured TOA reflectance; and λ_i is the wavelength of the i -th wavelength band.

The largest errors in this retrieval method are expected to be caused by the assumptions on the aerosol size distribution and the chemical composition, and the assumed surface albedo. An error analysis was performed to investigate the sensitivity of the method to these assumptions. Data was simulated for different surface albedos and aerosol models using the 6S model [Tanré et al., 1997], for the geometry encountered in the case study described below. The simulated data set was created for the aerosol models 'Urban', 'Maritime' and 'Continental', as proposed by WMO [1983]. To test the surface albedo sensitivity, the surface albedo was varied while the same aerosol model was used as in the lookup tables. The simulated data set was used as input for the retrieval algorithm, and the retrieved AODs were compared to the 'true' values. The most important conclusions of this error analysis are:

- The retrieval method is sensitive to absorption by the aerosol. For strongly absorbing aerosols (WMO Urban model, single scattering albedo as low as 0.66) the retrieval algorithm tends to negative values for the AOD. The absorption sensitivity is caused by the weak absorption of the aerosol model used to compute the lookup tables. Strongly absorbing aerosols will absorb part of the important Rayleigh and surface contributions, which will lead to under-estimations, or even negative values, for the retrieved AOD.

- For the WMO Maritime and WMO Continental models the difference between the retrieved and 'true' AOD was between 1 and 34 %.

- For land surfaces (albedo 0.02 - 0.04) the assumed surface albedo should be within 0.01 of the 'true' value to ensure that the retrieved AOD is within 0.1 of the 'true' value.

The overall uncertainty of the retrieval method depends on the accuracy of the assumed aerosol model and surface albedo. When the surface albedo is within 0.01 of the 'true' value, the uncertainty of the AOD retrieval is estimated 30% or 0.1, whichever is greatest.

6.2.5 Cloud detection in ATSR-2 images

The operational ATSR-2 cloud flagging product is developed for sea surface temperature retrieval, and cannot be used over land. Therefore, we developed a cloud detection algorithm for ATSR-2 data which can be used both over land and ocean. The cloud detection algorithm is based on the APOLLO algorithm, which was developed for cloud detection in AVHRR images [Olesen and Grassl, 1985, Saunders and Kriebel, 1988]. A sequence of cloud detection tests is applied to all pixels in the ATSR-2 image. Pixels are flagged cloudy if the reflectivity at 0.66 μm , the color ratio (0.87/0.66 μm), the brightness temperature at 11 μm , or the brightness temperature difference (11-12 μm) exceed specified thresholds. The thresholds are determined from the data itself by histogram analysis. Different thresholds are used over land and sea. The cloud detection results in a classification of all pixels in clear and cloudy pixels.

6.3 Observational Data

On 25 July 1995, the ERS-2 satellite passed over northwestern Europe at 1050 UTC. The ATSR-2 1.6 μm image is shown in Figure 6.1a, together with the ground tracks of the eastern and nadir pixels of GOME. The 25th of July 1995 was in the commissioning and validation phase of GOME, during which the pixel size was set to $80 \times 40 \text{ km}^2$. The satellite retrievals will be compared to ground-based measurements at three locations indicated in Figure 6.1a. In Petten, The Netherlands (52.75° N , 4.65° E) and De Bilt, The Netherlands (52.10° N , 5.18° E) the direct solar irradiance was measured with pyrhelimeters. The mid-visible AOD can be derived from the direct solar irradiance when data on the amount of precipitable water is available [Halthore et al., 1997]. The latter was derived from the radiosonde from De Bilt at 1200 UTC. The direct solar irradiance in the UV ($0.368 \mu\text{m}$) was measured in De Bilt with a UV-A pyrhelimeter. The AOD at this wavelength was derived in the morning (between 0505 and 0720 UTC) and afternoon (between 1610 1825 UTC) using the Langley plot method. In Lille, France (50.60° N , 3.15° E) the spectral AOD was determined using a Sun/sky radiometer of the AERONET network [Holben et al., 1998].

6.4 Results

6.4.1 ATSR-2 retrieval

Figure 6.1a shows very few clouds over northwestern Europe for 25 July 1995. The cloud flagging method described in section 6.2.5 indicated some sub-pixel cloudiness in the southern part and northeastern part of the image. The area over The Netherlands, Belgium and northern France above about 50° N was cloud-free. The dual-view algorithm was applied to the ATSR-2 data. The AOD at $0.555 \mu\text{m}$ retrieved from the ATSR-2 data is shown in Figure 6.1b. This image shows a large aerosol plume over Germany, Belgium and northern France. The AOD at $0.555 \mu\text{m}$ in this plume reaches values larger than 0.5, whereas to the north of the plume the AOD is smaller than 0.15. Over less than 100 km the AOD changes by more than a factor of 3, clearly demonstrating the large spatial variability of the aerosol. The AOD image shows some artifacts over shallow water bodies. Apparently the k -factor approximation (equation (6.3)), which was developed for use over land surfaces, is not valid for these areas. The higher AODs in the area around (51.5° N , 9° E) are an artifact caused by the occurrence of sub-pixel clouds in this area.

To validate the satellite retrieval, the dual-view algorithm results were compared to the results of ground-based aerosol measurements. In Figure 6.2a the AOD retrieved from the ATSR-2 data and the AOD computed from the Sun/sky radiometer direct solar irradiance measurements at Lille are plotted as a function of the wavelength. Unfortunately, the Sun/sky radiometer data and the ATSR-2 data are not available at the same wavelengths. However, it is reasonable to assume a smooth spectral variation of the AOD, and thus the data points from

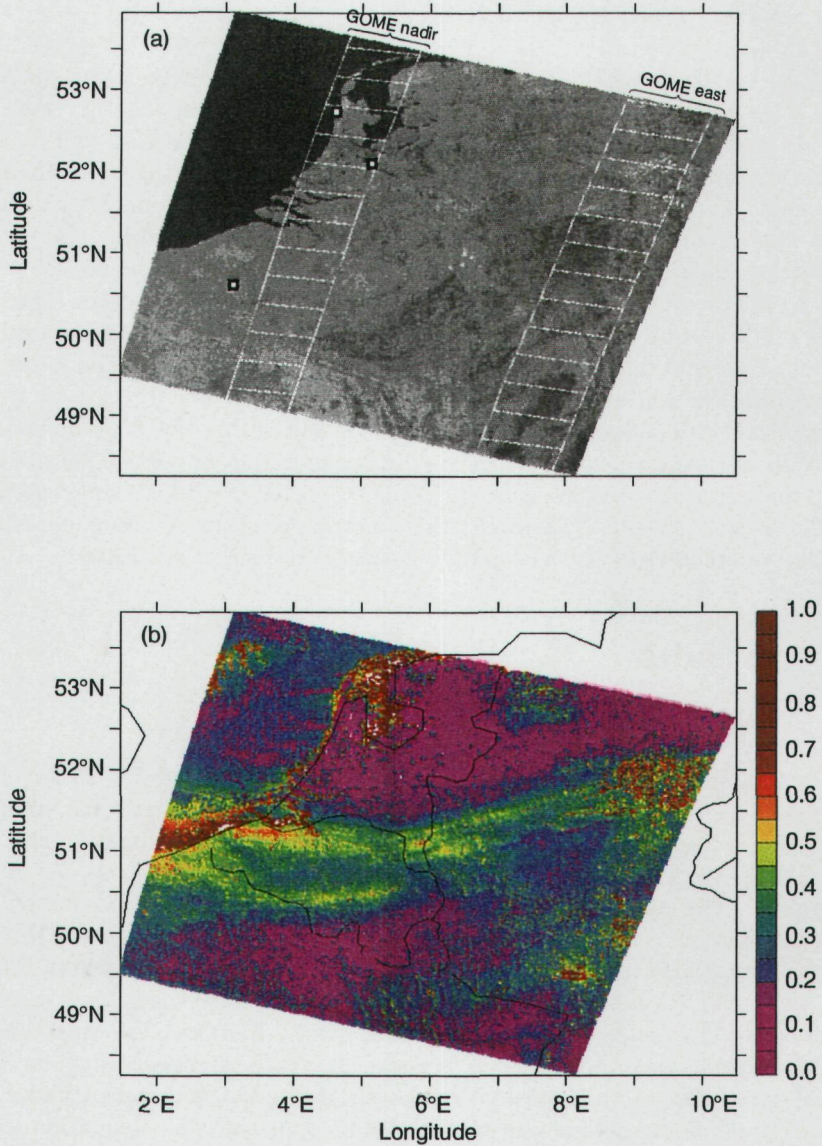


Figure 6.1: (a) ATSR-2 near infrared ($1.6 \mu\text{m}$) image over northwestern Europe for 25 July 1995, 1050 UTC. Squares indicate the location of the ground stations at Petten (52.75°N , 4.65°E), De Bilt (52.10°N , 5.18°E) and Lille (50.60°N , 3.15°E). Lines indicate the GOME pixels for the nadir and east tracks. (b) Distribution of the aerosol optical depth at $0.555 \mu\text{m}$ for the scene of Figure 6.1a as computed from the ATSR-2 data using the dual view algorithm.

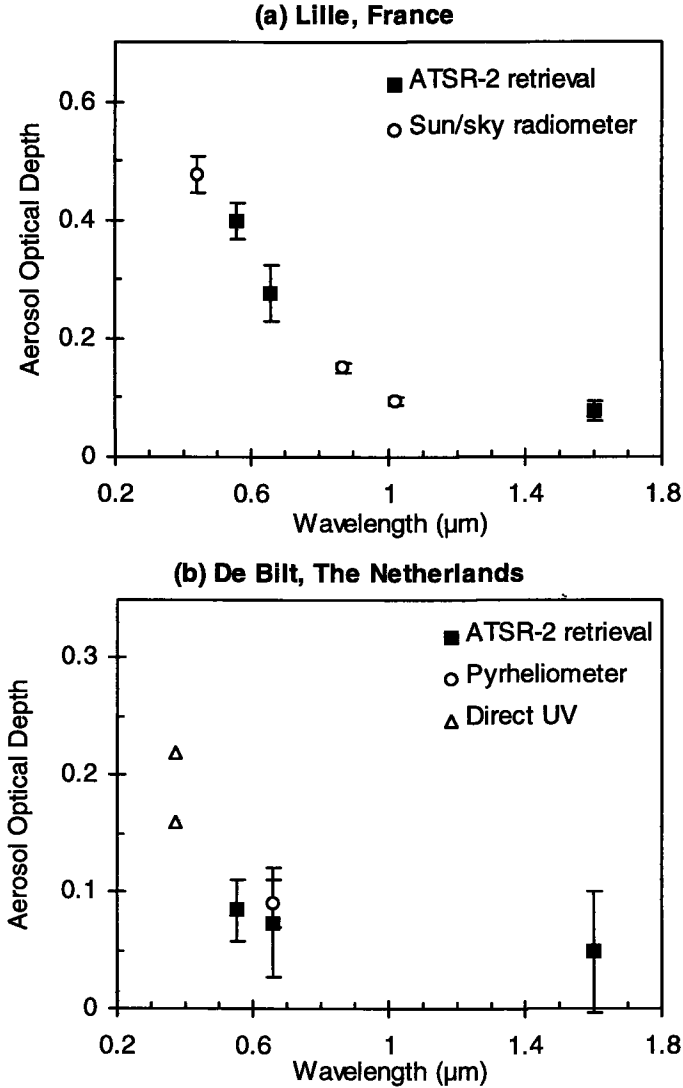


Figure 6.2: (a) Aerosol optical depth for Lille for 25 July 1995, 1050 UTC, plotted as function of the wavelength. Squares for the satellite retrieval from ATSR-2 data using the dual view algorithm; open circles for the Sun/sky radiometer data; errorbars indicate the standard deviation in the measurements. (b) Aerosol optical depth for De Bilt for 25 July 1995, plotted as a function of the wavelength. Squares for the satellite retrieval from ATSR-2, open circles for the broadband pyrheliometer results, and triangles for the UV direct solar irradiance results.

each method can be interpolated. Application of this procedure shows that the ATSR-2 and Sun/sky radiometer data agree within 0.05 optical depth. From the direct solar irradiance measured by the pyrhemeters in Petten and De Bilt, the AOD at $0.659 \mu\text{m}$ was computed using MODTRAN 3.5 computations. In De Bilt the AOD at $0.659 \mu\text{m}$ was 0.09 ± 0.02 ; and in Petten the AOD at $0.659 \mu\text{m}$ was 0.12 ± 0.02 . The AOD at $0.659 \mu\text{m}$ from the dual view retrieval was 0.07 ± 0.05 in De Bilt and 0.09 ± 0.05 in Petten. Thus the values for the AOD derived from ATSR-2 and from the ground based pyrhemeter measurements are within the experimental uncertainty. Also the spatial variations show a similar trend. The AOD at $0.368 \mu\text{m}$, derived from Langley plots for the UV direct solar irradiance measurements in De Bilt, was 0.16 and 0.22 for the morning and the afternoon, respectively. These values are in agreement with the low AOD values from the ATSR-2 and pyrhemeter measurements in De Bilt. The AOD from the ATSR-2 retrieval for De Bilt, as function of the wavelength, is plotted in Figure 6.2b, together with the ground-based results described above. The AOD from the UV measurements seems to be higher than the ATSR-2 retrieval and the pyrhemeter results. However, the difference in wavelength and time between make comparison difficult.

6.4.2 GOME retrieval

surface albedo results

The ground tracks of the nadir and the east pixels of GOME are shown in Figure 6.1a. The ground stations are nearest to, or covered by, the nadir GOME pixels. Therefore we will focus on the nadir GOME pixels, which were cloud-free. To compare GOME and ATSR-2 data, the ATSR-2 retrieved AOD values were averaged over the GOME pixels. In Figure 6.3 the TOA reflectance at two wavelengths, as measured by GOME, is plotted as a function of the AOD as retrieved from the ATSR-2 data. In the UV ($0.368 \mu\text{m}$, Figure 6.3a) there is a clear linear relationship between the TOA reflectance and the AOD from ATSR-2. In the visible ($0.680 \mu\text{m}$, Figure 6.3b) such a relationship is absent, due to the non-negligible spatial variations of the surface albedo. In the UV the surface albedo is much lower and far more constant. Using radiative transfer calculations and the y-axis intercept of Figure 6.3a, the surface albedo at $0.368 \mu\text{m}$ was estimated to be 0.013 ± 0.005 . The same analysis was performed to determine the surface albedo at the other wavelengths used in the GOME retrieval algorithm. The surface albedo for all the wavelengths is shown in Table 6.2.

The surface albedos listed in Table 6.2 are slightly lower than those reported by Herman et al. [1997b] for land surfaces (0.02 to 0.04), however these authors did not correct for contribution by aerosols. The surface albedo shows little spectral variation, except at the lower end. At $0.342 \mu\text{m}$ the surface albedo is significantly higher than at the other wavelengths.

The slope between the TOA reflectance and the AOD is very sensitive to the aerosol phase function [Durkee et al., 1986], which in turn depends strongly on the aerosol type. The linear relationship between the TOA radiance and the

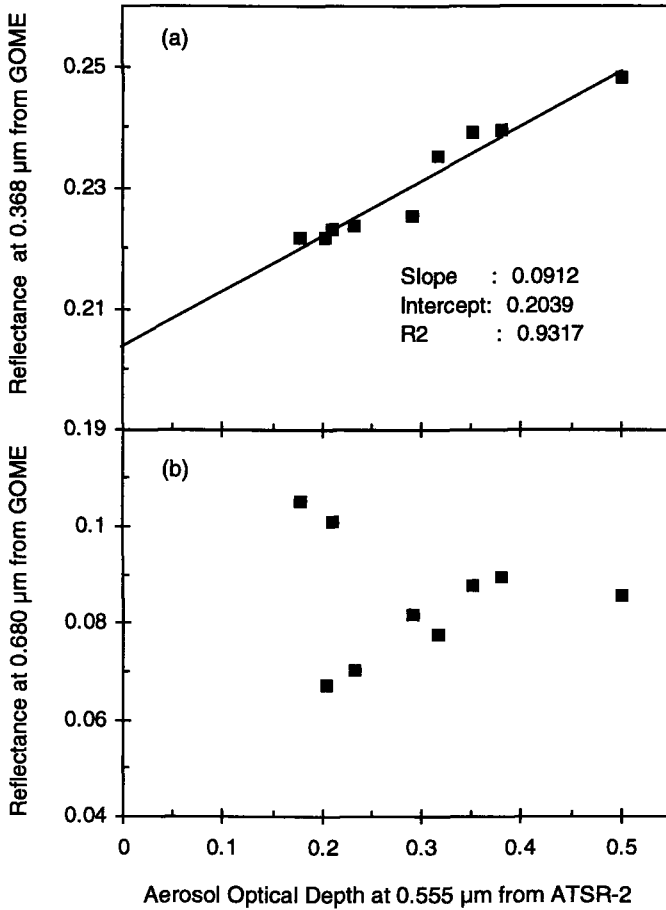


Figure 6.3: Comparison between the reflectance as measured by GOME and the aerosol optical depth as retrieved from ATSR-2. In Figure 6.3a the reflectance at 0.360 μm is plotted as a function of the aerosol optical depth at 0.555 μm ; in Figure 6.3b the reflectance at 0.680 μm is plotted as a function of the aerosol optical depth at 0.555 μm .

AOD, as observed in Figure 6.3a, indicates that the phase function does not vary strongly over this region. The UV aerosol algorithm was applied to the GOME data, using the surface albedos as listed in Table 6.2.

Wavelength (μm)	Surface Albedo
0.342	0.024 ± 0.005
0.355	0.015 ± 0.005
0.368	0.013 ± 0.005
0.388	0.011 ± 0.005
0.400	0.011 ± 0.004

Table 6.2: UV Surface albedo determined from the GOME nadir reflectances and ATSR-2 AODs between 49.4 and 53.3° N.

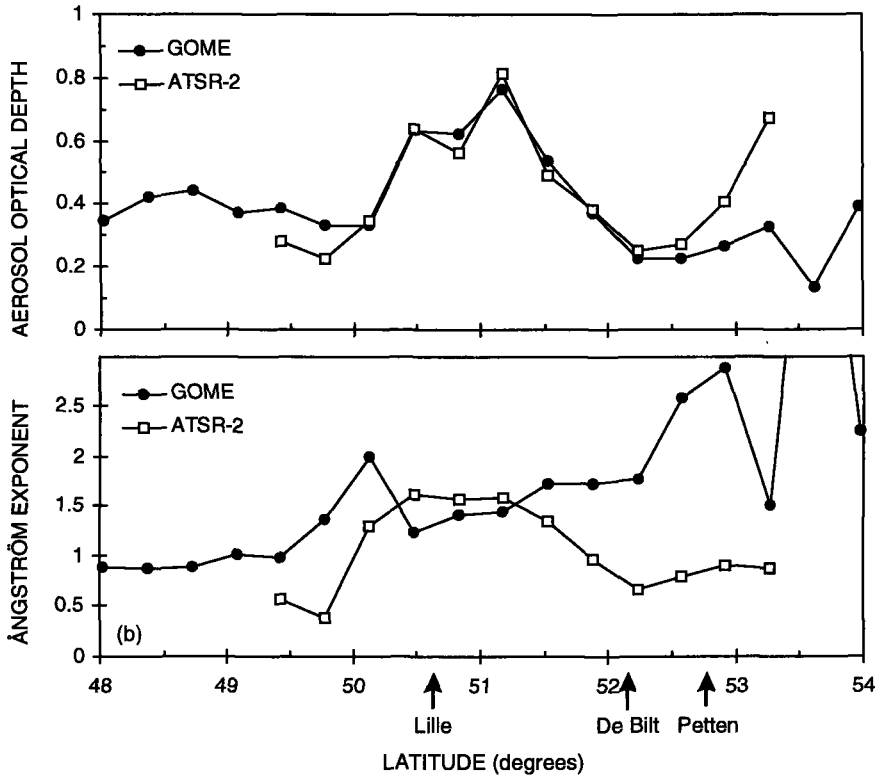


Figure 6.4: (a) Aerosol optical depth at 0.400 μm as determined from the GOME and ATSR-2 data plotted as a function of latitude for the nadir track of GOME, see Figure 6.1a. (b) Same as (a) but for the Ångström wavelength exponent.

aerosol optical depth results

The AOD can often be well represented by a power-law function:

$$AOD(\lambda) \sim \lambda^{-\alpha} \quad (6.10)$$

where α is the Ångström wavelength exponent; and λ is the wavelength in μm . Such a power law fit was used to convert the ATSR-2 data to $0.400 \mu\text{m}$, in order to compare the ATSR-2 and GOME retrieval results. Figure 6.4a shows the GOME AOD and the ATSR-2 AOD, both for a wavelength of $0.400 \mu\text{m}$, plotted as function of latitude. The AODs from the two retrieval methods agree within 0.1, except for latitudes larger than about 52.5°N . In this region with shallow waters the ATSR-2 retrieval is unreliable, as discussed above. In Figure 6.4b the Ångström wavelength exponent as determined from the GOME and ATSR-2 data is plotted as a function of the latitude. For the ATSR-2 the AOD (Figure 6.4a) and Ångström wavelength exponent (Figure 6.4b) correlate very well. This good correlation shows that there are more and smaller particles inside the plume than outside the plume. However, the Ångström wavelength exponent determined from the GOME data does not show this correlation. The GOME Ångström wavelength exponent shows much more variation than the ATSR-2 values, which is probably caused by the small wavelength range ($0.342 - 0.400 \mu\text{m}$) used in the GOME retrieval.

A further comparison between GOME and ATSR-2 aerosol retrieval is presented in Figure 6.5. Figure 6.5a shows the AOD retrieved from the GOME pixel including De Bilt, and the ATSR-2 AOD averaged over this GOME pixel, both as a function of wavelength. Figure 6.5b is similar to 5a, but for the GOME pixel nearest to Lille. Combining the information from the two aerosol retrieval methods yields information on the AOD and its spectral behavior from the UV to the near-infrared. Therefore, power-law fits through the combined GOME and ATSR-2 data were computed, which are plotted in Figure 6.5a and 6.5b. For the De Bilt pixel the Ångström wavelength exponent from the power-law fit is 0.7 ± 0.1 , for the pixel near Lille it is 1.6 ± 0.1 . The latter is in good agreement with an Ångström wavelength exponent of 1.8 ± 0.2 from the Sun/sky radiometer in Lille. Note that the Sun/sky radiometer is a point measurement whereas the GOME pixel covers a $80 \times 40 \text{ km}^2$ area.

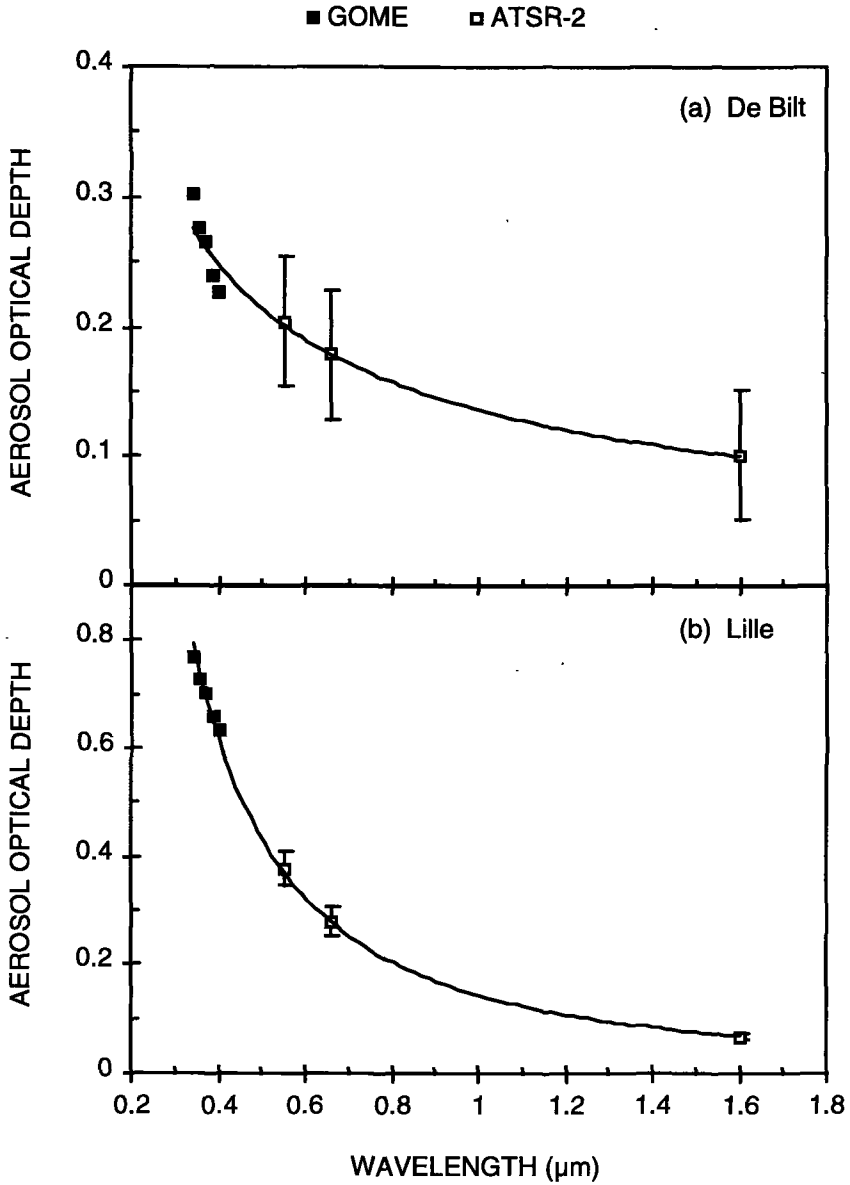


Figure 6.5: Aerosol optical depth versus wavelength for the GOME pixel covering De Bilt (figure 6.5a), and for the GOME pixel nearest to Lille (Figure 6.5b). Lines are power-law fits through the combined ATSR-2 and GOME aerosol optical depths.

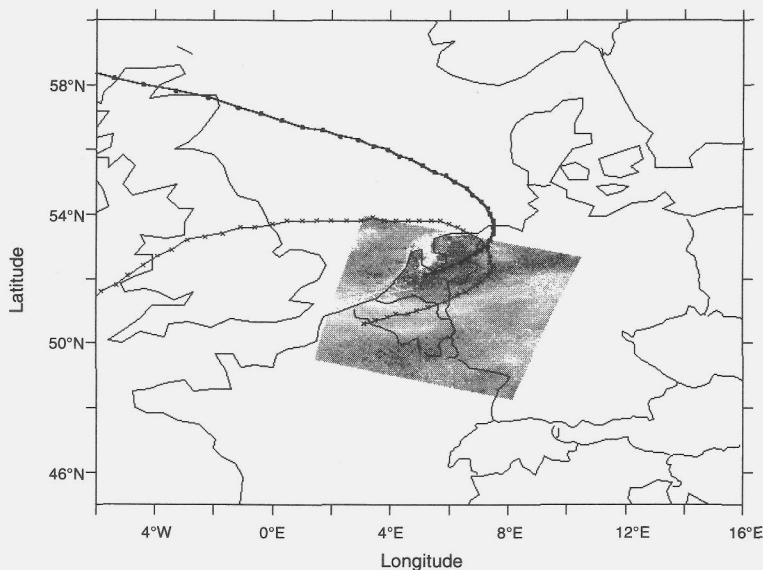


Figure 6.6: Back-trajectories for airmasses reaching De Bilt and Lille on 25 July 1995, 1100 UTC, overlaid on the aerosol optical depth image (Figure 6.1b). Each symbol (dot for De Bilt, cross for Lille) on the back-trajectory represents one hour; the back-trajectories end at a height of about 150 m.

6.4.3 Back-Trajectories

In the previous sections, data were presented of aerosol properties determined from satellite measurements and ground based observations. The image constructed from the ATSR-2 data shows a large aerosol plume over Germany, Belgium and northern France (Figure 6.1b). The occurrence of this plume and the large aerosol gradient was confirmed by ground based measurements and by GOME retrievals. Also, combination of GOME and ATSR-2 retrievals showed a higher Ångström wavelength exponent in Lille. These two facts together indicate that in this case of 25 July 1995, the particles dominating the scattering are smaller in Lille than in De Bilt. The regional distribution of aerosols is caused by both transport and local sources. To investigate this in detail, the airmass history for De Bilt and Lille were determined. The back-trajectories for De Bilt and Lille are shown in Figure 6.6. The time interval between each point in Figure 6.6 is one hour. Both back-trajectories end at an altitude of approximately 150 m. Over the last 4 days the back-trajectory for De Bilt was between 900 and 150 m height, and for Lille between 400 and 150 m. The airmass that ends at De Bilt, which is north of the aerosol plume, has passed over Scotland, the North Sea and the mainly rural northeastern part of The Netherlands. The airmass ending in Lille (in the aerosol plume) has followed a more southerly route, passing over some industrial regions in the UK, and particularly over the

industrial and densely populated areas in the German Ruhr area. Therefore it is most probable that the aerosol plume was mainly due to anthropogenic sources in Germany and Belgium.

6.5 Summary and Conclusions

Aerosol optical depths retrieved over land from GOME and ATSR-2, two satellite instruments on the ERS-2 satellite, are compared for a case study over north-western Europe for 25 July 1995. The retrieval methods differ in the wavelength ranges to which they apply, in the viewing directions used and the assumptions on the surface reflection. First, results from the ATSR-2 dual-view algorithm were compared to ground based observations at three locations. The AOD from the ATSR-2 dual view algorithm agreed within the observational uncertainty with co-located Sun/sky radiometer and pyrhelimeter derived values. To compare the two satellite aerosol retrieval methods the ATSR-2 derived AODs were averaged over the GOME pixels. Comparison of the AODs at $0.400 \mu\text{m}$ showed that for most of the pixels the two methods agreed within 0.1 optical depth. The Ångström wavelength exponent compared less good, which is probably due to the small wavelength range used in the GOME retrieval (0.342 to $0.400 \mu\text{m}$). By combining the two retrieval methods, aerosol properties from the UV to the near infrared can be retrieved from the same satellite platform. The regional aerosol distribution for 25 July 1995 shows a large aerosol plume over Belgium and northern France. Back-trajectories indicate that this plume was formed by anthropogenic sources in the Germany and Belgium. The large aerosol gradient illustrates the high spatial variability of the aerosol in the troposphere.

6.6 Acknowledgments

This work is supported by the Netherlands Space Research Organization (SRON), under contract EO-008. The ATSR-2 and GOME data were kindly provided by the European Space Agency (ESA) through DLR and ESRIN. The authors would like to thank Dr. D. Tanré from the Laboratoire d'Optique Atmosphérique (LOA), Université de Lille, for the Sun/sky radiometer data, Arjan Hensen from the Netherlands Energy Research Foundation (ECN) for the pyrhelimeter data, and Rinus Scheele from the Royal Netherlands Meteorological Institute (KNMI) for the trajectory calculations. The Ferret analysis package, developed by NOAA PMEL, was used in the preparation of this work (available at <http://ferret.wrc.noaa.gov/>).

Bibliography

Chandrasekhar, S. (1950). *Radiative Transfer*. Oxford University Press, London.

- Charlson, R. J., Schwartz, S. E., Hales, J. M., Cess, R. D., Coackley, J. A. J., Hansen, J. E., and Hofmann, D. J. (1992). Climate forcing by anthropogenic aerosols. *Science*, 255:423–430.
- De Rooij, W. A. and Van der Stap, C. C. A. H. (1984). Expansion of mie scattering in generalized spherical functions. *Astron. Astrophys.*, 131:237–248.
- Durkee, P. A., Jensen, D. R., Hindman, E. E., and VonderHaar, T. H. (1986). The relationship between marine aerosols and satellite detected radiance. *J. Geophys. Res.*, 91:4063–4072.
- Evans, K. F. and Stephens, G. L. (1991). A new polarized atmospheric radiative transfer model. *J. Quant. Spec. Rad. Trans.*, 40:413–423.
- Flowerdew, R. and Haigh, J. (1995). An approximation to improve accuracy in the derivation of surface reflectances from multi-look satellite radiometers. *Geophys. Res. Lett.*, 22:1693–1696.
- Gathman, S. G. and Davidson, K. L. (1993). The navy oceanic vertical aerosol model. Technical report, NRAD, San Diego, Calif.
- Gathman, S. G., de Leeuw, G., Davidson, K. L., and D., J. (1989). The naval oceanic vertical aerosol model: Progress report. In *AGARD 45th symposium of the Electromagnetic Wave Propagation Panel on Atmospheric propagation in the UV, visible, IR and mm-wave region and related systems aspects*, Copenhagen, Denmark.
- Halthore, R., Schwartz, S., Michalsky, J., Anderson, G., Ferrare, R., Holben, B., and Ten Brink, H. M. (1997). Comparison of model estimated and measured direct-normal solar irradiance. *J. Geophys. Res.*, pages 29991–30002.
- Hegg, D. A., Livingston, J., Hobbs, P. V., Novakov, T., and Russell, P. B. (1997). Chemical apportionment of aerosol column optical depth off the mid-atlantic coast of the united states. *J. Geophys. Res.*, 102:25293–25303.
- Herman, J. R., Bhartia, P. K., Torres, O., Hsu, C., Sefstor, C., and Celarier, E. (1997). Global distributions of uv-absorbing aerosols from nimbus 7/toms data. *J. Geophys. Res.*, 102:16,911–16,922.
- Herman, J. R. and Celarier, E. A. (1997). Earth surface reflectivity climatology at 340-380 nm from toms data. *J. Geophys. Res.*, 102:28,003–28,011.
- Holben, B., Eck, T., Slutsker, I., Tanré, D., Buis, J., Setzer, A., Vermote, E., Reagan, J., Kaufman, Y., Nakajima, T., Lavenu, F., Jankowiak, I., and Smirnov, A. (1998). Aeronet- a federated instrument network and data archive for aerosol characterization. *Remote Sens. Environ.*, 66:1–16.
- IPCC (1995). Radiative forcing of climate. In Houghton, J., Filho, L. G. M., Bruce, J., Lee, H., Haites, E., Harris, N., and Maskell, K., editors, *Climate change 1994*, pages 1–231. Cambridge UP, Cambridge.
- Kaufman, Y. J., Tanre, D., Nakajima, T., Lenoble, J., Frouin, R., Grassl, H., Herman, B. M., King, M. D., and Teillet, P. M. (1997a). Passive remote sensing of tropospheric aerosol and atmospheric correction for the aerosol effect. *J. Geophys. Res.*, 102:16,815–16,830.

- Kaufman, Y. J., Wald, A. E., Remer, L. A., Gao, B. C., Li, R. R., and Flynn, L. (1997b). The modis 2.1 μm channel correlation with visible reflectances for use in remote sensing of aerosol. *IEEE Trans. on Geosci. and Remote Sens.*, 35:1286–1298.
- Olesen, F. and Grassl, H. (1985). , cloud detection and classification over oceans at night with NOAA-7. *Int. J. Remote Sens.*, 6:1435–1444.
- Saunders, R. and Kriebel, K. (1988). An improved method for detecting clear sky and cloudy radiances from AVHRR data. *Int. J. Remote Sens.*, 9:123–150.
- Stamnes, K., Tsay, S., Wiscombe, W., and Jayaweera, K. (1988). Numerically stable algorithm for discrete-ordinate-method radiative transfer in multiple scattering and emitting layered media. *Appl. Opt.*, 27:2502–2509.
- Tanré, Deuzé, J. L. H. M., and Morcette, J. J. (1997). Second simulation of the satellite signal in the solar spectrum, 6s: an overview. *IEEE trans. on Geosci. and Rem. Sensing*, 35:675–686.
- Tanré, D., Herman, M., and Kaufman, Y. J. (1996). Information on aerosol size distribution contained in solar reflected radiances. *J. Geophys. Res.*, 101:19,043–19060.
- ten Brink, H. M., Veefkind, J. P., Waaijers-IJpelaan, A., and van der Hage, J. C. H. (1996). Aerosol light-scattering in the netherlands. *Atmos. Environ.*, 30:4251–4261.
- WMO (1983). Cas/radiation commission of iamap meeting of experts on aerosols and their climatic effects. Technical report, WMO, Williamsburg, Vi.

Chapter 7

Comparison of Aerosol Satellite Remote Sensing and a 3D chemical transport Model

The model calculations presented in this chapter were performed by Ad Jeuken. He developed this model in co-operation with Frank Dentener.

Abstract

Comparisons are presented between aerosol optical depth derived from aerosol satellite remote sensing and from aerosol fields calculated with a 3D chemical transport model, for Europe for August 1997. The 3D chemical transport model describes the sulfur cycle coupled with methane oxidation and tropospheric background chemistry. The satellite retrieval is based on GOME data in the wavelength range between 0.340 and 0.400 μm . To independently test the model and the retrieval, results are compared to ground-based sunphotometer data. The correlation coefficient between GOME retrieved aerosol optical depth and sunphotometer data is 0.80. For the model derived aerosol optical depth and sunphotometer data the correlation is much less. However, this low value is biased by a few days for which the model predictions differ strongly from the measurements. For two periods of three days each, spatial correlation between model and GOME data was evaluated. The mean absolute difference between the model and GOME aerosol optical depth was 0.23. The model data shows a positive offset of approximately 0.2. This offset might be due to an excess of sulfate predicted by the model in the free-troposphere.

7.1 Introduction

Aerosols are important for a variety of processes in the atmosphere. Three-dimensional (3D) chemical transport models are being developed that can accurately describe the global aerosol fields. These models can be used as diagnostic tools to predict the effects of changes in emissions and depositions on global climate. Many different aerosol species, each with its own source strength and spatial extent, add to the aerosol radiation effects [Tegen et al., 1997]. In addition, the radiative forcing of aerosols does not only depend on the concentration, but also on the aerosol size distribution, particle shape and chemical composition. Owing to their relatively short lifetimes in the troposphere, the aerosol properties are highly non-uniformly distributed, in both space and time.

To test 3D chemical transport models, their results must be compared with experimental data. Ground-based, airborne, and satellite measurements can be used. Ground-based experiments can provide detailed information on the aerosol size distribution and chemical composition. However, most of these measurements are point measurements near the surface, and may not be representative for the aerosol throughout the boundary layer and above. Aircraft observations are very expensive and therefore not suitable for long term monitoring. Satellite remote sensing on the other hand can provide daily measurements of column integrated aerosol properties, such as the spectral aerosol optical depth (AOD), on spatial scales ranging from a few kilometers to global. The spectral AOD holds information on the aerosol load and on the aerosol size distribution [Tanré et al., 1996], and limited information can be derived on the chemical composition. The drawback of satellite remote sensing measurements are the lack of profile information, and the relatively large time span (usually more than 24 hrs) between two successive satellite overpasses over an area.

Combination of aerosol satellite remote sensing and transport models can be applied for interpretation of observed spatial aerosol distributions, as observed from the satellite, and vice versa. Also, combination of remote sensing and transport models should be considered for data assimilation [Jeuken et al., 1999]. In data assimilation the satellite measured aerosols fields are used as input for the transport models which then provide “smart” interpolations to fill the (spatial and temporal) gaps between satellite overpasses. Data assimilation can be used to predict the evolution of the aerosol field. This information can be used as a first guess for the aerosol retrieval algorithms for the next overpass.

In this chapter some of the above ideas are tested by combining data from aerosol satellite remote sensing with calculations from a 3D chemical transport model. The comparison is made for a scenario over Europe, for August 1997. The 3D chemical transport model describes the sulfur cycle, from which the total AOD is estimated. To account for other aerosols than sulfate, such as nitrate and organic aerosols, a correction factor is applied based on ground-based measurements [ten Brink et al., 1996, Diederer et al., 1985]. Because sulfate aerosol is much better understood than most other aerosol species, it is used as a tracer for these other species. Like sulfate, most of the nitrate and organic aerosols are the result of anthropogenic activities. The model results are compared with

AOD retrieved from observations from the Global Ozone Monitoring Experiment (GOME) in the wavelength range between 0.340 and 0.400 μm , see chapter 6 for a description of GOME and the retrieval algorithm. Besides results from the 3D chemical transport model and satellite observations, also data is used from the AERONET sunphotometer network [Holben et al., 1998] to validate both the model and satellite retrieval results.

7.2 Modeling the Sulfur Cycle using the TM3 model

The 3D chemical transport model is developed by Jeuken and Dentener. In this section a brief description of the model is given, a more comprehensive description can be obtained from Jeuken [1999].

The tracer transport model (TM3) calculates the horizontal and vertical transport of tracer mass using meteorological fields from the ECMWF. Global fields of wind, surface pressure, temperature, humidity, cloud cover, cloud liquid/ice water, surface precipitation and several other surface parameters are available. The ECMWF input fields are updated every six hours. A spatial resolution of $2.5^\circ \times 2.5^\circ$ is used for TM3. By computing the derivative fields, the TM3 output is on a $1.25^\circ \times 1.25^\circ$ grid.

The sulfur species in TM3 are SO_2 , SO_4^- , DMS, and MSA. The sulfur cycle is coupled to a tropospheric background chemistry scheme, which solves the $\text{CH}_4\text{-CO-NO}_x\text{-HO}_x$ chemistry [Roelofs and Lelieveld, 1995]. Emissions of SO_2 are taken from the GEIA data base. Here the two level seasonal emission distributions are used. Volcanic emissions are derived from the work of Andres and Kasgnoc [1998]. For DMS the compilation of ocean surface concentrations of Kettle and Andreae is used, in combination with the Liss and Merlivat [1986] exchange coefficient parametrization to calculate DMS emissions. The total global SO_2 emission is about 75 Tg per year.

Both gas phase and in-cloud reactions of SO_2 are considered. About 36% is oxidized by OH in the gas phase, the rest by H_2O_2 and O_3 in the cloud resulting in the formation of sulfate. The removal path via ozone is strongly pH dependent. The pH is calculated from all bases, weak and strong acids, that are available in the model (also ammonium). To determine the amount of dissolved SO_2 in the cloud droplet, the effective Henry equilibrium coefficient is calculated.

The main removal mechanism of sulfate is wet scavenging either by rain drops or cloud drops. The precipitation at the surface is scaled with a normalized zonally and seasonally average climatology of the vertical distribution of precipitation formation. The resulting vertical distribution of precipitation formation rates is directly related to the amount of tracer being scavenged inside the cloud [Langner and Rodhe, 1991].

Dry deposition of sulfate is calculated with a single deposition velocity obtained from a unimodal mass size distribution over land and a bimodal mass size distribution over sea.

SO₂ is removed at the surface mainly by dry deposition. Dry deposition of all tracers in the model is calculated with the extensive scheme of Ganzeveld et al. [1998]. In this scheme the deposition velocity of SO₂ depends on the aerodynamic resistance and surface characteristics like for example soil pH, soil wetness or snow cover. The deposition over sea is dependent on the surface roughness which varies with wind speed.

7.3. Modeling the Aerosol Optical Depth

The TM3 model provides the spatial and temporal distribution of the mass of sulfate ions. In TM3 an effective aerosol size distribution is used. To derive the AOD of the sulfate aerosol, assumptions are made on the aerosol size distribution. Other aerosol species, such as nitrates and organic aerosols contribute significantly to the total AOD [ten Brink et al., 1996]. Additional assumptions have to be made to account for the contribution of these aerosol species. A complication is that the optical properties of especially organic aerosols are not well known. The approach to take this into account will be discussed below.

Following the approach of Kiehl and Briegleb [1993], the AOD is expressed as:

$$AOD(\lambda) = f(RH, \lambda) \frac{\alpha_{SO_4}(\lambda) B_{SO_4}}{\chi_{SO_4}}, \quad (7.1)$$

where:

$\alpha_{SO_4}(\lambda)$ is the mass extinction efficiency of sulfate; i.e. extinction coefficient per unit of mass SO₄⁻ at relative humidity <40%;

B_{SO_4} is the sulfate column burden;

χ_{SO_4} is the fraction of the aerosol extinction at low relative humidity caused by sulfate aerosol; and

$f(RH, \lambda)$ is the relative increase of the scattering coefficient at given RH to the scattering at low (<40%) RH.

In equation (7.1) α_{SO_4} and $f(RH)$ depend on the aerosol size distribution and chemical composition of the particles. The aerosol size distribution was assumed to be lognormal, with a geometric mean radius of 0.05 μm and a geometric standard deviation of 2.0. All sulfate aerosol was assumed to be in the form of ammonium sulfate [ten Brink et al., 1996]. The dry density of the particles was taken as 1.7 g cm⁻³. α_{SO_4} was evaluated using a Mie code. The resulting α_{SO_4} is plotted in Figure 7.1 as a function of the wavelength.

Using the above assumptions, the AOD by sulfate aerosol at low RH is calculated from the model predicted sulfate mass and the sulfate mass extinction efficiency. Besides sulfate aerosol, also nitrate, organic and also sea salt aerosols contribute significantly to the AOD over Europe. The contribution of these non-sulfate aerosol particles to the column AOD is assumed a constant fraction of the sulfate contribution. The justification for this assumption is based on good correlation between aerosol scattering measured by nephelometers and the

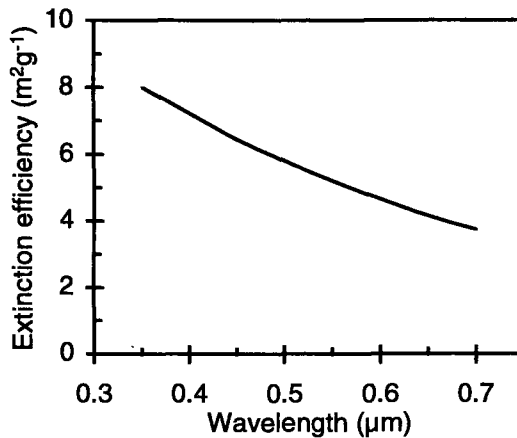


Figure 7.1: The mass extinction efficiency for dry ammonium sulfate in m^2g^{-1} SO_4^- , as a function of the wavelength. A lognormal size distribution with mean geometric radius of $0.05 \mu\text{m}$ and geometric standard deviation of 2.0 is used. The refractive index is taken as $1.53 - 0.0$.

sulfate mass [Diederer et al., 1985, ten Brink et al., 1996]. The factor χ_{SO_4} in equation (7.1) accounts for the AOD due to the non-sulfate aerosol. Very few data are available to determine a value for χ_{SO_4} . Studies in the Netherlands in the 1980s and 1990s showed that the contributions of sulfates and nitrates to aerosol scattering are comparable [Diederer et al., 1985, ten Brink et al., 1996]. Large parts of the fine particle mass could not be identified, and were presumed to be carbonaceous material. Ten Brink et al. [1996] speculated that the contribution of sulfate to particle scattering was between 30 and 40%. Diederer et al. found that sulfate scattering contributed 38% to the total aerosol extinction. Based on these studies, the sulfate contribution to the AOD at low RH is estimated to be 40%, hence a value of 0.4 is used for χ_{SO_4} in equation (7.1). It is noted that this number is based on data from two studies conducted in the Netherlands. Elsewhere in Europe χ_{SO_4} may have a different value due to differences emissions. Therefore, the use of this factor introduces uncertainty in the modeled AOD.

Most aerosol particles absorb water vapor when exposed to increasing RH. The particle growth results in more scattering by the aerosol particles, and consequently a higher AOD. To account for the increase of aerosol extinction with increasing RH, the factor $f(\text{RH}, \lambda)$ is used in equation (7.1). This factor is the ratio between aerosol extinction at given RH to aerosol extinction at low RH (<40%). The increase of the scattering coefficient with increasing RH can be measured by humidity controlled nephelometry. Figure 7.2 shows $f(\text{RH})$ as measured in the Netherlands in November 1993, for days with a continental airmass [ten Brink et al., 1996, Veefkind et al., 1996]. A polynomial fit to the

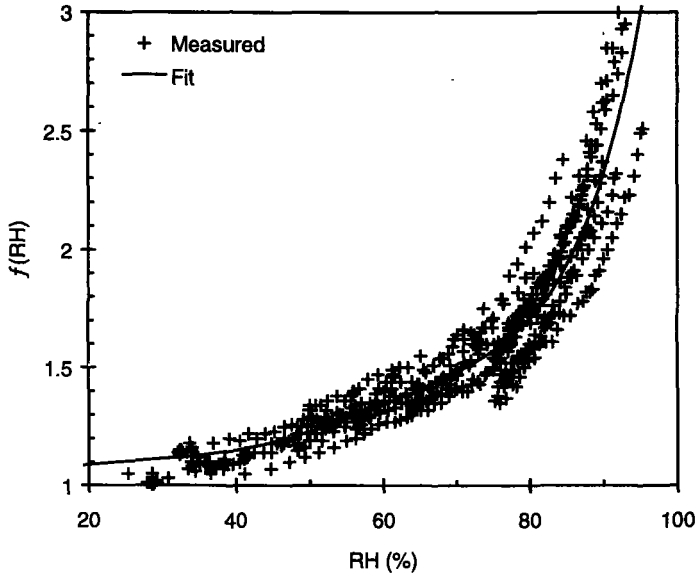


Figure 7.2: Increase of the scattering coefficient as a function of the RH, as measured using humidity controlled nephelometry. Line shows a sixth order polynomial fit through the points.

experimental data is used to describe $f(RH)$. Mie calculations showed that the wavelength dependence of $f(RH)$ can be ignored.

To compute the humidity effect on the AOD (equation (7.1), the polynomial fit shown in Figure 7.2 is used together with the RH derived from the ECWMF fields. Usually, most of the aerosol will be in the boundary layer. Therefore, the mean RH of the model boundary layer is used to compute $f(RH)$. This introduces errors when large portions of the aerosol are situated above the boundary layer. Also, due to the strong non-linear behavior of $f(RH)$, using the mean RH will always lead to an underestimation of $f(RH)$.

7.4 GOME UV Aerosol Retrieval

For aerosol satellite remote sensing the UV retrieval method described in chapter 6 was applied to GOME measurements in the wavelength range between 0.340 and 0.400 μm . In this wavelength range the surface albedo of most land surfaces is low. In chapter 6, results were presented from application of the algorithm to GOME data from the validation phase, during which the GOME pixel size was $80 \times 40 \text{ km}^2$. The retrieval results were validated using sunphotometer data and results from the ATSR-2 dual view algorithm. In this chapter GOME

data for August 1997 is used, which has the default pixel size of $320 \times 40 \text{ km}^2$. Each GOME scanline consists of three (east, nadir and west) of such pixels. The retrieval algorithm compares the measured reflectance to radiative transfer calculations. For the $320 \times 40 \text{ km}^2$ GOME pixels a single Sun/satellite geometry cannot be assumed for these calculations. Particularly for the nadir pixel, the geometry changes rapidly since the viewing azimuth angle changes rapidly in the middle of the scan line. Therefore, the GOME pixel is broken up into six sub-pixels. The reflectance of the total pixel is computed by summing the contributions of these sub-pixels.

Surface albedos as listed in Table 6.2 were used. Additionally, for sub-pixels over the sea, the Fresnel reflection of the sea surface was taken into account. The contribution by molecular (Rayleigh) scattering dominates the satellite measured radiance in the UV. Therefore, it is very important to compute the Rayleigh scattering as accurate as possible. Since the Rayleigh optical depth varies with the surface air pressure, variations in the surface air pressure should be taken into account. Daily average values for the air-pressure were taken from the NCEP/NCAR reanalysis [Kalnay and Co-authors, 1996].

The retrieval algorithm only applies to cloud-free pixels. Two cloud-screening methods were applied. The first one uses the data from the Polarization Measuring Devices (PMDs) of the GOME instrument. The PMDs are three broadband channels with a pixel size of $20 \times 40 \text{ km}^2$. A PMD-pixel is marked cloud-contaminated when the ratio between the spectral variance and the spectral average of the three PMDs exceeds a threshold value [Koppers, 1997]. As an artifact, this screening method will also flag pixels with high albedos, such as snow or ice covered surfaces. The PMD cloud-screening method fails when only a small part of the PMD pixels is covered by clouds. However, sub-pixel clouds can bias the retrieved AOD. Therefore the data was checked manually for cirrus and sub-pixel clouds using the nearest in time AVHRR visible and infrared data. Usually the AVHRR overpass is approximately three hours later than the GOME overpass.

7.5 Observational Data

For August 1997, AOD values from the TM3 model, the satellite retrieval, and ground based sunphotometers over Europe were compared. The largest wavelength used in the satellite retrieval is $0.400 \mu\text{m}$. For this reason, all comparisons are presented for this wavelength. The AOD is computed from the total sulfate column and the boundary layer RH, as described above.

Satellite retrieval was performed for all GOME data for August 1997 for the area between 35° and 75° N , and between 10° W and 30° E . In total there were 49 overpasses over this region. Due to the degradation of PMD 1, the calibration of GOME in the UV is unreliable [Tanzi et al., 1998]. The error due to this degradation was estimated between 10 and 40% for AOD between 0.2 and 1. To correct for this effect the fractional polarization for PMD 1 was increased with 10%.

Sunphotometer data from the AERONET network [Holben et al., 1998] was collected for Lille, France (50.6° N, 3.1° E), Ispra, Italy (45.8° N, 8.6° E) and Aire Adour, France (43.7° N; 0.3° E). These sunphotometers measure the direct solar radiation at 0.440, 0.670, 0.870 and 1.020 μm . The AOD at 0.400 μm was computed from the sunphotometer data by fitting a power law function through the sunphotometer derived spectral AOD. For Aire Adour and Ispra the standard cloud screened level 2 data product is used [Smirnov et al., 1999]. For Lille it was noted that the standard cloud screening was too strict. When AVHRR images indicate that it was clear over Lille, the data was still rejected by the cloud screening algorithm. Therefore, for Lille the unscreened level 1 data was used, and filtered using the following screening criteria. First, if the AOD at any of the wavelengths was missing the data was rejected. Second, if the solar zenith angle was larger than 60° the data was rejected. Third, if the AOD at 0.440 μm is larger than 0.7 and the Ångström wavelength exponent smaller than 0.7 the data was marked as cloudy and rejected.

7.6 Results and Discussion

7.6.1 Timeseries

Both the satellite retrieval and the model results were validated by comparing them to sunphotometer timeseries. It is noted that this comparison is not straightforward. The sunphotometer data is often not available at the time of the model output or at the time of the satellite overpass. The sunphotometer data show little diurnal variations, except when a change of airmass occurs during the day. Such a temporal variation at the sunphotometer site shows as spatial variations in the satellite data. The large GOME pixels tend to smooth the spatial variations. To compare the GOME data, daily averages and standard deviations for the sunphotometer data were computed. In Figure 7.3 the timeseries of the AOD at 0.400 μm is shown for Lille, Ispra and Aire Adour, for August 1997. The average, standard deviation and number of days for which data is available are listed in Table 7.1.

	Lille			Ispra			Aire Adour		
	ave	std	n	ave	std	n	ave	std	n
AERONET	0.64	0.29	24	0.59	0.28	21	0.41	0.16	15
GOME	0.67	0.29	11	0.43	0.17	5	0.48	0.10	10
Model	0.72	0.40	31	0.78	0.35	31	0.57	0.27	31

Table 7.1: Average (ave), standard deviation (std), and number of days with data (n), for the aerosol optical depth (0.400 μm) derived from AERONET sunphotometers, GOME satellite retrieval, and TM3 model, for Lille, Ispra, and Aire Adour, August 1997.

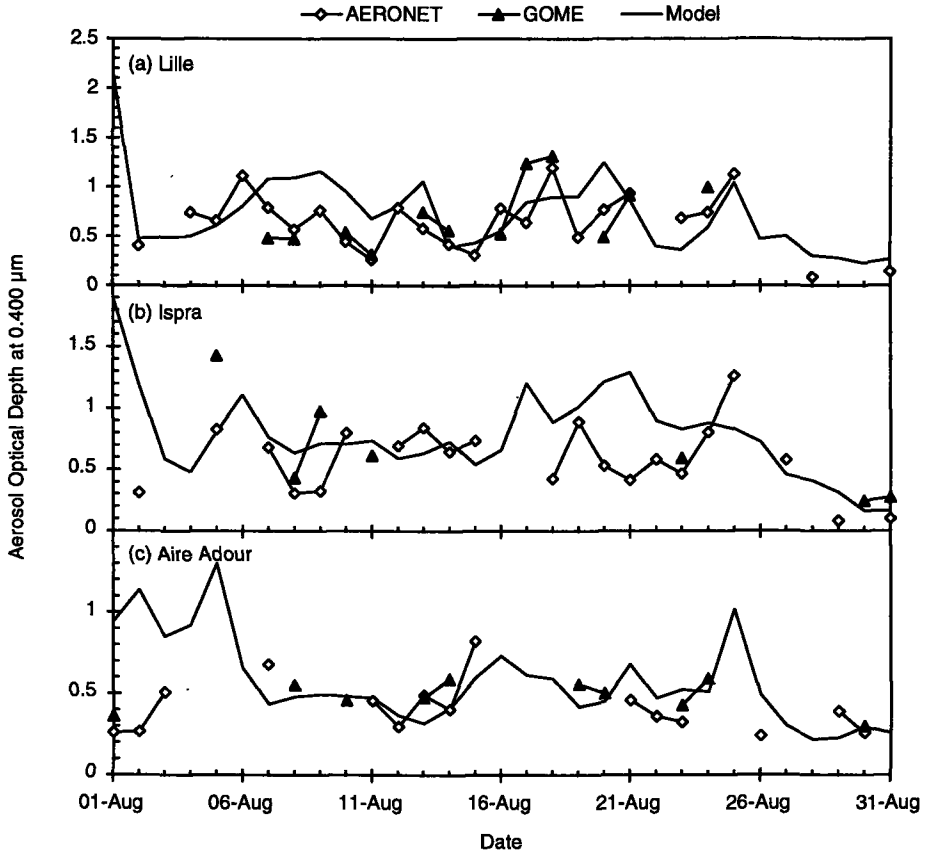


Figure 7.3: Timeseries of aerosol optical depth at $0.400 \mu\text{m}$ for August 1997, as derived from AERONET sunphotometer data, GOME satellite retrieval, and TM3 model. The AERONET data are daily averages, the GOME data are at the time of the satellite overpass (between 930 and 1130 UTC), and the TM3 model data is for 1200 UTC. For clarity the data for successive days are connected by lines. Figure 7.3a is for Lille, France; Figure 7.3b for Ispra, Italy; and Figure 7.3c for Aire Adour, France.

Due to the large pixel size ($320 \times 40 \text{ km}^2$) most of the GOME pixels are cloud contaminated, and rejected in the aerosol retrieval algorithm. For only few occasions, a cloud free GOME pixel could be identified that covered one of the AERONET sunphotometer sites. When no satellite retrieval data was available for the sites, the nearest pixel for which a valid satellite retrieval was available was used, provided that this pixel was within 200 km of the sunphotometer location. As can be seen in Table 7.1, even application of this nearest neighbor filling method provided GOME retrieval data for only about 28% of the days.

For the comparison of sunphotometer data with the GOME retrieval results, it should be realized that the sunphotometer data are daily averages at a single location, whereas the GOME data are for a large area at the time of the satellite overpass. The AOD can vary strongly over a few hundred kilometers [chapter 4, chapter 6], but also the daily variations can be large.

The timeseries in Figure 7.3 show that for Lille (Figure 7.3a) the sunphotometer and the GOME retrievals correlate well. For Ispra (Figure 7.3b) and Aire Adour (Figure 7.3c), only for few days both GOME and sunphotometer data are available. In most cases they compare reasonably well. In Figure 7.4 the GOME AOD is plotted versus the sunphotometer AOD for all three locations. The correlation for these data is 0.82. The differences between the sunphotometer data and the GOME retrieval can be explained by errors in the GOME retrieval algorithm, spatial and temporal variations in the AOD, or combinations of these effects. Although the data was carefully checked for cloud contamination, errors in the retrieval results due to unidentified sub-pixel clouds can not entirely be excluded.

The AOD from the TM3 model was computed from the model result at 1200 UTC. The data for 1200 UTC were selected as nearest to the GOME overpass over Europe is between 930 and 1130 UTC. The AOD at the sunphotometer locations was calculated by interpolating between the $1.25^\circ \times 1.25^\circ$ model output grid ($\sim 90 \times 140 \text{ km}^2$). The timeseries of the TM3 model derived AOD for the AERONET sunphotometer sites (Figure 7.3) show that the model AOD is of the same order of magnitude as the sunphotometer and GOME results. During some periods the trends in the AOD are quite similar, while for other periods they show no correlation. For example, good correlation is observed for Lille between 13 and 18 August (Figure 7.3a), and for Aire Adour (Figure 7.3c) between 11 and 15 August. An example of a period when no correlation is apparent is for Ispra (Figure 7.3b) between 20 and 25 August.

In Figure 7.5, the model AOD is plotted versus the sunphotometer derived values. In 80% of the cases the model AOD are within a factor of two of the AERONET data. The correlation is strongly biased by the data for 1 to 5 August, when in particular for Aire Adour the model overpredicts the AOD. It is noted that the model AOD is based on some very crude assumptions on the aerosol size distribution, aerosol composition and treatment of hygroscopic growth. Also, TM3 model data on large grids are compared to daily averaged point measurements. Given these crude assumptions, a factor of two seems a satisfactory result.

7.6.2 Spatial Correlation

To further evaluate the GOME AOD retrievals versus the TM3 results, spatial variations were compared for two periods: 10 to 12 August and 20 to 22 August 1997. These periods were selected because of the relatively large number of cloud-free GOME pixels. In total seven valid GOME overpasses occurred during these two periods. The orbit number, number of pixels for which aerosol retrieval was successful, and the total number of pixels, are listed in Table 7.2.

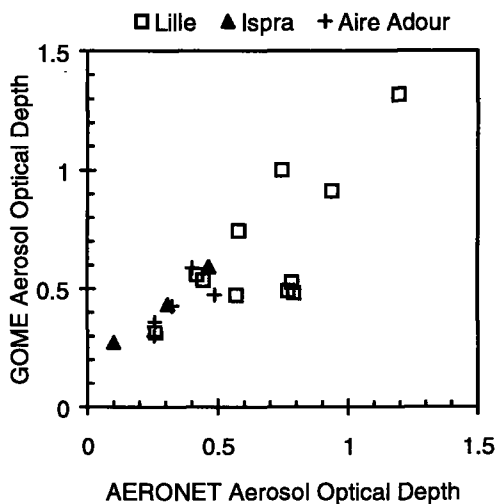


Figure 7.4: Scatterplot of aerosol optical depth at $0.400 \mu\text{m}$ from GOME satellite retrieval and derived from AERONET sunphotometer data, for Lille, Ispra, and Aire Adour, for August 1997.

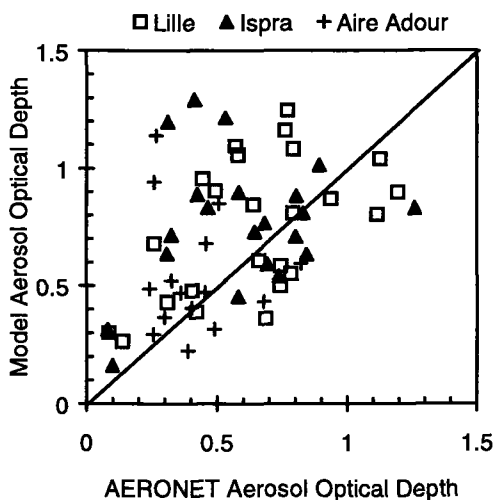


Figure 7.5: AOD at $0.400 \mu\text{m}$ derived from the TM3 model versus AERONET sunphotometer data for August 1997.

The total column burden of sulfate for 11 and 21 August, as computed by the TM3 model, are shown in Figure 7.6. The spatial distributions of sulfate aerosol on these days were strongly different. The cloud patterns are shown in the AVHRR images in Figure 7.7, showing the afternoon overpass over Europe. The role of clouds in determining the sulfate distributions is non-trivial. On one hand, sulfate is formed in clouds by the processes described in section 7.2, on the other hand, sulfate is effectively removed by precipitating clouds. For 11 August the maximum of about $60 \text{ mg m}^{-2} \text{ SO}_4^-$ was situated northwest of Scotland. The high values over the UK coincide with a cloud system coupled with a frontal zone. In-cloud oxidation can explain the high values in this region. A thunderstorm system over the Mediterranean coast of France coincides quite well with a strong gradient in the sulfate concentration. The low sulfate concentration over the eastern Mediterranean might be caused by rain out in this thunderstorm system. For 21 August the maximum was situated over the European mainland, showing values of more than $65 \text{ mg m}^{-2} \text{ SO}_4^-$. This maximum is caused by a high pressure system, with stagnant air in which pollution can build up. Over north Scandinavia more sulfate aerosol is predicted for 21 August. The low values over the UK may be explained by the large frontal zone, in which wet removal may have dominated over in-cloud formation.

The AOD image for the GOME retrieval on 11 and 21 August 1997 is shown in Figure 7.8. Due to the swath width of GOME (960 km) and cloud contamination, AOD values are only available for a small part of Europe. In Figure 7.9 the model and GOME AOD are plotted as a function of latitude, for the GOME overpass on 11 August. The GOME tracks for the east, nadir and west pixels are presented separately in Figures 7.9a, 7.9b and 7.9c. The model AOD shows peaks around 45° N and around 56° N , for all three tracks. The few GOME data do not allow for a direct comparison with the model spatial variation. Nevertheless, the data available are useful for a first evaluation of the model AOD prediction. For example, the nadir and west pixel show variations between 45° N and 57° N that are similar to those in the model results, although the location of the peaks do not exactly match. This may be due to the difference in spatial res-

Date	Orbit	Cloud-free	Total
10 Aug 1997	12058	25	207
11 Aug 1997	12072	96	300
12 Aug 1997	12086	52	267
20 Aug 1997	12200	33	210
20 Aug 1997	12201	58	237
21 Aug 1997	12215	77	267
22 Aug 1997	12229	96	240

Table 7.2: Date, orbit number, number of cloud-free pixels and total number of pixels for GOME overpasses over Europe for 10 to 12 August, and for 20 to 22 August, 1997.

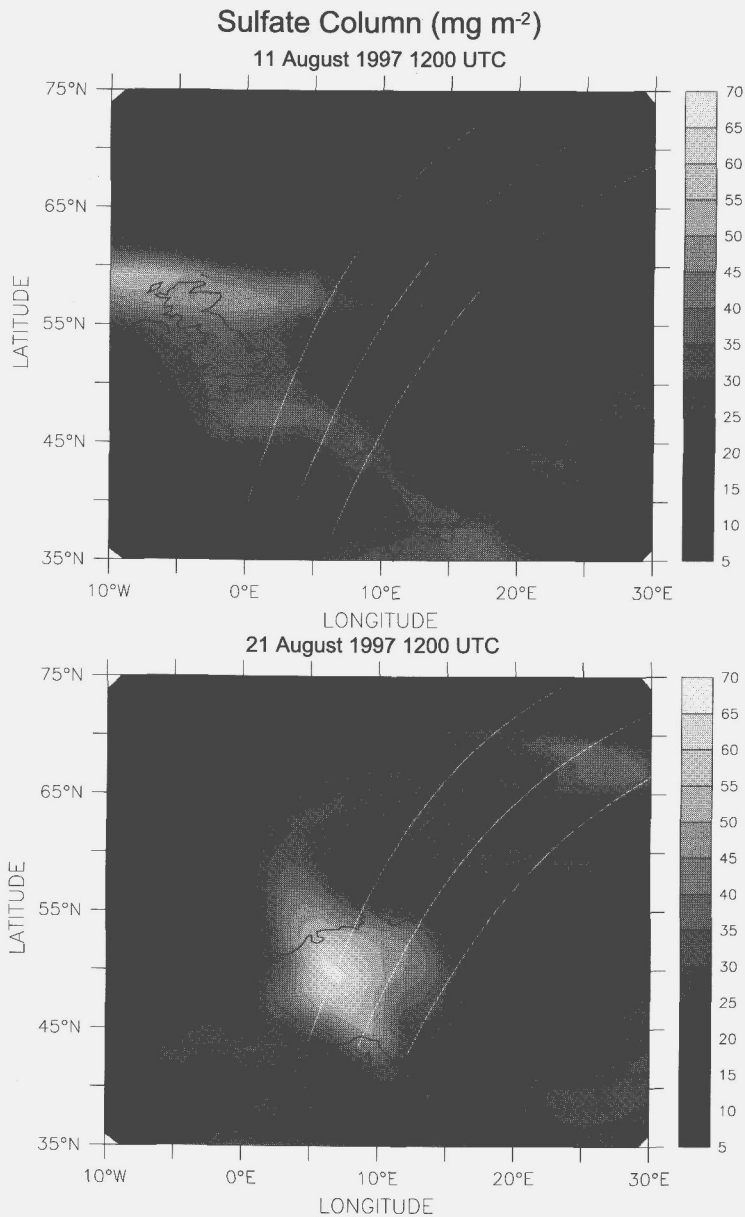


Figure 7.6: Calculated sulfate column burden (in $\text{mg m}^{-2} \text{SO}_4^-$) for 11 August 1997 (upper panel) and 21 August 1997 (lower panel). Lines show the tracks of the centers of the GOME east, nadir and west pixel tracks, for the overpasses on these days.

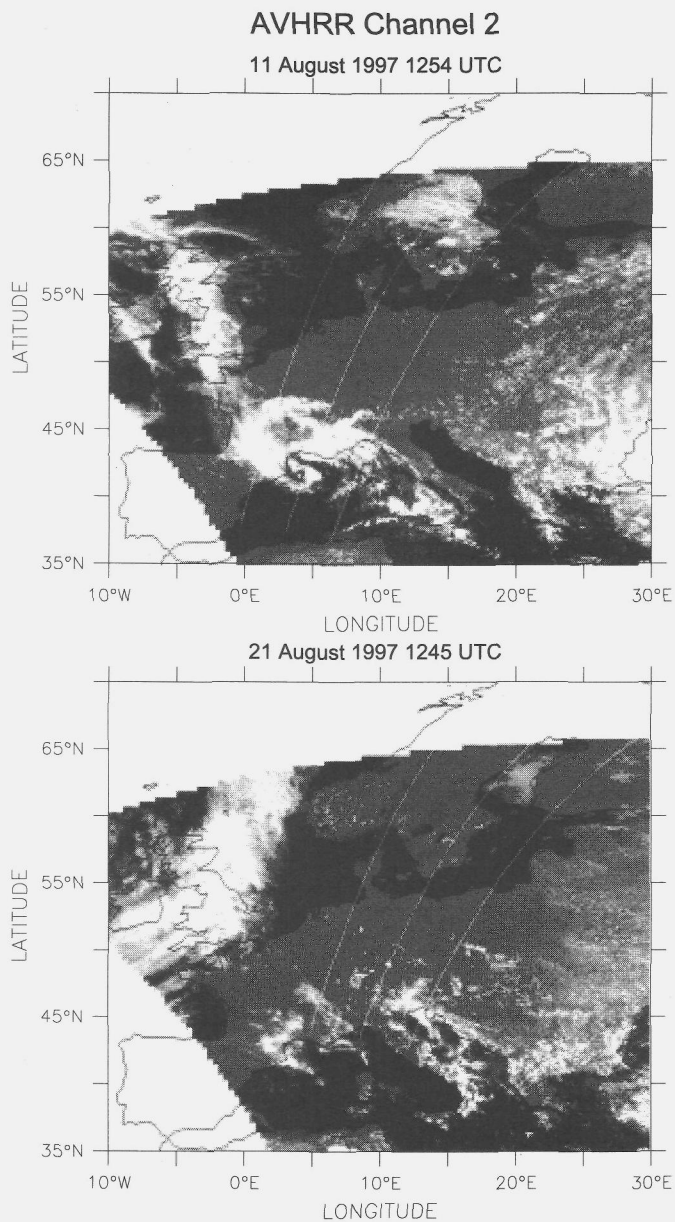


Figure 7.7: AVHRR channel 2 ($0.86 \mu\text{m}$) image for afternoon overpass on 11 August 1997 (upper panel) and 21 August 1997 (lower panel). Lines show the tracks of the centers of the GOME east, nadir and west pixel tracks, for the overpasses on these days.

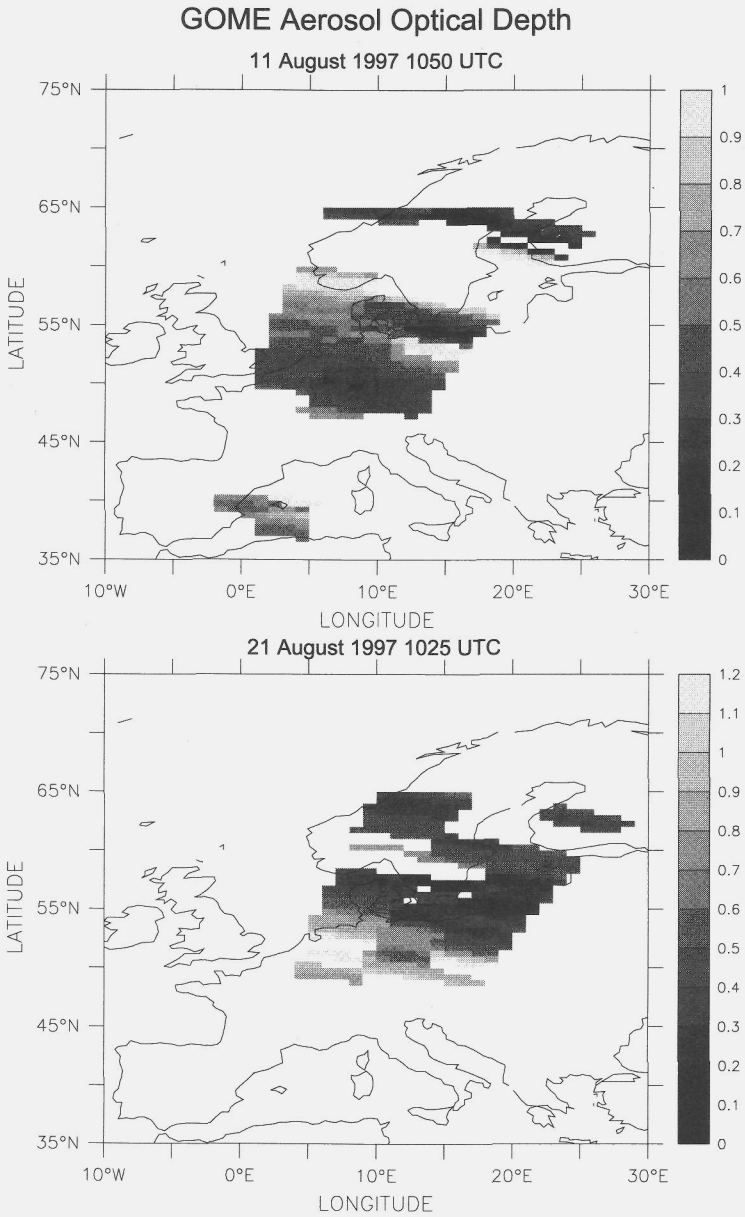


Figure 7.8: Aerosol optical depth at 0.400 μm from GOME overpass on 11 August 1997 (upper panel) and 21 August 1997 (lower panel). Note the different scales.

olution, temporal variations, inexact matching of locations, model assumptions and sub-pixel cloud contamination. The GOME data for the east pixel (Figure 7.9a) is hard to interpret. From the AVHRR image, it is unclear whether the increases in AOD around 51° N and 55° N can be trusted or are artifacts caused by sub-pixel cloud contamination.

The GOME and model AOD for 21 August 1997 are shown in Figure 7.10. The model AOD shows a maximum over the European mainland around 50° N, which is most pronounced for the west track (Figure 7.10c), which passes exactly over the area with the highest sulfate load. In Figures 7.10a en 7.10b a second maximum is found around 60° N. In all tracks a strong peak in AOD is present between 66° en 68° N. This maximum is caused by a combination of increased sulfate load and a high RH ($>90\%$). For all three pixel tracks the GOME data trace the model results reasonably well. The west pixel track shows the largest AOD gradient, in good agreement with the spatial distribution of the sulfate aerosol in Figure 7.6.

In addition to the comparison of the spatial variation of the AODs derived from the TM3 model and from the GOME data, a comparison of all results for the two periods (Table 7.2) is presented in Figure 7.11. This Figure shows that for most pixels the model AOD is higher than the GOME values. The difference between the model and GOME AODs is on average 0.14 with a standard deviation of 0.23. In 75% of the cases the model AODs are within a factor of two of the GOME data. As mentioned above, the data in Figure 7.11 is for two periods: 10-12 August, and 20-22 August. For the first period, the difference between the model and GOME AODs is on average 0.06 with a standard deviation of 0.20. For the second period, the difference was on average 0.20 with a standard deviation of 0.24. For the first period 87% of the model AODs are within a factor of two of the GOME values, for the second period 68%.

Figure 7.11 suggests that the model AODs are positively offset compared to the GOME values. This is more evident from the data in Figure 7.12, where the model AOD is plotted versus the GOME values for the overpass for only 21 August. The offset of approximately 0.2 can easily be seen in this figure. Since no negative offset was found in the comparison between the GOME and AERONET data (Figure 7.4) most probably the model values are biased. The positive offset in the model AOD can be caused by an overestimate of free tropospheric sulfate. Because the residence time is much longer, the sulfate is well distributed in the free troposphere. As a result, the free tropospheric contribution to the AOD will be relatively constant in space and time. An excess of sulfate in the free-troposphere thus shows up as a constant offset in the AOD. In model intercomparison studies, the current version of the TM3 model shows relatively high sulfate concentrations in the free troposphere [Jeuken, personal communication]. This is probably caused by a too simple wet removal scheme. A new version of the model is under development.

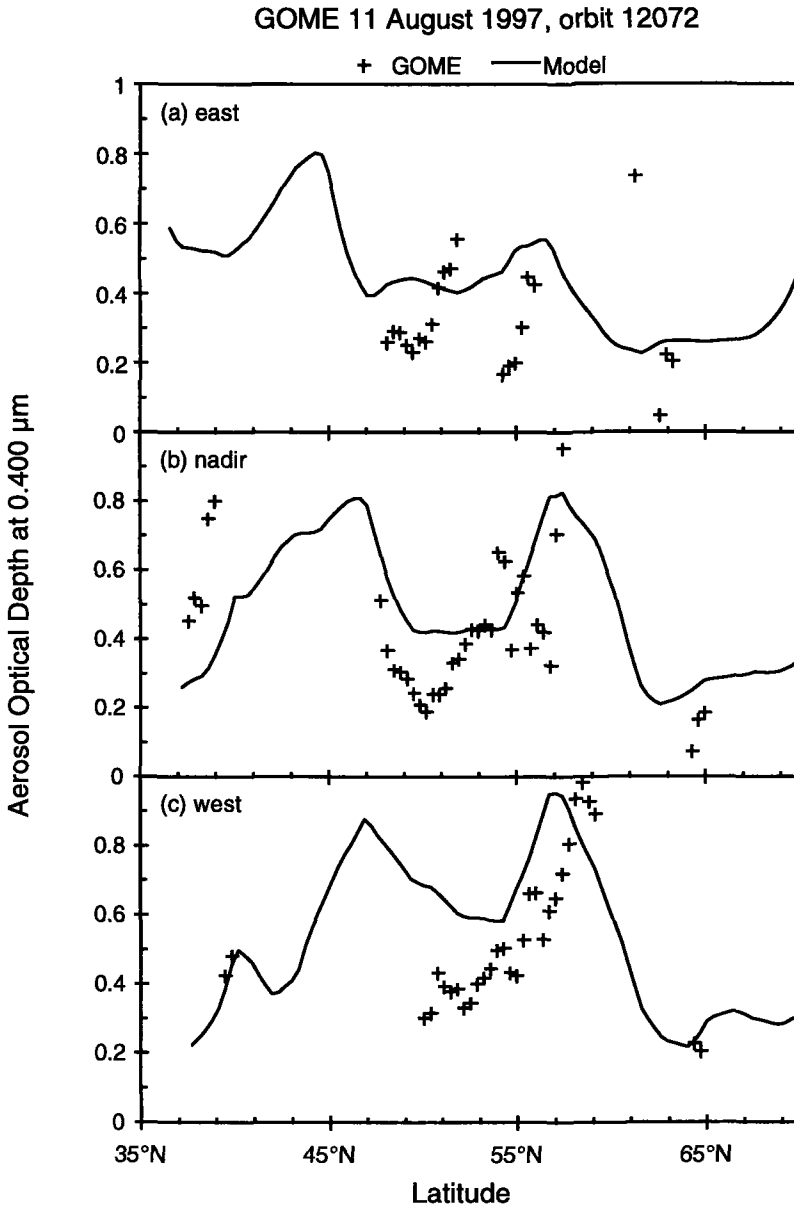


Figure 7.9: Aerosol optical depth at 0.400 μm from GOME aerosol retrieval algorithm and from the TM3 model for 11 August 1997, plotted as a function of the latitude. (a) GOME east pixel track; (b) GOME nadir pixel track; and (c) GOME west pixel track.

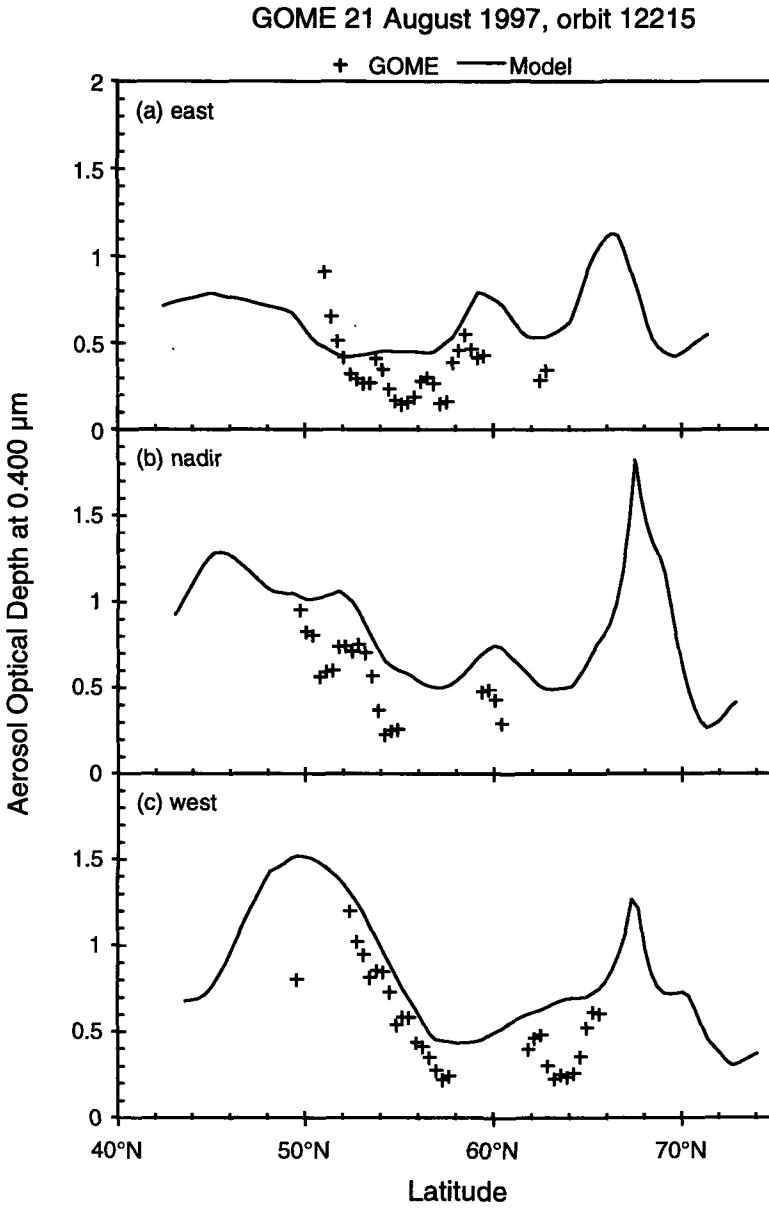


Figure 7.10: As Figure 7.9, but for 21 August 1997. Note that the vertical scales differ from those in Figure 7.9.

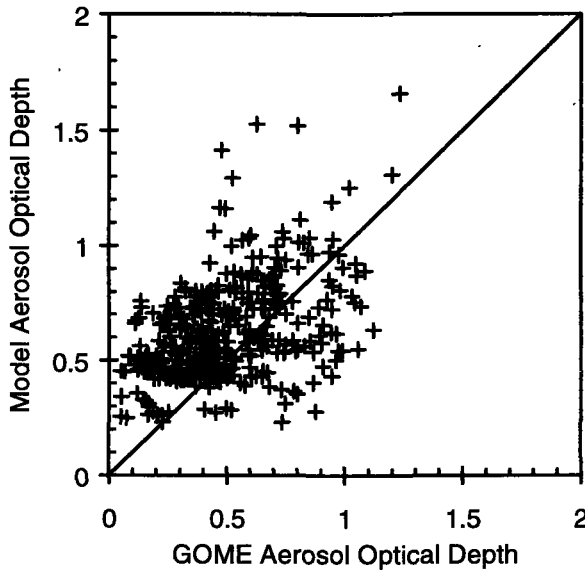


Figure 7.11: Aerosol optical depth at $0.400 \mu\text{m}$ derived from the TM3 model plotted versus the values from the GOME satellite retrieval for the orbits listed in Table 7.2. The line shows the identity line for the two data sets.

7.7 Conclusions

AOD derived from the TM3 sulfate concentration is compared to satellite retrievals from GOME data. Comparisons with ground based sunphotometer data show good correlation (correlation coefficient 0.80) for the GOME retrieval. For the model derived AOD the correlation with the sunphotometer data is much less. The model AOD is typically within a factor of two of the sunphotometer data. This is a reasonable result, given the many assumptions used in calculating the sulfate concentration by the TM3 model, and in estimating the AOD from the sulfate concentration. To derive the AOD from the sulfate concentration the aerosol size distribution is assumed constant, the contribution of non-sulfate aerosol is taken proportional to the sulfate AOD, and boundary layer RH is used to assess the hygroscopic growth of the aerosol particles. These assumptions alone can cause differences of the order of a factor of two or more. Furthermore, the comparison between the sunphotometer data and the TM3 model is difficult due to the difference in spatial and temporal resolution. However, this also holds for the GOME retrievals.

For two periods of three days each, GOME retrievals were compared to TM3 model derived AODs over Europe. Cloud contamination, and the limited swath width of GOME cause that retrieval data are only available over a small part

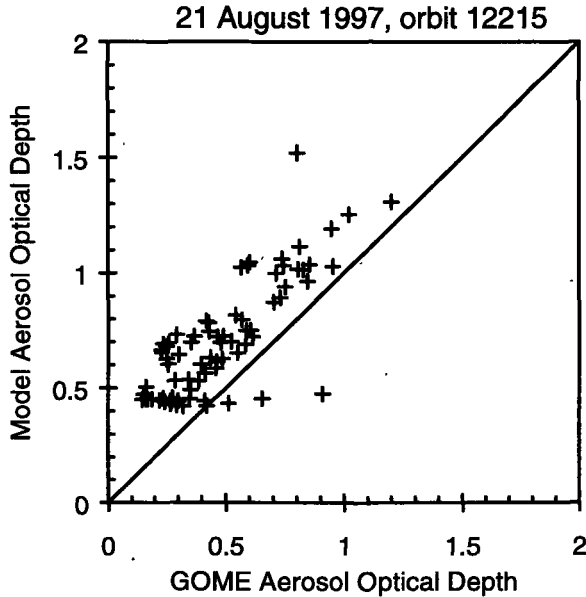


Figure 7.12: As Figure 7.11, but for GOME overpass on 21 August 1997.

of Europe. In spite of the limited amount of GOME data, certain features in the spatial aerosol distribution were observed in both the GOME and the model data. The difference between the model and GOME AOD was 0.14 with a standard deviation of 0.23 for all data for the two periods. Most of the model values (75%) were within a factor of two of the GOME values. This factor of two was also observed between the model results and the sunphotometer data.

The model AOD were positively offset compared to the GOME data. This offset can be explained by an excess of sulfate predicted by the TM3 model in the free troposphere. This was supported by model intercomparisons, and is probably caused by a too simple wet removal scheme. A new version of the model is currently under development.

Overall the GOME and the model results are in reasonable agreement, considering the large assumptions in modeling the AOD. Since only the sulfur cycle was accounted for in the TM3 model, it is anticipated that better agreement will be obtained when other important aerosol species, such as nitrate and carbonaceous material, are modeled as well. The satellite retrieval is limited by swath width and the large pixel size of GOME. This causes a large number of cloud contaminated pixels and limited spatial coverage. In the coming years, new spaceborne spectrometers with a larger swath and a smaller footprint will be launched. Combination of 3D chemical transport models and satellite remote sensing has great potential, both for validation of the models, for interpretation of satellite data, and in assimilation of satellite data.

7.8 Acknowledgments

This work is supported by the Netherlands Space Research Organization (SRON), under contract EO-008. The GOME data were kindly provided by the European Space Agency (ESA) through DLR. The authors would like to thank Dr. D. Tanré from the Laboratoire d'Optique Atmosphérique (LOA), Université de Lille, and Dr. G. Zibordi from the European Commission Joint Research Centre, for the AERONET data. The Ferret analysis package, developed by NOAA PMEL, was used in the preparation of this work (available at <http://ferret.wrc.noaa.gov/>).

Bibliography

- Andres, R. J. and Kasgnoc, A. D. (1998). A time-averaged inventory of aerial volcanic sulfur emissions. *J. Geophys. Res.*, 103:25,251–25,261.
- Dentener, F., Feichter, J., and Jeuken, A. (1998). Simulations of ²²²radon using off- and online models. *Tellus*, page in press.
- Diederer, H., Guicherit, R., and Hollander, J. (1985). Visibility reduction by air pollution in the netherlands. *Atmos Environ.*, 19:377–383.
- Ganzeveld, L., Lelieveld, J., and Roelofs, G.-J. (1998). Dry deposition parametrization of sulfur oxides in a chemistry and general circulation model. *J. Geophys. Res.*, 103:5679–5694.
- Holben, B., Eck, T., Slutsker, I., Tanré, D., Buis, J., Setzer, A., Vermote, E., Reagan, J., Kaufman, Y., Nakajima, T., Lavenu, F., Jankowiak, I., and Smirnov, A. (1998). Aeronet- a federated instrument network and data archive for aerosol characterization. *Remote Sens. Environ.*, 66:1–16.
- Jeuken, A. (1999). KNMI, p0-box 201, 3730 AE de bilt, the netherlands. e-mail: jeuken@knmi.nl.
- Jeuken, A., Eskes, H., Holm, E., Velthoven, P. V., and Kelder, H. (1999). Assimilation of TOVS total ozone columns in a three-dimensional tracer transport model. *J. Geophys. Res.*, page in press.
- Kalnay, E. and Co-authors (1996). The ncep/ncar 40-year reanalysis project. *Bull. Amer. Meteor. Soc.*, 77:437–471.
- Kiehl, J. T. and Briegleb, B. P. (1993). The relative roles of sulfate aerosols and greenhouse gases in climate forcing. *Science*, 260:311–314.
- Koppers, G. (1997). *Radiative Transfer in the Absorption Bands of Oxygen: Studies of their Significance in Ozone Chemistry and Potential for Aerosol Remote Sensing*. PhD thesis, Stockholm University.
- Langner, J. and Rodhe, H. (1991). A global three-dimensional model of the tropospheric sulfur cycle. *J. Atm. Chem.*, 13:225–263.

- Liss, P. and Merlivat, L. (1986). Air-sea gas exchange rates: Introduction and synthesis. In Menard, P., editor, *The Role of Sea-Air Exchange in Geochemical Cycling*, pages 113–127. Reidel, Dordrecht.
- Roelofs, G.-J. and Lelieveld, J. (1995). Distribution and budget of O_3 in the troposphere calculated with a chemistry general circulation model. *J. Geophys. Res.*, 100:20,983–20,998.
- Smirnov, A., Holben, B., Eck, T., Dubovik, O., and Slutsker, I. (1999). Cloud screening and quality control algorithms for the AERONET data base. *Rem. Sens Environ.*, page submitted.
- Tanré, D., Herman, M., and Kaufman, Y. J. (1996). Information on aerosol size distribution contained in solar reflected radiances. *J. Geophys. Res.*, 101:19,043–19,060.
- Tanzi, P., Hegels, E., Aben, I., Bramstedt, K., and Goede, A. (1998). Preliminary results on the performance degradation of earth radiation spectra measured by GOME. In *Optical Remote Sensing of the Atmosphere and Clouds*, page 3501. SPIE.
- Tegen, I., Hollrig, P., Chin, M., Fung, I., Jacob, D., and Penner, J. (1997). Contribution of different aerosol species to the global aerosol extinction optical thickness: Estimations from model results. *J. Geophys. Res.*, 102(D20):23,895–23,915.
- ten Brink, H. M., Veefkind, J. P., Waaijers-IJpelaan, A., and van der Hage, J. C. H. (1996). Aerosol light-scattering in the netherlands. *Atmos. Environ.*, 30:4251–4261.
- Veefkind, J. P., van der Hage, J. C. H., and ten Brink, H. M. (1996). Nephelometer derived and directly measured aerosol optical depth of the atmospheric boundary layer. *Atmos. Res.*, 41:217–228.

Chapter 8

Concluding Remarks

Aerosols are important for many processes in the atmosphere. They are the largest uncertainty in global climate models. To a large extent this uncertainty is caused by a lack of aerosol data on a global scale, both as regards their occurrence, their physical and chemical properties, and/or their effects on e.g. climate, through their optical properties, and their influence on clouds. Due to the limited lifetimes of aerosols in the lower troposphere the aerosol field is highly variable in space and time. Several examples of this variability are presented in Chapter 4,5 and 7. Frequent measurement of the global aerosol field is only achievable by satellite remote sensing. However, aerosol satellite remote sensing is far from straightforward. It is a notoriously underdetermined problem, for which many assumptions have to be made in the retrieval algorithms. These assumptions regard not only the surface reflectivity, but also the aerosol properties itself. Validation of aerosol algorithms in so-called closure experiments is therefore of crucial importance.

Aerosol satellite remote sensing puts high demands on the satellite sensors. The sensors should have narrow spectral bands outside gaseous absorption regions, and the data should be well-calibrated. Data from sensors that meet these requirements are available only for the last few years. Earlier, data came from sensors that were not designed for aerosol satellite remote sensing. Their application is therefore limited.

In this thesis different aerosol retrieval techniques were presented. Until recently it was thought that aerosol retrieval was only possible over surface areas with a low and preferably constant albedo, such as oceans. Due to the difference in surface reflectivity properties, aerosol retrieval over the ocean differs strongly from aerosol retrieval over land. The differences are not only in the treatment of the surface reflectivity, but also on the choice of the wavelength range that is best suitable for aerosol satellite remote sensing. In addition, aerosol sources over the continents differ from those over the ocean. The capabilities of new sensors make it possible to retrieve aerosol over land as well. In fact, most of this thesis is on aerosol retrieval over land. However, aerosol retrieval over land is still less advanced and less accurate than aerosol retrieval over the ocean.

All the retrieval algorithms presented in this thesis apply to cloud-free scenes. Especially for sensors with a poor spatial resolution like GOME, this is a serious limitation for the application of aerosol satellite remote sensing.

8.1 Aerosol retrieval over the ocean

Chapters 3 and 4 are dedicated to aerosol retrieval over the ocean. In chapter 3 the aerosol retrieval algorithm for this application was described. For accurate aerosol retrieval it is important to include multiple scattering as well as the bi-directional surface reflection. The bi-directional surface reflection is especially important over the ocean since Fresnel reflection by the sea surface causes both sunglint and skyglint. Serious errors in the retrieved AOD occur when this effect is not accounted for. A sensitivity study showed that the largest uncertainties in the retrieval method can be expected due to the assumptions as regards the oceanic whitecaps and the assumed aerosol size distributions.

In chapter 4 the ocean aerosol retrieval algorithm is tested in a so-called closure experiment. The retrieval algorithm was applied to ATSR-2 and AVHRR data and the results were compared to sunphotometer measurements. The ATSR-2 has more and smaller spectral bands, and is better calibrated than the AVHRR. Comparison with airborne sunphotometer data showed that the AOD from the ATSR-2 retrieval is more accurate than the AVHRR retrieved values, demonstrating that the retrieval significantly improves when data are used from a sensor that is more suitable for aerosol retrieval. Another key result is that both the AOD and its spectral behavior, which can be used to assess the aerosol size distribution, can be retrieved accurately. Within a few years a number of satellite sensors will be available that meet the requirements for aerosol retrieval over the ocean. It is therefore anticipated that an accurate global data set of AOD and Ångström parameters over the ocean can be constructed within a couple of years.

8.2 Aerosol retrieval over land

Aerosol retrieval over land surfaces is much more difficult than over the ocean. The key problem in aerosol retrieval over land is to distinguish between surface and atmospheric contribution to the satellite measured reflectance. In this thesis two methods are presented for aerosol retrieval over land: the ATSR-2 dual view algorithm and the GOME UV method. The ATSR-2 dual view algorithm, which was presented in chapter 5, uses both the spectral and the directional information in the ATSR-2 data. In the dual view algorithm, the shape of the bi-directional surface reflectance is assumed independent of the wavelength, which is a much weaker assumption than prescribing the surface albedo. In chapters 5 and 6 the dual view algorithm was validated using ground based sunphotometer results for the US east coast and Europe. These comparisons show that the dual view algorithm can retrieve the AOD as well as its spectral behavior. The dual view

algorithm clearly demonstrates the added value of a sensor concept with a two or multi-angle view. Using a relatively simple method, aerosol retrieval of the AOD and Ångström parameter is possible over different type of land surface. As the ATSR-2 was launched in 1995, it should be possible to construct a global aerosol database over land starting in 1995. It is expected that the dual-view algorithm will fail over areas with high surface albedo, such as deserts or snow cover.

The GOME UV aerosol retrieval algorithm uses data in the wavelength range between 0.340 to 0.400 μm . In this wavelength range the albedo of most land surfaces is low. The satellite measured reflectance is therefore dominated by scattering in the atmosphere. The GOME UV algorithm uses prescribed surface albedo values. In chapter 6 and 7 the GOME UV algorithm was validated using ground based sunphotometer data and ATSR-2 dual view results. These results are encouraging, given the simple treatment of the surface albedo. However, due to the large pixels size of $320 \times 40 \text{ km}^2$ GOME has limited application. Most of the GOME pixels are cloud contaminated, and a global database of aerosol retrievals for cloud free GOME pixels will be strongly biased to certain meteorological conditions. Future sensors measuring in this wavelength range will have a much smaller footprint. Therefore aerosol retrieval in the UV, over both land and sea, has strong potentials.

8.3 Application of aerosol retrieval

Satellite remote sensing can provide the spatial aerosol distribution. In detailed field experiments data is usually obtained at single locations, or for a limited area. Satellite remote sensing can be used as additional tool, providing the spatial aerosol distribution over a much larger area. A disadvantage of aerosol satellite remote sensing is that no information is provided on the vertical distribution. In chapter 4 aerosol retrieval over the ocean was combined with *in situ* aircraft observations, providing information on the three dimensional aerosol distribution.

Analysis of aerosol fields produced by aerosol satellite remote sensing contributes to development and validation of models that describe the global aerosol field and effects of changing emissions. On the other hand the models can help to understand the observed aerosol field, and fill the gaps both in space and time between the satellite data. In chapter 7 satellite remote sensing is compared to results from a three dimensional chemical transport model. Although the model can be strongly improved, in particular by adding nitrate and organic aerosol species, this first comparison of actual model data with satellite retrieval results is encouraging.

8.4 Future Outlook

The ideal satellite sensor for aerosol retrieval should have a spectral range from the UV to the mid infrared, a moderate spectral resolution (~ 1 nm), a spatial resolution of a few kilometers, a wide swath width providing daily global coverage, a multi-angle view, and the possibility to measure the polarization. Also, the use of geostationary satellites should be considered, as they can observe changes in the aerosol field over the day. Clearly such an ideal sensor is not available in the near future. This work describes algorithms with sensors that partly cover the features of the ideal aerosol retrieval sensor. The ATSR-2 is a radiometer with a few narrow spectral bands, good spatial resolution and a two-view capability. GOME is a spectrometer with a wide spectral range and high spectral resolution. Based on these sensors, new retrieval algorithms have been developed that show good results both over the ocean and over land. In the coming years the satellite instruments will be further improved, and it is anticipated that aerosol retrieval will improve considerably as well. As the ideal sensors will not be available, the synergy of different sensors will become important. Combination of data from different sensors at different stages during the retrieval process will improve the overall aerosol retrieval. For sensors with a very wide spectral range, different algorithms may apply that can be combined in the retrieval process.

Satellite remote sensing provides column integrated aerosol optical properties. Interpretation of this data will give some information on the sources of the aerosol particles. Combination of satellite remote sensing with three-dimensional chemical transport models will give insight in the processes governing the aerosol spatial and temporal aerosol distribution. In data assimilation studies, remote sensing data of aerosol properties and their precursor gases such as SO_2 and NO_2 should be combined with the models. Ultimately, these studies should lead to models that can predict the effects of the changing aerosol emissions on the human environment.

Appendix A

List of Acronyms

AERONET	Aerosol Robotic Network, Network of Sun/sky radiometers.
AOD	Aerosol Optical Depth.
ECN	Netherlands Energy Research Foundation.
ATSR-2	Along Track Scanning Radiometer 2; Two-view radiometer on ERS-2.
AVHRR	Advance Very High Resolution Radiometer; Radiometer on NOAA satellites.
ENVISAT	ESA Environmental Satellite to be launched in 2000.
ERS-2	ESA Remote Sensing Satellite launched in 1995.
ESA	European Space Agency.
GOME	Global Ozone Monitoring Experiment; Spectrometer on ERS-2.
KNMI	Royal Netherlands Meteorological Institute.
NASA	USA National Aeronautics and Space Administration.
NOAA	USA National Oceanic and Atmospheric Administration.
PMD	Polarization Measuring Device of GOME.
SRON	Netherlands Space Research Organization.
SCIAMACHY	Scanning Imaging Absorption Spectrometer for Atmospheric Cartography; spectrometer on ENVISAT.
TNO-FEL	Netherlands Organization for Applied Scientific Reserach, Physics and Electronics Laboratory.
TOMS	Total Ozone Mapping Spectrometer; Ozone monitoring instrument.

Summary

Aerosol particles are important for many processes in the atmosphere. They affect global climate by scattering and absorbing the incoming solar radiation and by modifying the albedo and lifetimes of clouds. Aerosol effects are a leading uncertainty in predicting global climate change. To a large extent this uncertainty is caused by the lack of knowledge on the occurrence and concentration of aerosols, which are highly variable. On a global scale, this information can only be obtained by satellite remote sensing.

Most aerosol retrieval techniques apply only to cloud-free conditions. Aerosol particles modify the top-of-the-atmosphere radiance. In the absence of clouds, the radiance measured by a satellite sensor is caused by scattering in the atmosphere by aerosols and molecules, and by reflection by the Earth's surface. A key problem in aerosol retrieval is to distinguish between the atmospheric and surface contributions. These can best be separated when the reflectivity of the surface is low and constant, as for example over the ocean. Over land the reflectivity is much higher and usually not known with enough accuracy, which greatly complicates aerosol satellite retrieval. In addition to assumptions on the surface reflectivity, also assumptions on the aerosol properties have to be made in the retrieval algorithms.

In this thesis three aerosol retrieval algorithms are described. One of these applies to retrieval over the ocean, the other two were primarily designed for use over land. These algorithms compute the aerosol optical depth, which is the column integrated aerosol extinction coefficient along a vertical path through the atmosphere.

The retrieval algorithm for use over the ocean was designed to be applicable to different satellite sensors. Both multiple scattering and the bi-directional ocean reflectance is accounted for. The aerosol is assumed to be a mixture of a sea salt type and an anthropogenic type. The spectral information in the measured radiance is used to determine the best fit mixture of these two types. The total size distribution is then used to compute the aerosol optical depth. Sensitivity analysis shows that the largest uncertainties in the retrieved aerosol optical depth are caused by the aerosol models and by reflection by oceanic whitecaps. The ocean retrieval algorithm was tested in a field experiment conducted at the east coast of the USA in July 1996. The algorithm was applied to data from the Along Track Scanning Radiometer 2 (ATSR-2) and the Advanced Very High Resolution Radiometer (AVHRR). Comparisons between aerosol op-

tical depth derived from ATSR-2 data and aerosol optical depth measured with a sunphotometer, showed that the aerosol optical depth and its spectral behavior are retrieved accurately. The spectral behavior is important since it can be used to assess the aerosol size distribution. The retrieval from ATSR-2 data was significantly better than from AVHRR data, which indicates that the retrieval significantly improves for sensors with more spectral information and a better calibration. The combined satellite and airborne data provided information on the three-dimensional aerosol distribution, demonstrating the use of satellite data in intensive field experiments.

The dual view algorithm was designed for aerosol retrieval over land from ATSR-2 data. It uses the dual view capability of the ATSR-2, which provides two views for each region. The information from the two viewing directions and the spectral information is used to separate the surface and atmospheric contributions to the top-of-the-atmosphere radiance. The dual view algorithm assumes that the shape of the bi-directional surface reflectance is independent of the wavelength, and that the effect of aerosols is small at $1.6 \mu\text{m}$. Validation experiments at the US east coast and for northwestern Europe show good agreement between the satellite retrieved spectral aerosol optical depth and sunphotometer derived values. The dual view algorithm can thus be applied for assessing the aerosol load and the aerosol size distribution over land.

A second algorithm that was designed for aerosol retrieval over land uses data from the Global Ozone Monitoring Experiment (GOME) in the wavelength range between 0.340 and $0.400 \mu\text{m}$. In this wavelength range the albedo of most land surfaces is low. The aerosol optical depths retrieved using the GOME UV method show good agreement with ground-based sunphotometer data and with ATSR-2 dual view results. The major difficulty with GOME data is the poor spatial resolution of $320 \times 40 \text{ km}^2$ or $80 \times 40 \text{ km}^2$, which leaves few cloud-free pixels. However, the validation experiments clearly show the potential of aerosol retrieval over land in the UV.

Aerosol satellite remote sensing can contribute to the development and validation of chemical transport models. These models have the ability to predict the effects of changing emissions on the global aerosol field. Vice versa, model results can also be used as a source of information that can help understanding the satellite observed aerosol field. Results from the TM3 chemical transport model are compared to GOME UV retrievals for a scenario over Europe for August 1997. The TM3 model computes the sulfate aerosol mass from which the total aerosol optical depth is computed using assumptions on the aerosol size distributions and on the contribution of non-sulfate aerosol species. The model results are in reasonable agreement with the satellite retrieval results, particularly in regard of the large assumptions in the method to derive the model result.

Results in this thesis show successful retrieval of information on the concentration and size of aerosol particles from satellite measurements. From the short lifetimes of aerosols in the lower troposphere, it is expected that the spatial and temporal variations of the aerosol field are large. This is confirmed by the case studies presented in this thesis. Especially in the heavily industrialized regions,

such as western Europe and the US east coast, variations in the aerosol optical depth of more than a factor of three are observed over a few hundred kilometers. In the remote marine environment the variations are much smaller.

Samenvatting

Aërosolen zijn kleine deeltjes, zoals stof, roet en zeezout deeltjes, die in de atmosfeer zweven. Deze deeltjes spelen een belangrijke rol bij veel processen in de atmosfeer. Ze beïnvloeden het mondiale klimaat op twee manieren: door verstrooien en absorberen van zonnestraling, en door hun effect op de reflectiviteit en levensduur van wolken. Aërosol effecten vormen één van de grootste onzekerheden in voorspellingen van mondiale klimaatveranderingen. Voor een belangrijk deel worden deze onzekerheden veroorzaakt door het gebrek aan kennis over de concentratie en eigenschappen van het aërosol, welke sterk variëren in zowel plaats als tijd. Op mondiale schaal kan informatie hierover alleen worden verkregen door gebruik te maken van satelliet metingen.

Doordat aërosol deeltjes kortgolvlige straling verstrooien en absorberen hebben ze effect op de hoeveelheid straling, zoals die gemeten wordt aan de top van de atmosfeer met satelliet sensoren. Het proces om deze uit ruwe stralingsmetingen aërosol eigenschappen te bepalen wordt aërosol retrieval genoemd. Vrijwel alle aërosol satelliet retrieval methoden zijn alleen toepasbaar in onbewolkte condities. In het onbewolkte geval wordt de straling die gemeten wordt door een satelliet sensor veroorzaakt door verstrooiing in de atmosfeer en reflectie door het aardoppervlak. Één van de belangrijkste problemen in aërosol satelliet remote sensing is onderscheid te maken tussen de bijdragen van de atmosfeer en die van het oppervlak. Dit is relatief eenvoudig als de reflectiviteit van het oppervlak klein en constant is, zoals bijvoorbeeld het geval is voor oceanen. De reflectiviteit van landoppervlakken daarentegen is in het algemeen veel groter en meestal slecht bekend. Dit compliceert de aërosol retrieval in hoge mate, omdat er aannamen moeten worden gedaan over oppervlakte reflectiviteit. Daarnaast dienen er in de retrieval algoritmes ook aannamen worden gemaakt over de aërosol eigenschappen.

In dit proefschrift worden drie aërosol retrieval algoritmes beschreven. Één daarvan is alleen toepasbaar boven zee, de andere twee zijn in eerste instantie ontwikkeld voor retrieval boven land (maar ook toepasbaar boven zee). Met deze algoritmes wordt de aërosol optische dikte bepaald: de extinctie geïntegreerd over een verticaal pad door de atmosfeer.

Het algoritme voor retrieval boven de oceaan is zodanig ontworpen dat het toegepast kan worden op data van verschillende satelliet instrumenten. Zowel multiple verstrooiing als de bi-directionele reflectie van het zeeoppervlak worden in beschouwing genomen. Er wordt aangenomen dat het aërosol een mengsel is

van een antropogeen en een zeezout aërosol component. De spectrale informatie in de gemeten straling wordt gebruikt om het best passende aërosol mengsel te bepalen. Hiermee wordt vervolgens de aërosol optische dikte berekend. Een gevoeligheidsstudie heeft aangetoond dat de grootste onzekerheden in de berekende aërosol optische dikte worden veroorzaakt door de gebruikte aërosolmodellen en door de reflectie van schuimkoppen op de oceaan. Het algoritme voor retrieval boven de oceaan kon worden getest tijdens een veldexperiment dat in juli 1996 plaatsvond aan de oostkust van de Verenigde Staten. Het algoritme werd toegepast op data van twee satelliet sensoren: de ATSR-2 (Along Track Scanning Radiometer 2) en de AVHRR (Advanced Very High Resolution Radiometer). Vergelijkingen tussen aërosol optische dikte bepaald uit de ATSR-2 data, en die gemeten met een zogenaamde zonnephotometer, toonden aan dat de aërosol optische dikte en het spectrale verloop daarvan goed kon worden bepaald uit de satelliet metingen. De ATSR-2 retrieval was significant beter dan die van de AVHRR, hetgeen laat zien dat de retrieval sterk verbetert wanneer data worden gebruikt met meer spectrale informatie en een betere calibratie. Door satellieten vliegtuiggegevens te combineren kon een beeld worden gevormd over de driedimensionale aërosol verdeling in de troposfeer. Hiermee werd de meerwaarde van satelliet gegevens in een veldexperiment aangetoond.

Het zogenaamde dual view algoritme werd ontwikkeld voor aërosol retrieval boven land uit ATSR-2 metingen. Het ATSR-2 instrument meet ieder gebied onder twee verschillende kijkrichtingen. Door de directionele informatie uit de twee kijkrichtingen te combineren met de spectrale informatie, kan er onderscheid gemaakt worden tussen de respectievelijke bijdrage van de atmosfeer en van het oppervlak aan de gemeten straling. Het dual view algoritme neemt aan dat de vorm van de bi-directionele oppervlaktereflectiviteit niet afhangt van de golflengte, en dat de aërosol bijdrage bij een golflengte van $1.6 \mu\text{m}$ klein is. Validatie-experimenten aan de oostkust van de Verenigde Staten en in West Europa laten zien dat de spectrale aërosol optische diktes uit het dual view algoritme goed overeenkomen met resultaten van zonnephotometer metingen. Met het dual view algoritme is het dus mogelijk uit satelliet metingen schattingen te maken van de aërosol concentratie en de aërosol grootteverdeling boven land.

Een tweede algoritme dat is ontwikkeld voor aërosol retrieval boven land, gebruikt metingen in het golflengtegebied tussen 0.340 en $0.400 \mu\text{m}$ van het GOME (Global Ozone Monitoring Experiment) instrument. In dit golflengtegebied is de reflectiviteit van de meeste grondoppervlakken laag. De aërosol optische diktes uit het GOME UV algoritme komen goed overeen met zonnephotometer waarden en met ATSR-2 dual view resultaten. Helaas is de ruimtelijke resolutie van GOME beperkt ($320 \times 40 \text{ km}^2$ of $80 \times 40 \text{ km}^2$), zodat er weinig wolkenvrije pixels zijn. Zoals al eerder opgemerkt zijn wolkenvrije pixels noodzakelijk voor aërosol retrieval. De validatie-experimenten demonstreren wel dat aërosol retrieval in het UV veel potentieel heeft.

Aërosol satelliet remote sensing kan bijdragen aan de ontwikkeling en validatie van chemische transportmodellen. Met deze modellen kunnen de effecten van veranderende emissies op het mondiale verdeling van aërosol worden voorspeld. Vice versa kunnen de model resultaten ook worden gebruikt om satellietwaar-

nemingen van het aërosol-veld te begrijpen. Resultaten van het TM3 chemische transportmodel zijn vergeleken met GOME UV retrievals voor Europa voor augustus 1997. Het TM3 model berekent de aërosol sulfaat massa, waaruit de totale aërosol optische dikte wordt berekend. Daarbij wordt gebruik gemaakt van aannamen over aërosol grootteverdelingen over de bijdrage van aërosolen waarin geen sulfaat voorkomt. De model-resultaten zijn in redelijke overeenstemming met de satelliet retrievals, met name gezien de aannamen die moeten worden gemaakt voor het berekenen van het modelresultaat.

De resultaten in dit proefschrift laten zien dat het goed mogelijk is om informatie over de concentratie en grootte van aërosol deeltjes in de atmosfeer uit satelliet waarnemingen te bepalen. Aërosol deeltjes hebben een korte verblijftijd in de atmosfeer, waardoor grote variaties in zowel ruimte als tijd kunnen worden verwacht. Resultaten in dit proefschrift bevestigen dit beeld. Met name in de sterk geïndustrialiseerde gebieden, zoals de oostkust van de Verenigde Staten en West Europa worden variaties van meer dan een factor drie over een paar honderd kilometer waargenomen. In een schone maritieme omgeving zijn de variaties veel kleiner.

Curriculum Vitae

Pepijn Veeffkind werd geboren op 1 mei 1970 in Eindhoven. Vanaf 1982 bezocht hij in Geldrop het Strabrecht College, waaraan hij in 1988 het VWO diploma behaalde. Aansluitend studeerde hij natuurkunde aan de toenmalige Rijksuniversiteit Utrecht. In 1990 behaalde hij het propedeutisch examen, hierna ging hij verder met de bovenbouwstudie meteorologie en fysische oceanografie. In 1994 behaalde hij het doctoraal examen meteorologie (met genoegen) aan de Universiteit Utrecht. Het afstudeerwerk had als onderwerp "lichtverstrooiing door atmosferisch aërosol" en werd uitgevoerd bij het Energie Onderzoekscentrum Nederland (ECN) in Petten. Na zijn afstuderen was de auteur van oktober 1994 tot januari 1995 werkzaam bij ECN. Aansluitend startte hij zijn promotieonderzoek bij TNO Fysisch en Elektronisch Laboratorium in Den Haag, onder leiding van Prof. Dr. G. de Leeuw. Gedurende dit onderzoek is hij tweemaal enkele maanden te gast geweest bij de Naval Postgraduate School in Monterey, California. Per 15 april 1999 is Pepijn Veeffkind als onderzoeker werkzaam bij het KNMI in De Bilt.